Nanostructured heterogeneous catalysts for green oxidation processes

Daniil Ovoshchnikov

A thesis presented to the University of Canterbury in partial fulfilment of the requirements for the degree of Doctor of Philosophy

University of Canterbury
Department of Chemistry
July 2014

Abstract

The development of sustainable, environmentally benign oxidation processes of organic compounds is an important task for chemical industry. This challenge can be addressed by designing catalysts that enable the utilisation of molecular oxygen as an oxidant. The work in this thesis is focused on the development of heterogeneous catalysts for the selective aerobic oxidation of various organic compounds.

The first part of the thesis (Chapters 3 and 4) covers the study of bifunctional gold catalysts for the solvent-free aerobic oxidation of cyclohexene, with a particular focus on tuning the selectivity of the catalyst. Various characterisation techniques (such as TEM, diffuse-reflectance UV-Vis spectroscopy, XPS), catalytic experiments and kinetic studies were used to investigate the nature of catalyst functionality and establish the optimal structure of a gold catalyst.

The second part of the thesis (Chapter 5) covers the study of the photocatalytic activity of hydrous ruthenium oxide deposited on TiO_2 in the aerobic oxidation of amines to nitriles under irradiation with visible light. The effect of the wavelength of the utilised light, applicability of the Sun as light source and water as a solvent were investigated. High catalytic activity of ruthenium-based catalyst was demonstrated for various benzylic and aliphatic amines. Various mechanistic studies were performed, based on which the mechanism of photocatalysis was suggested.

Table of Contents

Table of Figures

Acknowledgements

I would like to thank my supervisors, Dr Vladimir Golovko and Prof Bryce Williamson, for their guidance during my studies, as well as the University of Canterbury and the MacDiarmid Institute for generous funding.

I would like to thank Dr Matthew Polson, Dr Marie Squire, Dr Meike Holzenkämpfer and Alistair Duff for instrument training and other help during my studies; Campbell McNicoll and Tim Kemmitt from Callaghan Innovation NZ for their help with PXRD and surface area measurements; Danny Leonard, Nick Oliver Wayne Mackay and Robert McGregor for manufacturing of various equipment; Steven Graham for help with the LED assembly, Sebastian Horvath for help with measuring the characteristics of LEDs; Dr Colin Doyle from RCSMS, University of Auckland for XPS analysis; Dr Sally Gaw and Robert Stainthorpe for ICP-MS analysis; Dr Bruce Cowie and Dr Lars Thomsen from the Australian Synchrotron and Prof Gunther Andersson from Flinders University for help with Synchrotron-based XPS; Dr Takanori Sato and Mike Flaws from Department of Mechanical Engineering for TEM and SEM training and Prof Milo Kral for access to the TEM/SEM facilities.

Additional funding by Australian Synchrotron and New Zealand Synchrotron Group is very much appreciated.

I thank my colleague students from the Golovko lab who helped make my PhD experience more enjoyable.

Finally, I thank my wife and family for their enormous support and encouragement during my studies.

Declaration

I declare that the work presented in this thesis is based on my own research, except where specifically acknowledged in the text. Some parts of this thesis were previously published in B. G. Donoeva, D. S. Ovoshchnikov and V. B. Golovko, *ACS Catalysis*, 2013, 2986 and D. S. Ovoshchnikov, B. G. Donoeva, B. E. Williamson and V. B. Golovko, *Catalysis Science & Technology*, 2014, 4, 752; corresponding notes are made in the respective chapters.

List of Abbreviations

AAS – Atomic Absorption Spectroscopy

AR – Analytical Reagent

DMF – N,N-dimethylformamide

DR UV-vis – Diffuse reflectance UV-vis spectroscopy

ICP-MS – Inductively Coupled Plasma Mass Spectrometry

GC – Gas Chromatography

GC-FID – Gas Chromatograph equipped with Flame Ionisation Detector

GC-MS – Gas Chromatography Mass Spectrometry

LED – Light-Emitting Diode

MIL-101 – Matérial Institut Lavoisier-101 (type of MOF)

MOF – Metal-Organic Framework

NMR – Nuclear Magnetic Resonance

PPh_3 – triphenylphosphine

PXRD – Powder X-Ray Diffraction

S.D. – Standard Deviation

S.E. – Standard Error

SEM – Scanning Electron Microscopy

SPR – Surface Plasmon Resonance

TEM – Transmission Electron Microscopy

TGA – Thermogravimetric Analysis

THF – Tetrahydrofuran

TS-1 – Titanium Silicate

XPS – X-ray Photoelectron Spectroscopy

Chapter 1 - Introduction

1.1. Pathways to green oxidation processes

In the modern chemical industry oxidation processes and in particular oxidation of hydrocarbons play an important role in the production of functional organic compounds such as epoxides, ketones, alcohols, acids, *etc*. Oxidation is the second largest process after polymerisation with a share of *ca.* 30% of the total production by modern chemical industry.[1] However, currently oxidation processes heavily rely on the application of stoichiometric oxidants such as chromium salts, chlorine or organic peroxides, which leads to the formation of large amounts of by-products and toxic waste and increases the cost of production in the case of organic peroxides. In this respect, application of air or oxygen as an oxidant is an important pathway to a sustainable, environmentally friendly oxidation. The development of chemical processes focusing on process efficiency as well as on eliminating waste at the source and avoiding the use of toxic and hazardous compounds is the main target of Green Chemistry.[2] This aim cannot be achieved without the use of catalysts.

1.1.1. Catalysis

The importance of catalysis for modern society can hardly be overestimated: more than 95% of all produced products by volume are synthesised using catalysis, more than 80% of the added value in chemical industry is produced by means of catalysis, and *ca.* 20% of the world economy depends directly or indirectly on catalysis.[3] A catalyst is a substance that transforms reactants into products, through an

uninterrupted and repeated cycle of elementary steps in which the catalyst participates while being regenerated to its original form at the end of each cycle during its lifetime.[4]

A catalyst increases the rate of a reaction, but does not change the thermodynamics. An illustration of this principle for the activation of gas-phase reaction by a solid catalyst is shown in Figure 1.1. Here, the uncatalysed process proceeds through the activated state (1), over the energy barrier (energy of activation $E_{a,0}$). When a catalyst is introduced into the reaction the latter starts to proceed through a multi-step process. First, the reactant (A) is adsorbed on the surface of the catalyst (A_{ads}). Depending on the system, this process may or may not have an activation energy. Next, the adsorbed reactant is transformed into the product (P_{ads}) *via* a surface reaction with activation energy $E_{a,1}$, through the activated state (2). Finally, the product is desorbed with activation energy $E_{a,des}$. Both uncatalysed and catalysed processes have the same enthalpy of reaction $\Delta H_{reaction}$. Thus, the introduction of a catalyst provides an alternative pathway with smaller activation energies, which accelerates the reaction, but does not affect the equilibrium position.[5]

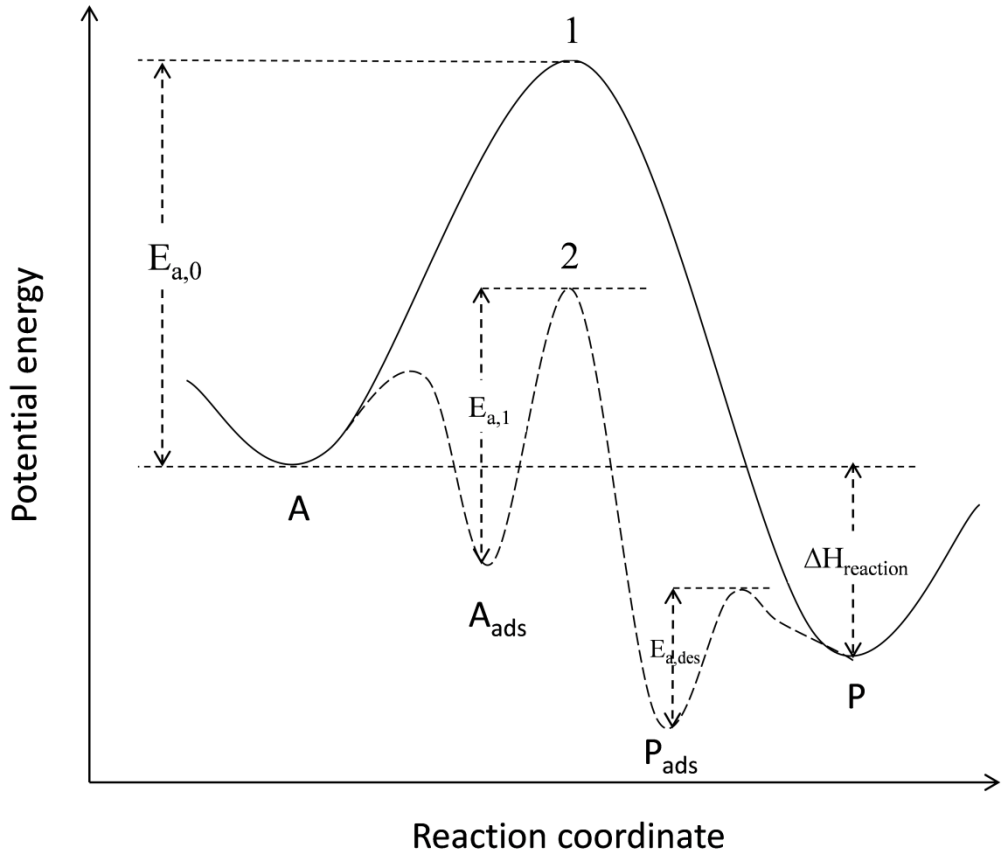

Figure 1.1 The course of the gas-phase reaction A → P, uncatalysed (solid line) or catalysed by a heterogeneous catalyst (dashed line).

Importantly, in addition to accelerating a reaction, the catalyst can favour one specific pathway to the desired product, when many pathways are possible. The energy profile diagram in Figure 1.2 depicts two possible pathways to products B and C. In the uncatalysed reaction, the product B will be formed faster because of the lower activation energy (given comparable Arrhenius constants for the two reactions). However, when a catalyst is introduced, the reaction proceeds through the adsorption of the substrate A on the catalyst's surface with subsequent formation of B and C. If the activation energy of the formation of product C from the adsorbed substrate A is now lower than the one for B, the formation of C will proceed faster. The reaction will

become more selective towards product C, even though it is not thermodynamically favourable.[6]

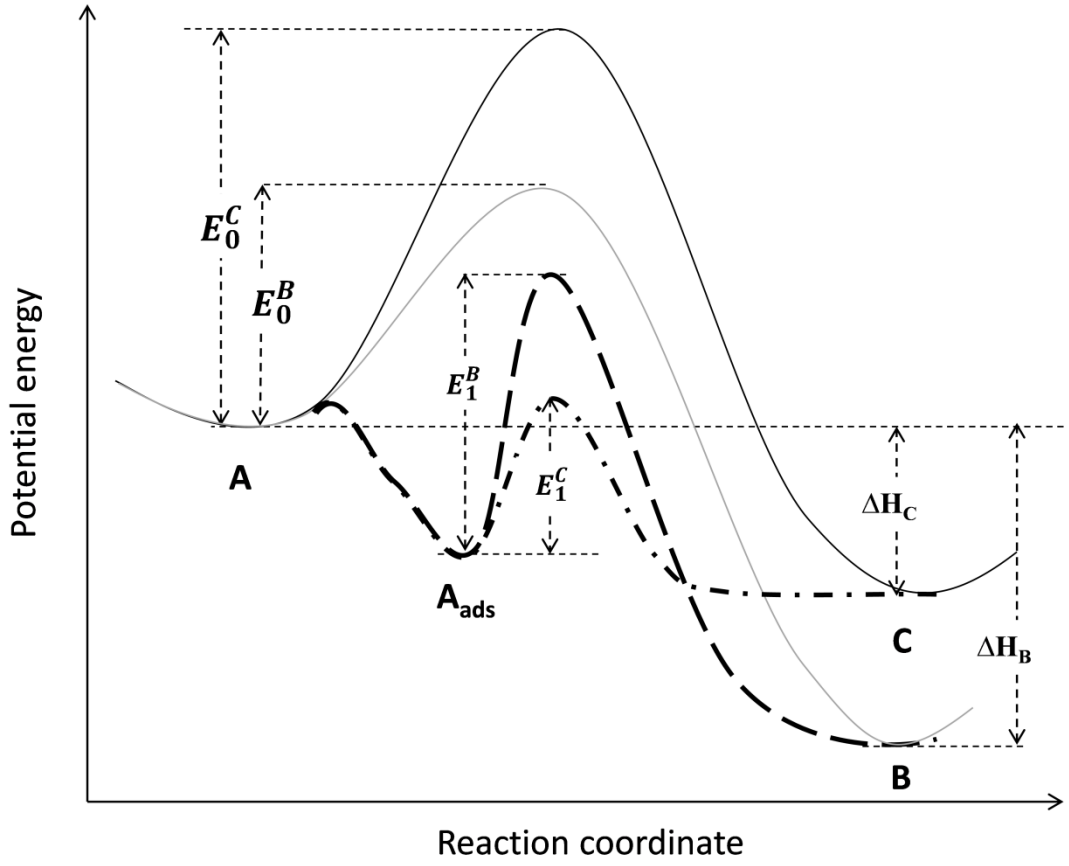

Figure 1.2 Scheme of the course of two parallel reactions A→B and A→C, showing how selectivity could be changed by a catalyst.

Catalysts are typically classified as heterogeneous, homogeneous or biocatalysts. Homogeneous catalysts are typically well-defined chemical compounds or coordination complexes, which are dispersed together with reactants in a reaction medium. Heterogeneous catalysts act between two phases; typically the catalyst is a solid and reactants are gases or liquids. Biocatalysts are protein molecules of colloidal size, some of them act in dissolved form in cells, while some are bound to cell membranes. Approximately 80% of all industrial catalytic processes are heterogeneous, 15% homogeneous and 5% use biocatalysts.[7] The major advantage of

heterogeneous catalysis is that they can be easily separated from the reaction mixture using simple methods such as filtration, centrifugation or even using magnetic attraction.[8] In the case of homogeneous catalysts, more complicated processes such as distillation, liquid–liquid extraction, and ion exchange must be used.[9] However, heterogeneous catalysts typically lack the activity and selectivity of the homogeneous catalysts. Thus, the development of highly active and selective heterogeneous catalysts is critical for the design of environmentally acceptable catalytic processes that minimise the production of undesired by-products, while preserving the advantage of easy separation of heterogeneous catalysts.

The use of multifunctional catalysts is one of the plausible approaches towards achieving high selectivity in chemical processes. Multifunctional catalysts can be defined as ones containing more than one type of active site, enabling them to carry out complex catalytic processes. Typically, such catalysts consist of metal nanoparticle-based active site and support material that has acidic, red/ox or other type of functionality. The dissociation of diatomic molecules, such as hydrogen or oxygen, is believed to occur at the metal nanoparticle sites, while subsequent rearrangement reactions of organic molecules, involving partial hydrogenation or oxidation, occur at the acidic or redox active sites.[10] An elegant example of utilisation of multifunctional catalysts to improve the selectivity of the process is the phenol hydrogenation process catalysed by palladium deposited on Al_2O_3: while palladium nanoparticles activate the hydrogen, the support, being a Lewis acid, activates the substrate and stabilizes cyclohexanone, preventing its over-hydrogenation to cyclohexanol.[11]

The vast majority of heterogeneous catalysts are nanostructured. The use of nanoparticles in catalysis is prompted by several factors: (a) higher dispersion leads to an increased number of surface atoms, which are the active sites of the process (Table

1.1) (b) with the decrease in size, the band structure begins to disappear, discrete energy levels become dominant and thus metal particle obtains properties different from those of bulk metals.[3]

Table 1.1 Decrease of the fraction of surface atoms for full-shell clusters.[3]

Full-shell clusters[12]	Total number of atoms	Number of surface atoms	Surface atoms, %
1 shell	13	12	92
2 shells	55	42	76
3 shells	147	92	63
4 shells	309	162	52

These effects play an important role in nanostructured gold catalysts utilisation of which is a promising pathway toward greener processes.[13]

1.1.2. Gold-based catalysts

Gold was traditionally regarded as a poor catalyst compared to other precious metals until the discovery in the 1980s that gold becomes a very active catalyst once it is dispersed in the form of nanoparticles deposited on supports. The first report on the activity of gold as a catalyst came out earlier in 1973, which showed the activity of gold in olefin hydrogenation,[14] but the booming interest in catalysis by gold was sparked a decade later by reports on the catalytic activity of gold in the low-temperature oxidation of CO (Haruta *et al.*)[15] and hydrochlorination of ethyne to vinyl chloride (Hutchings).[16] Since these discoveries, gold-based catalysts were shown to catalyse various types of chemical transformations, including selective aerobic oxidation reactions.[17, 18]

Aerobic alkene oxidation

Propene oxide is used on a large scale in the production of polyurethanes. It is generated *via* the chlorohydrin process or by oxidation using organic hydroperoxides.[19] Significant progress in the utilisation of oxygen as an oxidant for propene epoxidation was achieved by using supported gold catalysts. Early reports showed propene oxide selectivities above 99%, at propene conversions around 1%, obtained using Au/TiO_2 as a catalyst.[20] Au/TS-1 was shown to be one of the best gold-based catalysts for propene epoxidation – utilisation of this catalyst allowed achieving selectivities over 80% at conversions around 5%.[21, 22] A number of major chemical companies including Bayer, Dow and Nippon Shokubai hold patents for the production of propene oxide using gold catalysts, with pilot plants operating within the industry.[23] Interestingly, propene epoxidation on gold catalysts requires presence of H_2 as a sacrificial agent. It was suggested that the mechanism of epoxidation is most likely to include the step of generation of hydrogen peroxide, promoted by gold nanoparticles (Figure 1.3).[24] Later reports, however, showed that H_2 could be substituted with safer water vapour that can generate hydroperoxidic species on the surface of nanoparticles.[25, 26]

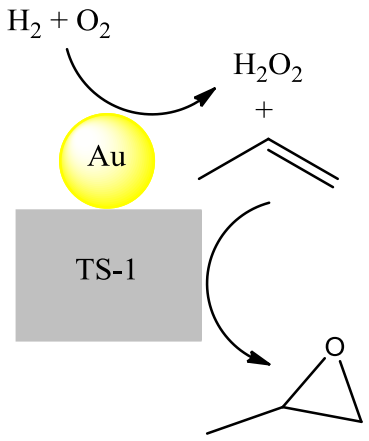

Figure 1.3 Probable mechanism of propene epoxidation on Au/TS-1.

Supported gold nanoparticles were found to be active in selective liquid-phase oxidation of various alkenes including cyclohexene, cis-cyclooctene, styrene and stilbene.[27] The first report on the catalytic activity of carbon-supported Au nanoparticles in alkene oxidation by Huges *et al.* showed that oxidation of alkenes required the presence of a radical initiator, such as *tert*-butyl hydroperoxide. The selectivity of the oxidation of alkenes, cyclohexene in particular, could be tuned by the proper choice of solvent.[28] When silicon nanowires were used as a support for gold nanoparticles improved activity in the oxidation of cyclooctene was reported.[29]

In the absence of radical initiator, gold nanoparticles supported on promoted manganese oxide octahedral molecular sieves were shown to catalyse the oxidation of cyclohexene. However, in this case instead of epoxidation, allylic oxidation of cyclohexene was achieved under solvent-free conditions.[30]

Oxidation of styrene, catalysed by supported gold nanoparticles, was also found to be possible in the absence of a radical initiator, though low activity and poor selectivity towards epoxide were reported.[31]

Aerobic alkane oxidation

Oxidation of cyclohexane represents an industrial interest as a pathway for production of cyclohexanone-cyclohexanol mixture (KA-oil), which is used in nylon production (Figure 1.4).[32]

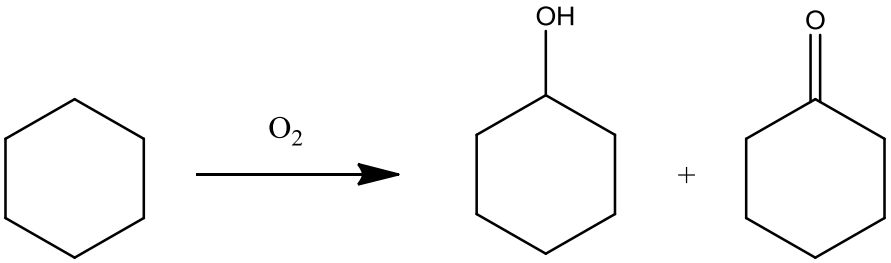

Figure 1.4 Oxidation of cyclohexane to cyclohexanol and cyclohexanone.

Early reports claimed that gold nanoparticles supported on mesoporous SiO_2,[33, 34] graphite[35] and Al_2O_3[36] were able to catalyse the conversion of cyclohexane to KA-oil with high selectivity. However these claims were later questioned by a report that showed that the reaction proceeds *via* a purely radical pathway and could be fully inhibited by radical scavengers.[37] The most recent investigation of the mechanism of cyclohexane oxidation by Hutchings *et al.* came to the conclusion that gold is capable of acceleration of the reaction without the need for initiators, which makes it by definition a catalyst for the reaction, but this acceleration occurs by increasing the concentration of hydroperoxide/peroxide species that promote catalytic autoxidation *via* radical-chain mechanism.[38]

Aerobic oxidation of toluene

Bimetallic Au-Pd nanoparticles supported on carbon and TiO_2 were found to be capable of catalysing the aerobic oxidation of toluene to benzyl benzoate, with a yield of latter reaching 90%.[39] The scope of substrates was expanded to 2-, 3- and 4-methoxytoluene and 2-, 3- and 4-nitrotoluene, showing that this methodology is applicable to substituted toluenes as well.

Aerobic alcohol and polyol oxidation

Oxidation of alcohols to carbonyl and carboxylic compounds is an important reaction to produce attractive chemicals for organic synthesis; therefore, the aerobic oxidation of alcohols using gold catalysts has been widely investigated.[13, 18, 27, 40, 41]

Early reports described alcohol oxidation using Au nanoparticles supported on conventional supports, such as carbon, Al_2O_3, SiO_2 and TiO_2.[42-46] The presence of base was found to be essential for catalytic activity. During further development of gold-based catalytic systems for alcohol oxidation more sophisticated materials were utilised as supports. Examples include carbon nanotubes,[47] ceria,[48] mesoporous

silica,[49] Ga-Al mixed oxide composites[50] and metal-organic frameworks.[51, 52] Importantly, the use of the metal-organic framework MIL-101 promoted alcohol oxidation without the need for added base.[52]

Thermally stable alcohols (C_2-C_5) were oxidised to the corresponding aldehydes and ketones in gas-phase over gold nanoparticles supported on SiO_2 at temperatures ranging from 100 ºC to 300 ºC.[53, 54] Interestingly, it was shown that 6 nm nanoparticles were more active than 3.2 nm and 8 nm ones in ethanol oxidation.

Liquid-phase oxidation of alcohols is typically performed on supported nanoparticles, but unsupported gold catalysts, such as Au(I) complex[55] or unsupported polyvinylpyrrolidone-stabilised Au nanoparticles,[56] were also demonstrated to be active in the liquid-phase alcohol oxidation.

Alloying of Au with Pd was shown to have an impact on catalyst activity and selectivity in alcohol oxidation. For example, Au-core Pd-shell nanoparticles supported on TiO_2 showed the highest selectivity towards benzaldehyde in the oxidation of benzyl alcohol, with activity between those of monometallic Au and Pd catalysts.[57] In another example, bimetallic Au-Pd nanoparticles supported on carbon showed superior activity in glycerol oxidation compared with both Pd and Au counterparts.[58] By using Au-Pt alloys supported on H-mordenite high conversion and selectivity were achieved in the base-free oxidation of glycerol in aqueous media.[59] However, the synergistic effects between gold and other metals are not always positive. Thus, monometallic Au nanoparticles supported on CeO_2 were found to be more active and selective in the oxidation of allylic alcohols compared with bimetallic Au-Pd counterpart.[60] This was attributed to the stability of metal hydrides that were not rapidly oxidised in case of Pd-containing catalysts. The high concentration of Pd-

H hydrides was sufficient to promote C-C bond isomerisation and reduction, leading to the formation of by-products.

Amine oxidation

Gold was found to be capable of promoting the aerobic oxidation of amines to imines (Figure 1.5, reaction 1). Interestingly, both bulk gold (particle size *ca.* 10^3 nm)[61] and large gold nanoparticles (50 – 150 nm) deposited on Al_2O_3 were catalysing the reaction, although the latter were understandably much more active.[62] The superiority of gold nanoparticles supported on carbon as compared to bulk gold powder was also reported in the oxidation of cyclic and acyclic benzylic amines.[63] The same report additionally demonstrated the ability of Au nanoparticles to catalyse the oxidation of N-substituted 1,2,3,4-tetrahydroisoquinolines to the corresponding amides in the presence of aqueous $NaHCO_3$ solution. Another report showed that Au nanoparticles supported on TiO_2 could be utilised for the one-pot synthesis of secondary benzylamines *via* a two-step process of oxidative cross-condensation of amines with subsequent hydrogenation of the resulting imine.[64]

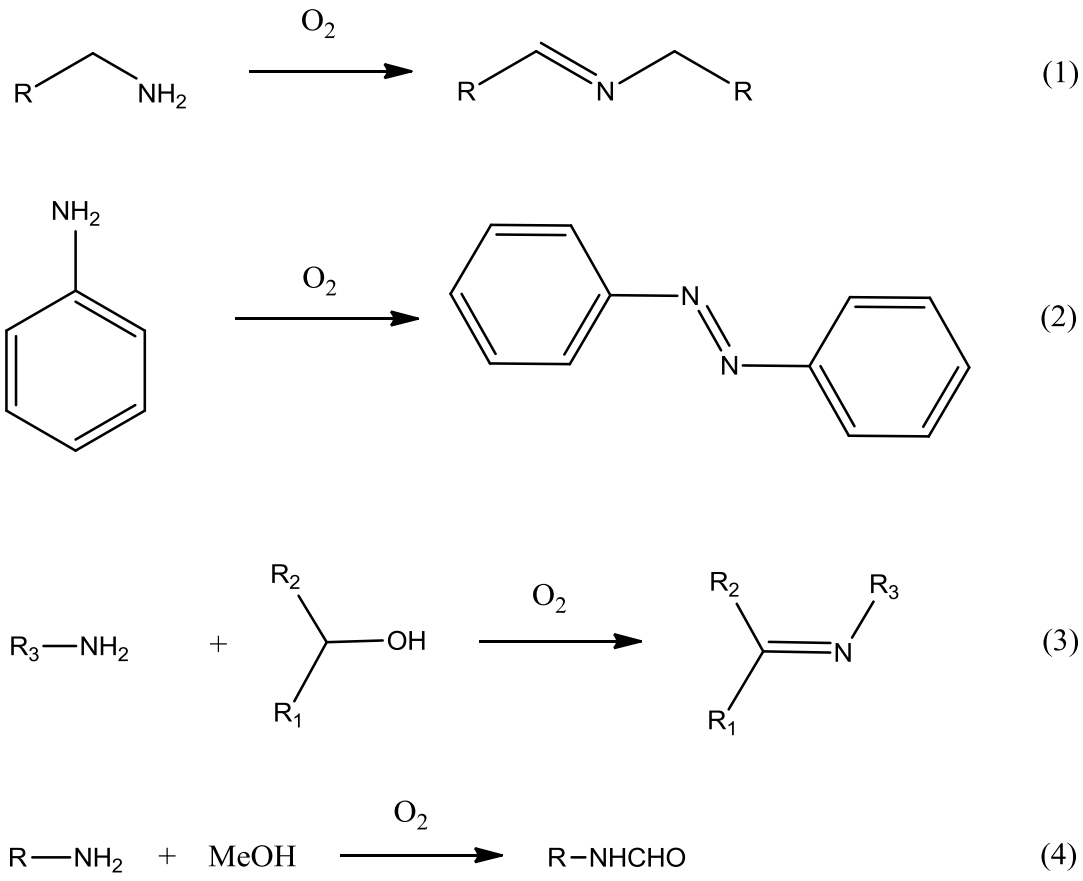

Figure 1.5 Various transformations of amines catalysed by gold catalysts.

Au nanoparticles supported on TiO_2 can also catalyse the aerobic oxidation of anilines to aromatic azo compounds (Figure 1.5, reaction 2).[65, 66] Another report demonstrated a novel green route to an important nylon-6 precursor caprolactam *via* the aerobic oxidation of 1,6-hexanediamine using Au/TiO_2.[67] The same catalyst was shown to catalyse imine formation *via* the oxidative coupling of alcohols and amines (Figure 1.5, reaction 3).[68] Au nanoparticles supported on NiO were shown to catalyse N-formylation of amines with methanol and oxygen to produce formamides (Figure 1.5, reaction 4).[69]

Preparation of heterogeneous gold catalysts

The catalytic activity of supported gold nanoparticles is largely affected by the method of preparation. Moreover, different reactions have their own requirements for

the ideal structure of the active site, and therefore methods of catalyst preparation become an important tool for tuning the properties of a catalyst. Methods of gold catalysts preparation can be divided into two classes: (a) those in which the gold precursor is deposited on the preformed support and (b) those in which the support and the gold species are formed at the same time.[70]

The first class includes the simplest method of *impregnation*, which was used for the preparation of the very first supported gold catalysts.[71] In this method the pores of support are filled with a solution of gold precursor. If the volume of the latter is equal to the pore volume of the support, the method is called impregnation to incipient wetness. When an excess of solution is used, the solvent is then removed by evaporation. Typical gold precursors include chloroauric acid $HAuCl_4$,[71, 72] gold chloride $AuCl_3$[73, 74] and ethylenediamine complex $[Au(en)_2]Cl_3$.[75, 76] The method can be used with any type of support. Quite often chlorine is left on the surface of the support, which leads to the formation of large gold nanoparticles during the subsequent thermal treatment.[77, 78] Additionally, chlorine can act as a poison for some catalytic reactions. These drawbacks of impregnation method could be avoided by the application of *coprecipitation* or *deposition-precipitation* methods.

In the *coprecipitation* method catalysts are prepared by adding aqueous alkaline solution to an aqueous solution of $HAuCl_4$ and water-soluble metal salt – a precursor of the support.[15] The rise in pH leads to a simultaneous precipitation of support and gold entities. The precipitate can be then washed with copious amounts of water to remove chlorine and sodium ions prior to calcination. The drawback of this method is that some of gold particles could be embedded in the bulk of the support material.[79]

The *Deposition-precipitation* method was first used by Haruta *et al.*[80] to obtain supported gold nanoparticles, and since then has become one of the most commonly

used procedures. In this method $AuCl_4^-$ is hydrolysed in the presence of solid support by raising the pH of the solution and aged at 343 K or 353 K to form insoluble $Au(OH)_3$ which deposits on the support during precipitation. The solid is then washed with water to remove sodium and chlorine and calcined. This method works well for supports that have a point of zero charge (PZC) greater than five, such as MgO, TiO_2, Al_2O_3, ZrO_2 and CeO_2, but is not suitable for SiO_2 (PZC *ca.* 2), silica-alumina (PZC *ca.* 1) and WO_3 (PZC *ca.* 1).[81] The resultant gold loading and the size of formed nanoparticles depend on the pH at which deposition-precipitation was performed.[82, 83] Thus, it is not always possible to achieve complete deposition of gold for a desired particle size. This disadvantage could be overcome by using a modified methodology that uses urea as a "delay base". Because the hydrolysis of urea in the suspension of support in aqueous metal salt solution only occurs upon heating above 333 K a gradual and homogeneous release of hydroxyl ions and increase in pH throughout the solution takes place.[70] In this method all the gold in solution can be deposited on the support, while control over the particle size of gold is maintained.[84, 85]

Another method for obtaining supported gold nanoparticles of desired size distribution is to use *pre-synthesized colloids or metal clusters*. Gold is able to form reliably persistent colloidal dispersions if stabilised by ligands. Mercaptans, phosphines, phosphine oxides, quaternary ammonium salts, citrate, polymers and dendrimers can be used as ligands in the preparation of gold nanoparticles.[86-89] Gold nanoparticles can be immobilised by dipping the support into the colloidal suspension. The use of this method is advantageous because particle size can be controlled independently, the size distribution is narrow, and the gold is in reduced form.

Incorporation of gold nanoparticles within porous supports can be performed using gold nanoparticles covered with protecting ligands as templates for the synthesis

of support materials. In one example of this method Au_{55} particles encapsulated by amine-terminated fourth-generation dendrimers were incorporated into an amorphous titania network upon hydrolysis and condensation of $Ti(O^{i}Pr)_4$ alkoxide.[90] In another example, using inverse water-oil emulsions, gold nanoparticles were synthesized by reduction with hydrazine in the presence of a mixture of two ligands, 1-dodecanethiol and 3-mercaptopropyltrimethoxysilane. In a second step, 3-mercaptopropyltrimethoxysilane of gold nanoparticle ligand shell was co-condensed with tetraethyl othosilicate to form a porous silica material that enclosed the gold nanoparticles. 1-dodecanethiol was acting as a spacer preventing nanoparticles from complete occlusion by silica during the gelification process. Such an isolation of gold nanoparticles within the silica domains significantly hindered the sintering of gold nanoparticles.[91]

There is a variety of less commonly used methods for the preparation of supported gold catalysts. In the *chemical vapour deposition* method a volatile organogold compound decomposes to gold nanoparticles upon reaction with the surface of the support.[92, 93] In *photochemical deposition* gold ions are reduced by photogenerated electrons of semiconducting supports under UV irradiation.[94, 95] Gold nanoparticles can also be deposited by *ultrasound*. The latter can induce the homolytic dissociation of water into $H^{\bullet}$ and $OH^{\bullet}$ radicals due to the formation and implosive collapse of bubbles in liquid. $OH^{\bullet}$ radicals in turn reduce gold ions.[96-98] In another method the volatile organogold complex $Me_2Au(acac)$ (acac = acetylacetonate) and the support are ground in an agate mortar in air at room temperature. The mixture is then treated with hydrogen at elevated temperature. It was proposed that the *solid grinding* induces the sublimation of $Me_2Au(acac)$ which is then uniformly distributed within the pores of the support *via* rapid diffusion.[51, 99]

1.1.3. Photocatalysis

Another approach to make chemical process "greener" is the utilisation of photocatalysts, in particular catalysts that can utilise sunlight.[100] First, it gives access to an abundant source of energy, such as sunlight. Second, the utilisation of such catalysts allows one to manipulate the selectivity of the chemical reaction.[101] Third, it allows one to perform reactions under reduced temperatures thus slowing unwanted reactions or to conduct transformations of thermally unstable compounds.

Traditionally, semiconductors were used as photocatalysts to drive various chemical transformations.[102] Semiconductors have a band structure in which the conduction band is separated from the valence band by a band gap. A flux of photons with energies greater than the band gap can be absorbed by a semiconductor, which leads to the formation of electrons and holes in the conduction and valence bands, respectively.[103] The charge carriers then diffuse to catalytically active sites where they drive chemical transformations. For example, in photocatalytic water splitting (Figure 1.6) photogenerated holes participate in the formation of O_2 half-reaction ($H_2O + 2h^+ = 2H^+ + 1/2O_2$), while photogenerated electrons are involved in the generation of hydrogen ($2H^+ + 2e^- = H_2$).[104]

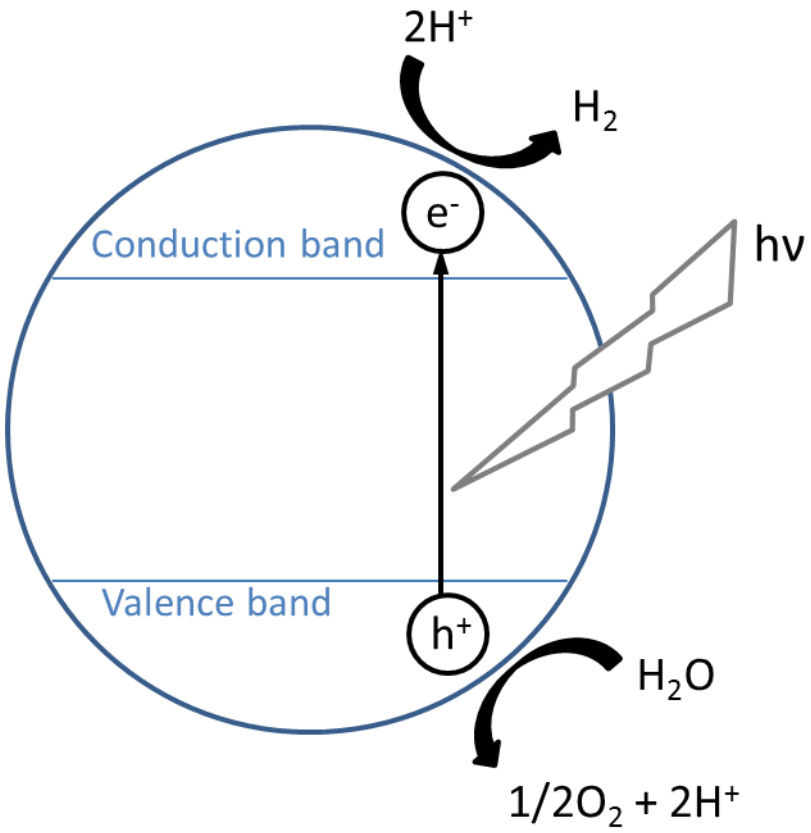

Figure 1.6 Schematic representation of photocatalytic water splitting on a semi-conductor particle.

However, pure semiconductors have many drawbacks, such as having a large band gap (e.g., TiO_2 with ~3.2 eV), which allows the photocatalyst to absorb only UV light. Because the later represents only ~5% of the solar spectrum, these semiconductor materials are inefficient catalysts for the utilization of sunlight. Semiconductors with narrower band gaps often suffer from poor catalytic activity and/or low mobility of charge carriers.[102] The wide band gap limitation can be partially overcome when the semiconductor is used to drive transformations of substrates that contain electron-rich heteroatoms (O, S or N). In this case, the substrates are adsorbed on the semiconductor surface, which creates new electron donor level above the valence band from the 2p orbital of O and N or 3p orbital of S,

leading to visible light absorbance (Figure 1.7). Under visible light irradiation electron from heteroatoms is injected into the conduction band of the semiconductor. The positive charge generated on the heteroatoms can lead to the functionalization of heteroatoms or adjacent C-H bonds.[105]

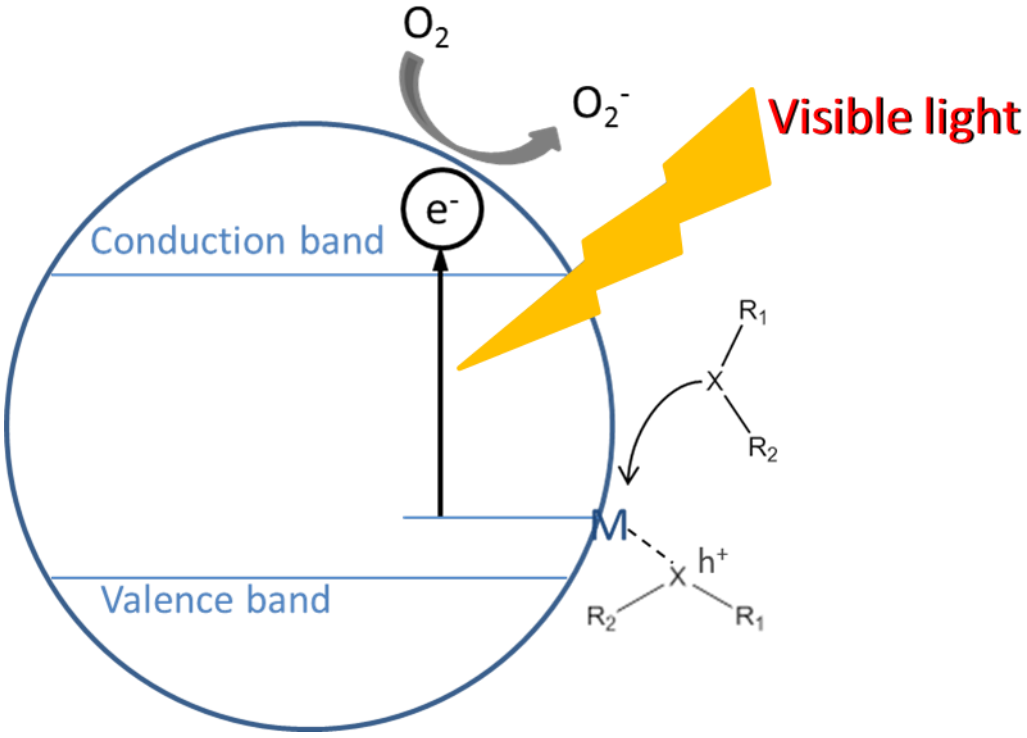

Figure 1.7 Schematic representation of the photocatalytic process under visible light irradiation facilitated by adsorption of heteroatom-containing (X = N, O or S) substrate.

Examples of chemical transformations driven by the described mechanism include the oxidation of alcohols to aldehydes catalysed by TiO_2[106] or Nb_2O_5,[107] the sulfoxidation of alkanes over TiO_2[108] and the oxidation of amines to imines over various semiconductors.[109, 110]

Another way to overcome the limitations of pure semiconductor photocatalysts and broaden the spectrum of utilised light is the application of multifunctional metallic material/semiconductor photocatalysts. The absorption of visible light by nanosized

metallic materials can occur due to interband transitions and/or *via* surface plasmon resonance.[111] Surface plasmon resonance (SPR) is the collective oscillation of electrons in a solid or liquid, which is stimulated when the frequency of the incident light photons matches the natural frequency of surface electrons oscillating against the restoring force of positive nuclei.[112] The most common plasmonic materials are metals, such as gold, silver and copper.[112, 113] SPR can also occur in conducting metal oxides and semiconductors with sufficient free carrier densities.[114-116]

There are several mechanisms of how SPR materials can enhance the creation of charge carriers, thus driving photochemical transformations.[102] The most commonly used mechanism to describe the photocatalytic processes driven by SPR material supported on semiconductor is shown in Figure 1.8. Here, under visible light irradiation electrons are photoexcited to surface plasmon states, with holes (positive charges) left below the Fermi level. Electrons are then injected into the conduction band of the semiconductor and transferred to electron acceptors, such as O_2. The holes in turn react with organic substrates thus completing photocatalytic cycle.[105]

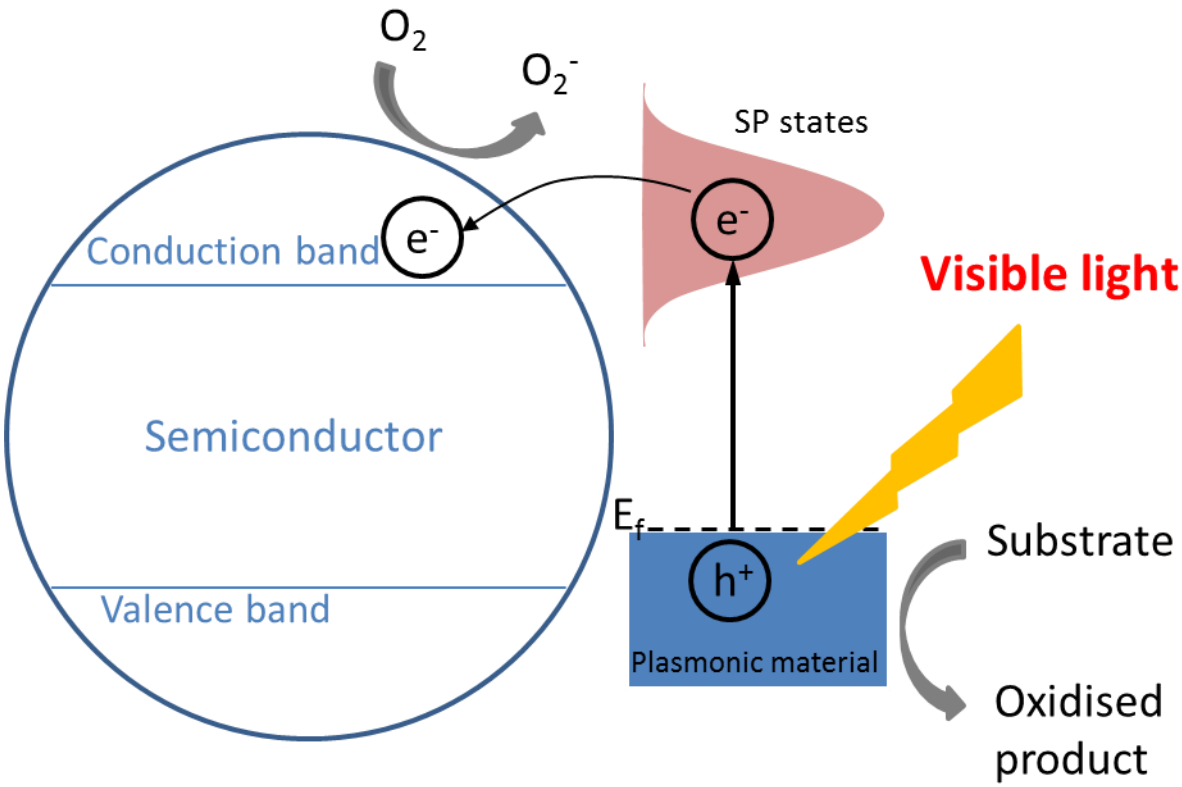

Figure 1.8 Schematic representation of a photocatalytic process under visible light irradiation driven by plasmonic material/semiconductor catalyst.

In a different mechanism, plasmonic structures generate strong electric fields under photo-excitation. Because the rate of electron-hole formation in a semi-conductor is proportional to the intensity of the electric field, the generation of electric fields by a photoexcited plasmonic material accelerates the generation of charge carriers in the semiconductor, located near plasmonic nanostructures.[117] In a third mechanism, large plasmonic nanostructures scatter photons, thus increasing the photon path through the semiconductor, which, in turn, accelerates electron-hole generation.[118]

Interestingly, plasmonic metals supported on insulators or semiconductors with very large band gaps can also utilise visible light in photocatalysis. In this case photogenerated electrons are donated into adsorbate (reactant) states/orbitals forming

negative ion species rather than being injected into the conduction band of the semiconductor.[102, 119]

Various plasmonic metal-based photocatalytic systems capable of utilising visible light irradiation have been developed in recent years. Photocatalysed reactions include the aerobic oxidation of alcohols driven by Au/TiO_2,[120, 121] Au/CeO_2,[122, 123] bimetallic $Au\text{-}Pd/ZrO_2$[124] and $Au\text{-}Cu/TiO_2$;[125] the aerobic oxidation of amines over Au/TiO_2[126] and $Au\text{-}Pd/ZrO_2$;[124] the reduction of nitroaromatic compounds over Au/ZrO_2[127] and Au/TiO_2;[128] Suzuki-Miyaura cross-coupling driven by $Au\text{-}Pd/ZrO_2$;[124] and several other reactions.[105, 129]

The absorption of light in the visible region by some metallic materials, such as metals Pt and Pd, and metallic oxides RuO_2 and IrO_2, is dominated by interband transitions.[130-132] This phenomenon can also be utilised in photocatalysts. For example, in the case of Pt metal absorption of visible light occurs *via* the interband transition of 5d band e^- to the 6sp conduction band which is then injected into the conduction band of the semiconductor and produces O_2^- species analogously to the plasmonic mechanism described above. This mechanism was suggested for the aerobic oxidation of alcohols photocatalysed by Pt nanoparticles deposited on anatase[133] and Pt-Cu bimetallic nanoparticles supported on anatase.[134]

1.2. Scope of this work

The goal of the work within this thesis was to develop heterogeneous catalytic systems that utilise oxygen as the sole oxidant and are capable of operating under mild, environmentally friendly conditions. Two different pathways were explored.

The first part of the thesis was focused on the development of gold-based catalysts and the study of how their selectivity could be tuned using various supports or co-catalysts. Investigation of the optimal catalyst structure for solvent-free aerobic

oxidation of cyclohexene was performed. Particular focus was made on the size of supported gold nanoparticles.

The aim of the second part of the thesis was the development of hydrous ruthenium oxide-based photocatalyst capable of utilising visible light irradiation for the aerobic oxidation of amines. The ability of the catalyst to work under sunlight irradiation and use water as a solvent was investigated. The scope of the reaction and its mechanism were also investigated.

Chapter 2 Characterisation methods

This Chapter describes basic principles and instrumentation of some of the main characterisation methods used throughout this thesis.

2.1. Gas Chromatography (GC)

The most frequently used method during the work described in this thesis is gas chromatography. Gas chromatography was used for the qualitative and quantitative analysis of the composition of mixtures of compounds obtained during catalytic reactions.

Gas chromatography is a method used for the separation and analysis of compounds in which the components of the sample partition between two phases.[135] The first phase is a stationary bed; the other is a gas that percolates through the stationary bed. The sample is vaporized in the injector and carried by the mobile gas phase through the column (Figure 2.1). The separation of the components of the mixture occurs due to the differences in vapour pressures and affinities for the stationary bed. This causes each component to elute from the column at different times, known as the retention times of the compound. After the column the carrier gas, together with compounds, passes through a detector.

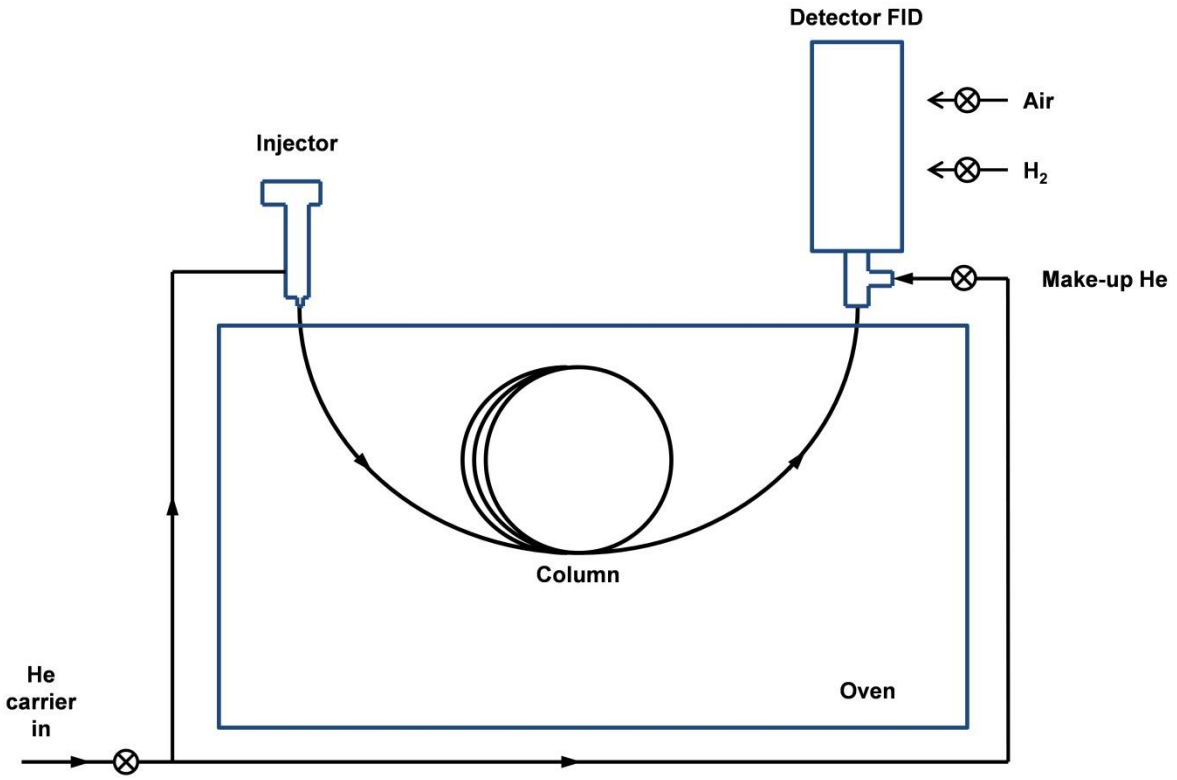

Figure 2.1 Scheme of gas chromatograph equipped with flame ionisation detector.

The state of stationary phase could be either a solid (Gas-Solid Chromatography) or a liquid (Gas-Liquid Chromatography). Gas-Liquid Chromatography is more widespread and is used in this work. The liquid used as a stationary phase is held inside the column using either of two methods. In packed columns the liquid is coated on an inert solid support with a high surface area, which is tightly dry-packed into the column. In more widely used capillary columns the liquid is coated on the inside of the capillary. Often, the liquid is cross-linked and sometimes it is chemically bonded to the surface of the fused silica.

The column is placed in the oven that provides the control over the temperature, which is an important tool for influencing the retention times of the components and their separation.

The most-often-used types of detectors are flame ionisation detectors (FID) and mass spectrometers (MS). In FID, the column effluent is burned in an air-hydrogen flame, which produces ions and thus causes the formation of current in a collector electrode. The current represents a signal that is proportional to the carbon content and is affected by the presence of heteroatoms in the compound. GC-FID could be used for both qualitative and quantitative analysis. The latter was performed in this work using an internal standard method. In this method, calibration mixtures with known concentrations are prepared from pure samples of analytes, together with a standard compound. The latter is also added to the reaction mixture in a known concentration. Peak areas determined from the chromatogram are then referenced to the area of the internal standard and calibration coefficients are extracted from the calibration curves. Qualitative analysis could, in principle, be performed on GC-FID by comparing the retention times of compounds in the sample with the retention times of known individual compounds; however GC-MS should be used when mixture composition is unknown and/or individual components are not available.

In GC-MS, effluent from the GC column is usually ionised using an electron impact technique in which high-energy electrons excite neutral analyte molecules causing the loss of electrons and fragmentation. The charged particles are then delivered into the mass-analysers where they are separated by their mass-to-charge (*m/z*) ratio by either magnetic or electrical fields. The mass spectrum is generated as a plot of ion abundance as a function of *m/z*. The presence of fragments with certain *m/z* and their abundance are characteristic for each compound and are used for their identification.

2.2. Transmission Electron Microscopy (TEM)

Transmission Electron Microscopy was used in this work for the imaging of gold nanoparticles/clusters and the measurements of their sizes. Electron microscopy offers much higher resolution compared to light microscopy due to the shorter wavelengths of electrons used for microscope illumination (*ca.* 10000 times shorter than visible light wavelength).

TEM has similar components to the ones of a light microscope: light source, condenser lens, sample stage, objective lens and projector lens (Figure 2.2).[136] Because an electron ray is used in TEM instead of visible light ray, optical lenses are substituted with electromagnetic lenses and a high-vacuum environment is required along the path of the electron beam in order to prevent collisions between electrons and air molecules. Unlike visible light, electron beams cannot be observed by a naked eye, so phosphorescent plates or special CCD cameras are used for image formation for viewing. The sample for TEM should be very thin to permit transmission of the electron beam. The thickness of the specimen should typically be about 100 nm, depending on the atomic weight of the specimen materials.

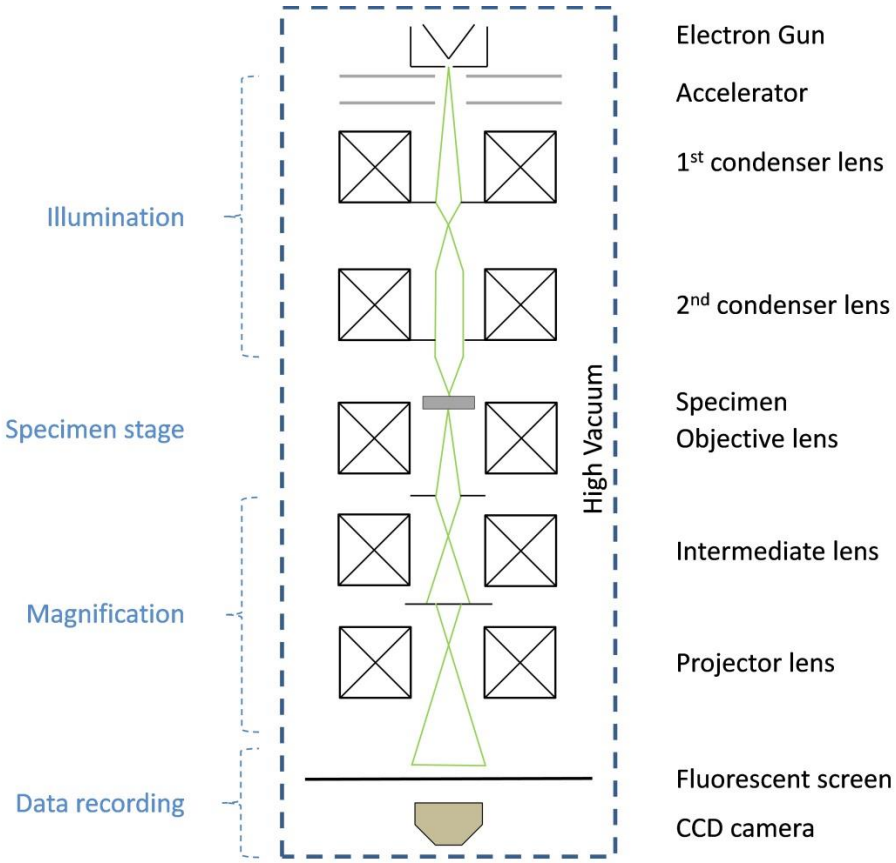

Figure 2.2 Scheme of transmission electron microscope.

The electron beam in TEM is generated by an electron gun, with thermionic emission gun being the most common type. In the latter, the filament (tungsten or LaB_6) is heated by an electric current leading to the emission of electrons, which are then accelerated by a high electrical voltage between the filament and the anode. The electron beam is then directed to the sample using a set of electromagnetic lenses and apertures; the latter are used to limit light scattering and/or to select diffracted or non-diffracted beams.

When passing through the sample, electrons are deflected from their primary direction by the sample. The contrast in the TEM image is generated based on the difference in the number of electrons scattered away from the transmitted beam. Electron scattering can create contrast in images by mass-density contrast and

diffraction contrast mechanisms. The latter is only applicable for crystalline specimens and is based on the capability of parallel crystal planes to scatter electrons. For amorphous materials, only mass-density contrast can be utilised. This type of contrast is based on the scattering of the electrons by atomic nuclei. The amount of scattering at any point of the sample depends on the product of thickness and density at that point. Thus, the differences in these parameters will generate variations in electron intensity on the image screen.

2.3. X-Ray Photoelectron Spectroscopy (XPS)

X-ray Photoelectron Spectroscopy (XPS) is a technique used for chemical analysis of the sample surface.[137] The fundamental event of XPS is photoionisation. The sample is irradiated with soft X-rays, causing electrons from core levels with binding energies E_b to be photoejected with kinetic energy $E_{kin} = h\nu - E_b$, where ν is the frequency of the photons. Measuring the kinetic energies of the photoejected electrons permits the calculation of binding energies, which are characteristic for each element. The binding energies could be "shifted" due to different oxidation states of an element, *e.g.* the typical binding energy of Au^0 is 84.0 eV, Au^+ - 85.0 eV and Au^{3+} - 85.9 eV. The technique is applicable for all elements except H and He, which do not have characteristic atomic core levels.

Peaks in XPS are named as *nlj*, where *n* is the principal quantum number, *l* is the angular momentum quantum number and *j* is defined as $j = l + s$ (where *s* is the spin angular momentum number and can be ±½). *p*, *d* and *f* orbital levels give rise to a doublet due to the spin-orbit splitting or $j - j$ coupling. For example, Au4f level gives rise to two peaks: $Au4f_{7/2}$ and $Au4f_{5/2}$.

The X-ray source in lab-based instruments is usually an aluminium- or magnesium-anode X-ray tube, with source energies of Mg Ka, 1253.6 eV and Al Ka,

1486.6 eV. Alternatively, synchrotron radiation could be employed, which gives several advantages:

- Bright synchrotron sources provide high intensity and high resolution.
- Variable source energy permits separation of photoemission lines, which vary in energy with the change of energy of the exciting source, from Auger lines, which remain constant in energy.
- The source energy could be tuned to increase the absorption cross-sections for certain elements thereby increasing the intensity of its peaks.
- The energy of the source can also be tuned to vary the kinetic energy of photo-excited electrons, which leads to a change in depth sensitivity of the measurements.

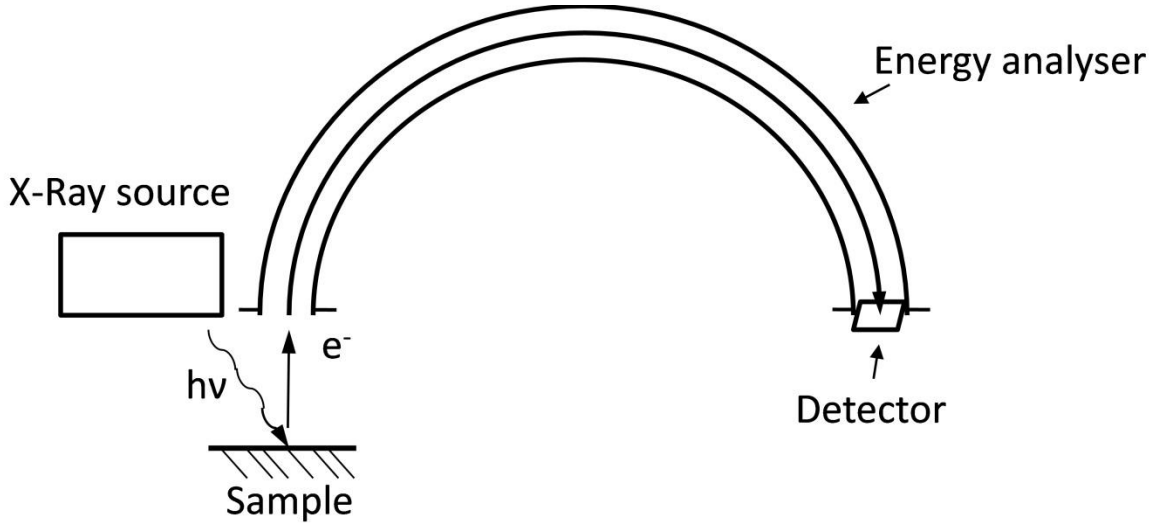

Figure 2.3 Scheme of photoemission spectrometer, which is entirely enclosed in ultra-high-vacuum chamber.

XPS is a very surface sensitive technique due to the fact that only electrons that are not inelastically scattered after formation give rise to XPS photopeaks. The ones that are inelastically scattered contribute only to the background in the spectrum. The

escape depth of the electron depends on its kinetic energy, *i.e.* electrons with high kinetic energy escape from greater depths in the analysed sample.

2.4. Atomic Absorption Spectroscopy (AAS)

AAS is employed to quantitatively determine chemical elements. In this work, AAS was used to measure gold concentration in solutions obtained from the dissolution of supported gold nanoparticles in order to establish catalyst gold loadings.

The underlying principle of AAS is based on the fact that, upon irradiation with light, atoms are excited to another electronic state by absorbing light at a certain wavelength, which depends on the nature of the element (for example, Au absorbs at 242.8 nm).[138] For each element there can be several excited states with definite energies, thus atomic spectrum consists of discrete lines, including resonance lines – lines which arise due to the transition from the ground state to excited states. Since these lines are extremely narrow (in the order of a few picometers) and unique to each element, AAS is highly element-selective.

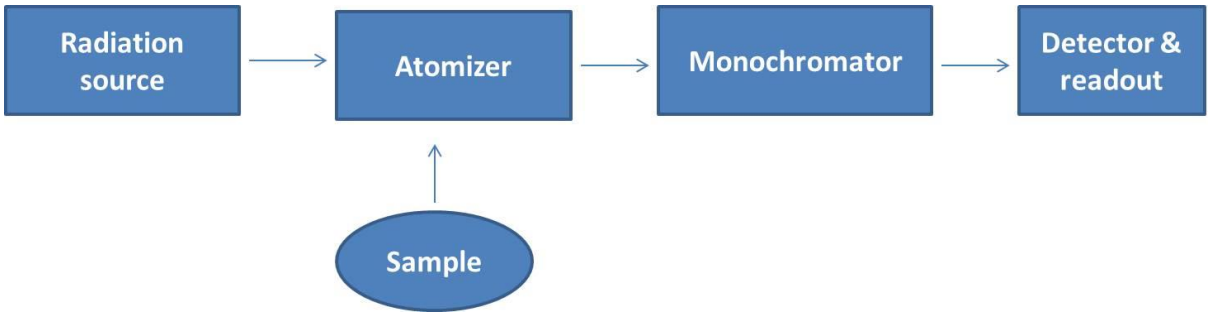

Figure 2.4 Diagram of Atomic Absorption Spectrophotometer.

In order to analyse element concentrations, a sample in a form of a solution is injected into a flame (an air-acetylene flame was used in this work) where it is atomized. When the light of the resonance wavelength is passed through a flame containing atoms of the element, a fraction of light is absorbed, and the extent of

absorption is proportional to the number of atoms present in the flame. The radiation flux with and without atoms of the element in the flame is analysed using a detector, and the ratio between the two values gives an absorbance value, which can be converted to concentration (or mass) using calibration curves. A hollow-cathode lamp specific for Au was used as a radiation source in this work.

2.5. UV-vis spectroscopy (UV-vis)

UV-Visible spectroscopy provides information about electronic transitions that occur in material under irradiation with ultra-violet (UV) and/or visible light.[139] In a UV-vis experiment, the absorption of light as a function of wavelength is measured. The fraction of light transmitted is described by the Beer-Lambert law:

$$\frac{I}{I_0} = e^{-\sigma(N_1 - N_2)l}$$

which states that the fraction of the light measured after interaction with the sample (I) versus the incident intensity (I_0) is dependent on the distance the light travels through the sample (l), the absorption cross-section σ and the difference between the populations of the initial state (N_1) and the final state (N_2) of initial and final electronic energy levels.

UV-Vis experiment is usually performed in either a transmission (typically for liquid samples) or a diffuse-reflectance configuration (for opaque solids). In transmission configuration, the sample is placed in the path of collimated beam of light, which is partially absorbed at characteristic wavelengths that correspond to the electronic transitions of the sample (Figure 2.5). The transmitted light, collected by the spectrometer, is referenced to a baseline measurement, which takes into account the absorbance by a sample holder (*e.g.* cuvette or glass slide). The spectra in transmission configuration are plotted in coordinates absorbance $A = -log(I/I_0)$ versus wavelength λ.

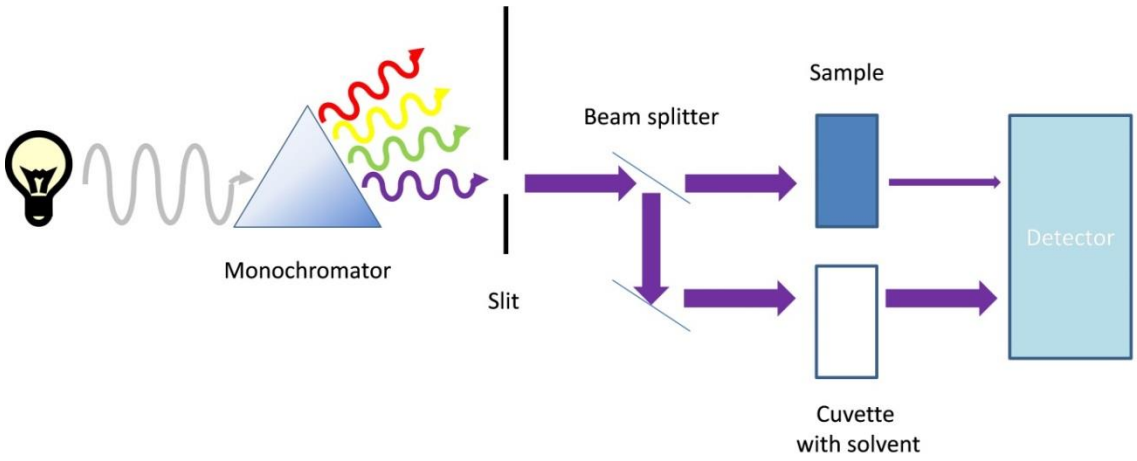

Figure 2.5 Scheme of UV-vis measurement in transmission configuration.

In diffuse reflectance UV-vis spectroscopy (DR UV-vis), the spectrometer measures the diffusely reflected light from the sample. Collection of diffuse reflected light could be performed using mirror optics, fibre optics or an integrating sphere. The latter is more widely used and enables the capture of photons that are reflected in all directions from the sample (Figure 2.6).

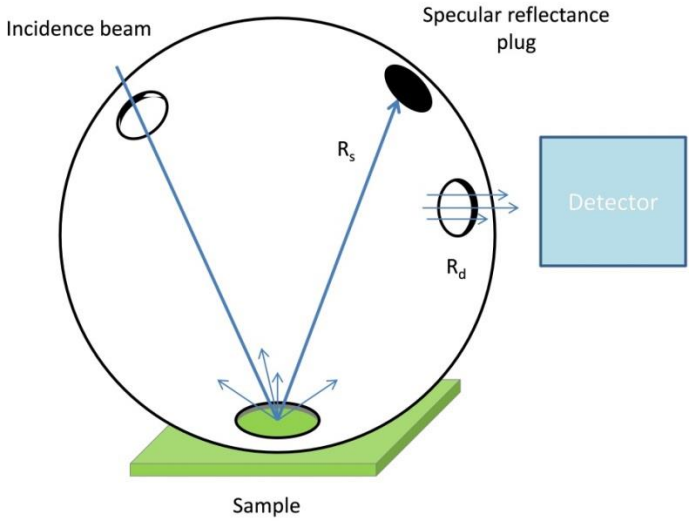

Figure 2.6 Scheme of DR UV-vis configuration using integrating sphere. R_s – specularly reflected light, R_d – diffuse reflected light.

After the incident beam reaches the sample, two types of reflections occur: specular and diffuse. In specular reflectance, the incident beam reflects at an angle equal to the angle of incidence. Because specularly reflected light does not undergo an absorption process it contains little to no information about electronic states of the material and only increases the noise. In diffuse reflection, the incident beam penetrates the sample surface, gets partially absorbed and then reemitted at various non-incident angles. Powders are typically diluted with non-absorbing material, such as $BaSO_4$, which increases diffuse reflectance and minimizes specular reflectance.

In a diffuse-reflectance experiment, the spectrometer measures the amount of light diffuse reflected by the sample with reference to the reflectance by a white material, such as $BaSO_4$ or polytetrafluoroethylene. The value of reflectance measured by the spectrometer is recalculated to obtain Kubelka-Munk function *F(R)*, which can be used to calculate the absorption coefficient α, if the scattering coefficient s is known:

$$F(R) = \frac{(1-R)^2}{2R} = \frac{\alpha}{s}$$

Typically, spectra obtained *via* DR UV-vis measurements are plotted in coordinates *F(R)* versus wavelength λ.

Chapter 3 - Tuning the Selectivity of Supported Gold Catalysts

Work on this Chapter was performed in collaboration with Baira Donoeva, who performed TEM and catalytic studies of some SiO_2-based catalysts. Also, discussions and formulation of ideas and experiments were done together with Baira.

3.1. Introduction

The epoxidation of alkenes is an important industrial process for production of fine chemicals.[140] Epoxidation of cyclohexene, in particular, gives cyclohexene oxide, which is an important monomer widely used in polymerisation industry.[141] Traditionally, epoxidation of alkenes involves the use of stoichiometric oxygen donors,[142] peroxycarboxylic acids[143] or hydrogen peroxide,[144] which either produces environmentally undesirable wastes or, in case of H_2O_2, increases the cost of the process. Utilization of molecular oxygen is highly desirable to make epoxidation "green" and cost-effective. Another important way to reduce the environmental impact of a reaction is to conduct it under solvent-free conditions.[145]

Since the discovery of the exceptional catalytic activity of gold in low-temperature oxidation of CO by Haruta[15] and in hydrochlorination of ethylene by Hutchings,[16] gold catalysts have proven to be efficient in a number of different reactions: cyclizations, rearrangements, selective hydrogenation, C-C coupling reactions, and selective oxidation of alcohols and olefins.[17, 18, 146] Among other reactions, aerobic oxidation of cyclohexene was shown to be catalysed by supported

nanosized gold.[13, 28-30] However, the reaction required the use of tert-butyl hydroperoxide as a radical initiator,[29] and the high yield of cyclohexene oxide was achieved only by conducting the reaction in a specific solvent.[28] Under solvent- and radical initiator-free conditions, mainly products of allylic oxidation are formed.[30]

In this chapter, we have attempted to tune the selectivity of the gold-based catalysts by developing multifunctional catalysts that employ the properties of various supports. We have synthesised gold clusters using wet chemistry methods and deposited them on SiO_2, TiO_2 and WO_3. The effects of the supports on the activity and the selectivity of the catalysts in the aerobic oxidation of cyclohexene under solvent-free conditions, without the addition of radical initiator, were studied. We have investigated the nature of gold species as active sites, the roles that the support and gold species play in the oxidation process and how the selectivity of cyclohexene oxidation can be tuned towards the formation of either cyclohexene oxide or 2-cyclohexen-1-one as major products.

3.2. Experimental procedures

3.2.1. Materials

Gold (99.99%), sodium borohydride (>97%), solution of $HAuCl_4$ (1 mg/mL in 0.5 N HCl), tetraoctylammonium bromide (98%), hydrochloric acid (37%, AR), nitric acid (65%, AR), acetone (AR), chloroform (AR), dichloromethane (99.8%), diethyl ether (AR), DMF (AR), ethanol (AR), methanol (AR), pentane (general grade), petroleum ether (general grade), THF (AR), toluene (AR), n-decane (99%), n-hexane (98%), triphenylphosphine (98%), $AgNO_3$ (99%), chromium nitrate nonahydrate (99%), terephthalic acid (99%), cyclohexene (99%, inhibitor-free), 2-cyclohexen-1-ol (95%), 2-cyclohexen-1-one (98%) and cyclohexene oxide (98%) were purchased from Sigma-Aldrich and Merck. CD_2Cl_2 (13C2, 99%; D6, 98%) was obtained from

Cambridge isotope laboratories. Oxygen (99.7%) was obtained from BOC gases. The supports of titanium (IV) oxide (P25, TiO_2), silicon dioxide (Aerosil OX 50, SiO_2) and tungsten (VI) oxide (nanopowder, <100 nm particle size, WO_3) were purchased from Evonik and Sigma-Aldrich. All materials were used without further purification.

3.2.2. Synthesis of precursors

$Au_{101}(PPh_3)_{21}Cl_5$ (Au_{101}) Triphenylphosphine-stabilized (PPh_3-stabilized) gold nanoparticles with an estimated composition of $Au_{101}(PPh_3)_{21}Cl_5$, with a mean gold core diameter of 1.5 nm were synthesized following the previously described method.[147] Gold (99.99%) coin was dissolved in a freshly prepared mixture of hydrochloric (37%) and nitric acids (65%) (volume ratio 3:1) under continuous stirring at *ca.* 60 ºC. Solvent was removed using a rotary evaporator yielding yellow crystals of $HAuCl_4 \cdot 3H_2O$. Toluene (60 ml) was added to a stirred solution of $HAuCl_4$ (1.00 g, 2.54 mmol) in Milli-Q water (60 mL), followed by the addition of tetraoctylammonium bromide (1.40 g, 2.56 mmol). The organic layer turned red, while the aqueous layer became colourless. After 5 minutes of stirring, PPh_3 (2.30 g, 8.78 mmol) was added to the solution and the organic layer turned cloudy white.

After 10 minutes of vigorous stirring, a freshly prepared solution of $NaBH_4$ (2.00 g, 53 mmol) in Milli-Q water (10 mL) was added drop-wise to the reaction mixture and the solution turned dark-brown. The aqueous and organic layers were separated using a separation funnel and the organic layer was washed 3 times with 100 mL of Milli-Q water. The organic phase was filtered from insoluble impurities and solvent was removed using a rotary evaporator.

The crude dark product was dissolved in chloroform (40 mL) and precipitated with pentane (300 mL). The suspension was filtered through a fritted funnel (porosity

4) to collect the solid (crude nanoparticles). The product was washed with the following solvents to remove the excess of tetraoctylammonium bromide:

- 100 mL of petroleum ether followed by 100 mL of 2:3 MeOH:H_2O
- 100 mL of petroleum ether followed by 100 mL of 1:1 MeOH:H_2O
- 100 mL of petroleum ether

The above sequence of washings was repeated twice. Next, the solid was washed on the same fritted funnel with the following solvents to remove $AuPPh_3Cl$:

- 150 mL of 3:1 pentane:chloroform
- 150 mL of 2:1 pentane:chloroform
- 150 ml of 1:1 pentane:chloroform

During each pentane:chloroform wash the product was agitated and allowed to soak in the wash solution for 5 minutes. The purified product was rinsed through a fritted funnel with CH_2Cl_2 and the solvent was removed on a rotary evaporator. To increase the purity of Au_{101}, after each particle solubilisation step of the procedure described above the solution was filtered through Celite-545 layer on a fritted glass funnel. The final yield of Au_{101} typically was 0.3 g.

$[Au_9(PPh_3)_8](NO_3)_3$ (Au_9) Gold cluster $[Au_9(PPh_3)_8](NO_3)_3$ was prepared using the previously published methodology.[148] In order to prepare Au_9 cluster, first, the precursor $Au(PPh_3)NO_3$ was synthesized using slightly modified procedure described by Mueting *et al*.[149] PPh_3 (2.68 g, 10.2 mmol) was dissolved in EtOH (60 mL) under sonication at 50 ºC. Solution of $HAuCl_4$ (2.00 g, 5.1 mmol) in EtOH (6.5 mL) was slowly poured into the PPh_3 solution and the mixture was left stirring for 10 min. The formed white precipitate ($Au(PPh_3)Cl$) was collected by centrifugation and washed with EtOH (2 × 20 mL) and dried under vacuum at room temperature. $AgNO_3$ (1.44 g, 8.5 mmol) was dissolved in EtOH (51 mL) under sonication at 50 ºC, cooled to room

temperature and poured into the solution of $Au(PPh_3)Cl$ (1.70 g, 3.4 mmol) in CH_2Cl_2 (25 mL). Immediately precipitated AgCl was removed by centrifugation, the solution was collected and dried using a rotary evaporator. The solid was washed with EtOH (3 × 30 mL), dried under vacuum and dissolved in $CHCl_3$ (15 mL). Insoluble impurities were removed by centrifugation and 20 mL of n-hexane was added to the solution. The formed precipitate of $Au(PPh_3)NO_3$ was collected by centrifugation and dried under vacuum. Freshly prepared solution of $NaBH_4$ (18 mg, 0.48 mmol) in EtOH (23 mL) was added drop-wise to the vigorously stirred slurry of $Au(PPh_3)NO_3$ in EtOH (40 mL). After stirring for 2 h, the solution was separated by centrifugation and dried using a rotary evaporator. The resulting solid was dissolved in CH_2Cl_2 (15 mL), insoluble impurities were removed by centrifugation, the solution was collected and dried using a rotary evaporator. The solid was washed with THF and n-hexane and was recrystallized by slow diffusion of diethyl ether into methanol solution of Au_9.

Successful preparation and purity of clusters were confirmed by ^{1}H, ^{31}P NMR, transmission electron microscopy (TEM) and thermogravimetric analysis (TGA) (see below).

The metal-organic framework MIL-101 was synthesized following the previously described method.[150] To a solution of $Cr(NO_3)_3 \cdot 9H_2O$ (2.00 g, 5 mmol) in Milli-Q water (20 mL) terephthalic acid (0.83 g, 5 mmol) was added. The resulting slurry was placed into a Teflon liner of an autoclave, shaken on vortex mixer and briefly sonicated. The mixture was then placed into an autoclave, put into preheated convection oven and thermally treated at 218 ºC for 18 h. After the synthesis the autoclave was allowed to cool to room temperature and the MOF solids were collected by centrifugation, washed with Milli-Q water (20 mL × 2), methanol (20 mL) and DMF (20 mL). The solids were soaked in DMF (50 mL) and kept at 70 ºC overnight.

The resulting MOF was collected by centrifugation and washed with DMF (20 mL), methanol (20 mL × 2), acetone (20 mL × 2) and diethyl ether (20 mL).

3.2.3. Materials characterisation

NMR spectra of gold clusters were recorded using Oxford/Varian AS500 500 MHz NMR spectrometer. The NMR spectra of synthesized clusters closely match the previously published spectra: the ^{31}P spectrum of Au_9 clusters in CD_2Cl_2 has a singlet at δ = 56.9 ppm (Figure 3.1A); the ^{1}H spectrum of Au_{101} in CD_2Cl_2 shows a broad phenyl resonance, centred at 7.1 ppm, with minimal signal (7.52 ppm) due to unbound $Au(PPh_3)Cl$ (Figure 3.1B).

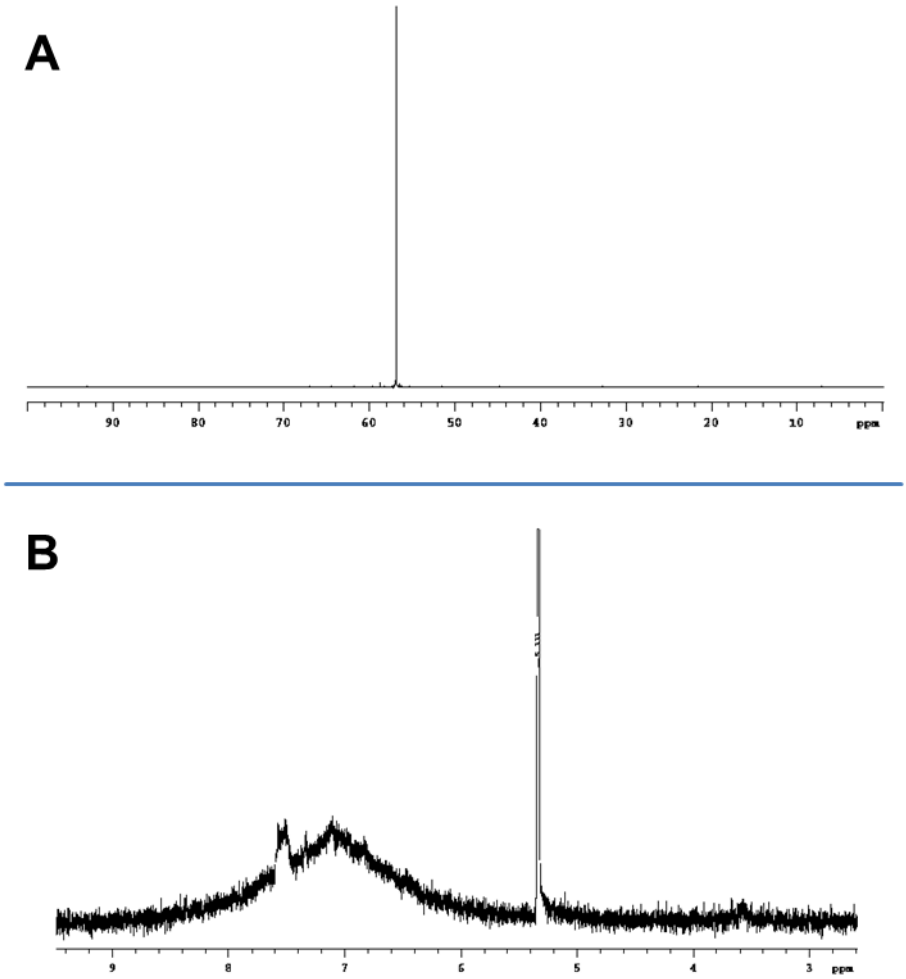

Figure 3.1 NMR spectra of clusters: (A) ^{31}P of Au_9, (B) ^{1}H of Au_{101}.

Thermogravimetric analysis (TGA) was performed using Alphatech SDT Q600 under nitrogen atmosphere. The samples were heated at a rate of 1 ºC/min from room temperature to 230 ºC, and maintained at 230 ºC for 2 h. TGA showed 52% (Au_9) or 26% (Au_{101}) weight loss of the starting mass in comparison to calculated values of 52% and 21%, respectively, based on the loss of triphenylphosphine ligands (Figure 3.2).

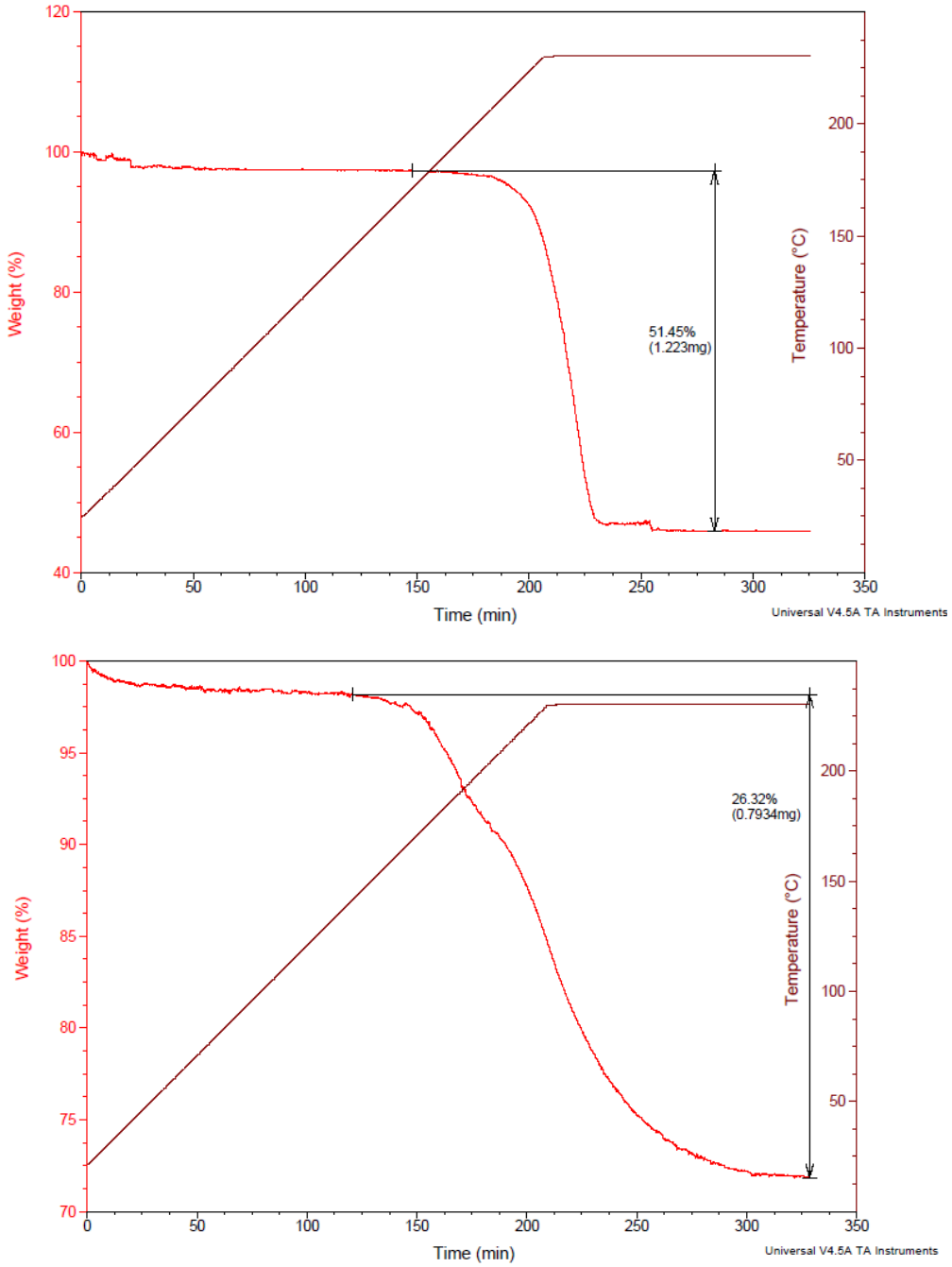

Figure 3.2 TGA of $[Au_9(PPh_3)_8](NO_3)_3$ (left) and $Au_{101}(PPh_3)_{21}Cl_5$ (right).

TEM images were taken on Philips CM200 instrument operating at 200 kV. Samples were deposited on holey carbon coated copper grids (300 mesh) from dichloromethane (clusters) or n-hexane (catalysts). Images were recorded in bright field regime, in which thicker regions or regions with elements of higher atomic number will appear darker in the image due to their stronger scattering of electron beam.[151] Thus, gold nanoparticles and cores of gold clusters will appear as the darkest circles (occasionally other shapes), compared to support materials and background carbon layer of the grid. Typically, at least 100 particles were counted to calculate the average particle diameter. The diameters of gold cores for Au_{101} and Au_9 were 1.5 nm and 0.9 nm respectively, as determined by TEM, which is in accordance with the previously published data (Figure 3.3).

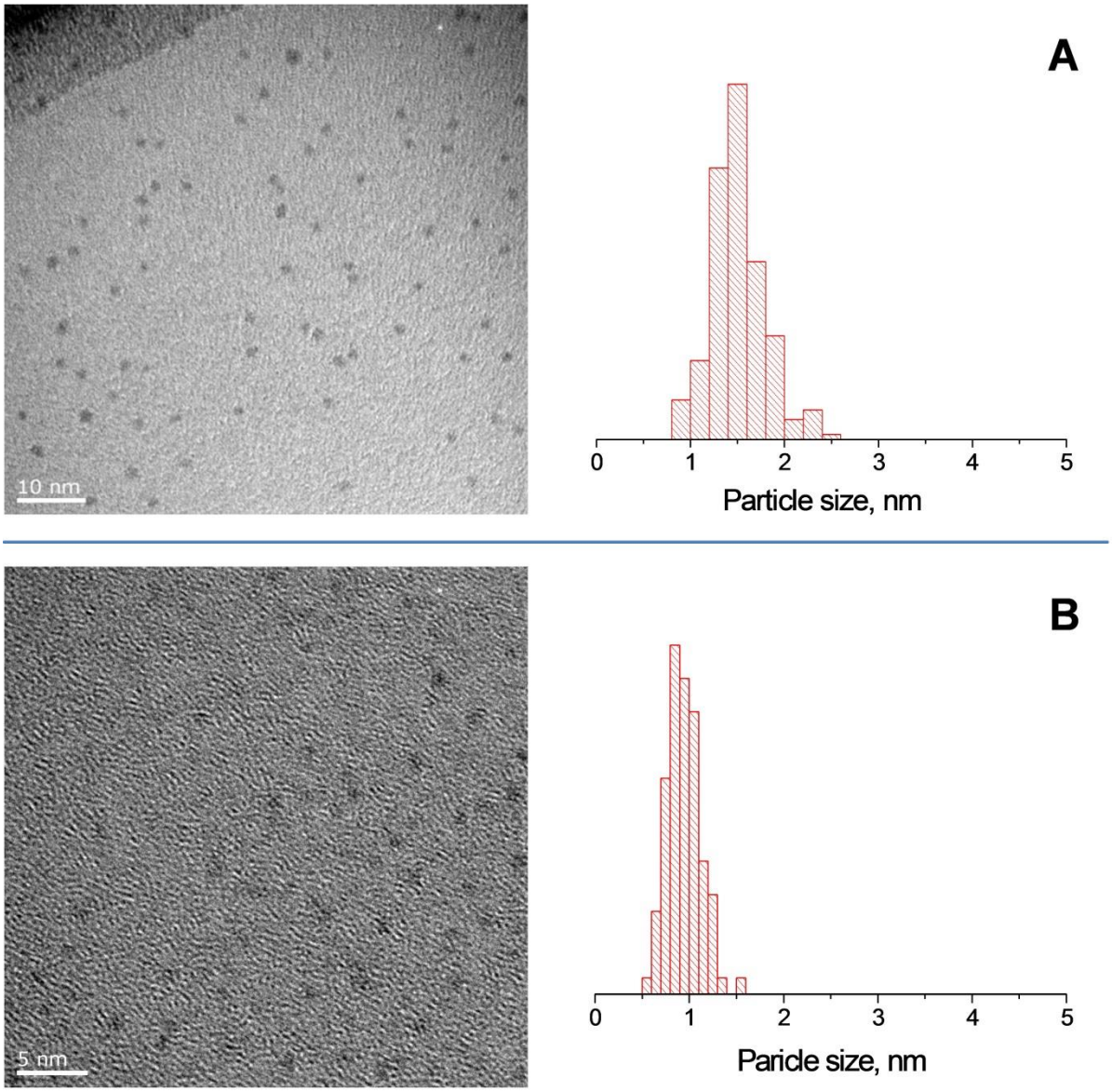

Figure 3.3 Representative TEM images and corresponding size distributions of Au_{101} (A) and Au_9 (B) clusters

MOF structure was confirmed using X-ray powder diffraction (PXRD) performed on Philips PW 1700 automated diffractometer with CoKα radiation and a graphite monochromator by PhD student Campbell McNicoll at Callaghan Innovation (Figure 3.4). The pattern was re-plotted for CuKα radiation source according to the Bragg's law:

$$n\lambda = 2dsin\theta$$

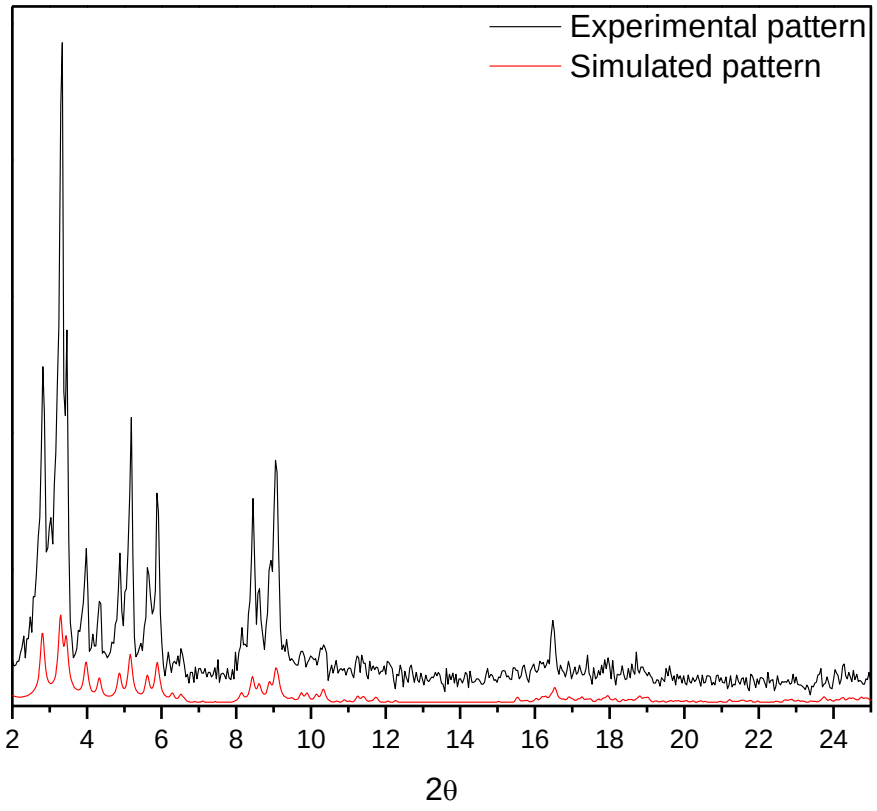

Figure 3.4 Powder X-Ray diffraction pattern of MIL-101: experimental (black) and simulated (red).

The PXRD of the obtained material matches the simulated pattern.

Surface area measurements were performed using Micromeritics ASAP 2010 by PhD student Campbell McNicoll at Callaghan Innovation. The BET surface area of the MIL-101 was found to be 3265 m^2/g, Langmuir Surface area – 4050 m^2/g, which correlates with literature data.[152]

During TGA, the sample of MIL-101 was subjected to heating from 25 to 500 ºC in N_2 at 2 ºC/min. Two weight loss steps were observed (Figure 3.5). The first, occurring at 25 – *ca.* 250 ºC, corresponds to the loss of adsorbed solvent and varies significantly depending on the humidity, the temperature in the laboratory, *etc*. The

second, occurring at 250 ºC – 400 ºC, corresponds to the decomposition of the framework (70% weight loss of dry weight, 68% calculated), which correlates with literature data.[152]

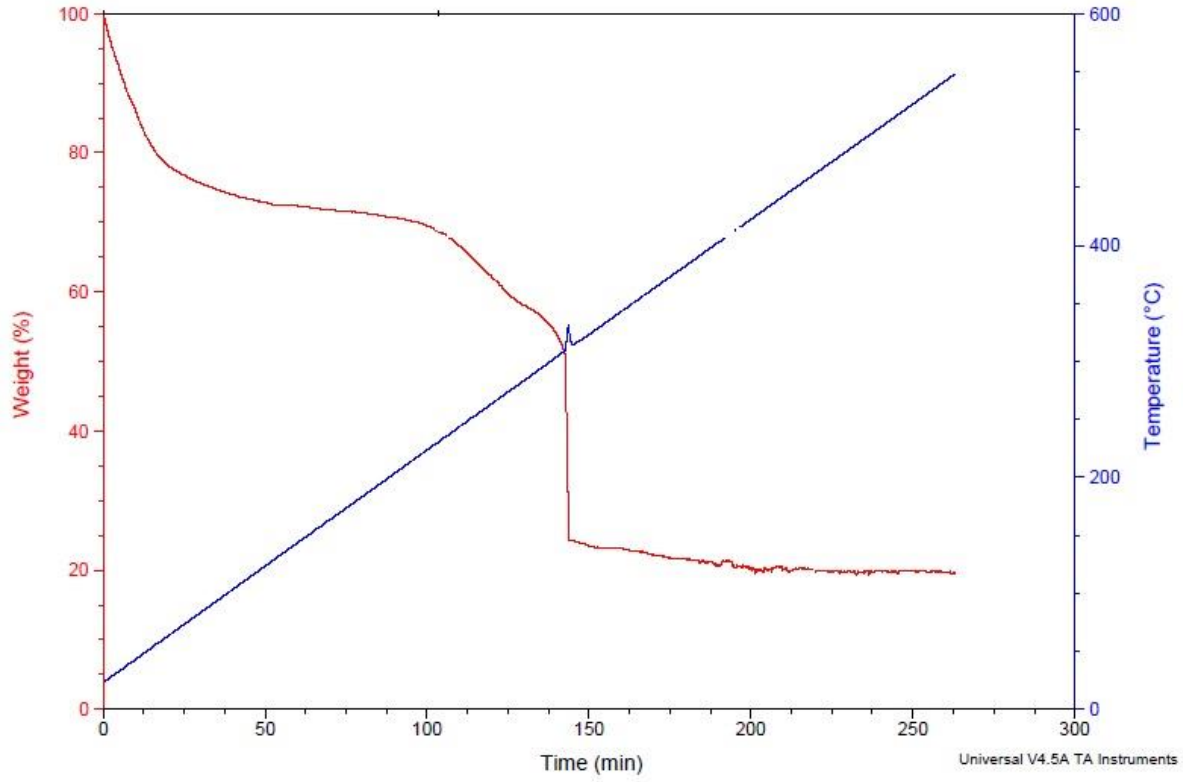

Figure 3.5 TGA curve of MIL-101.

The formation of uniformly sized, octahedral crystals of MIL-101 can be observed by scanning electron microscopy (SEM) (Figure 3.6). The latter was performed using JEOL JSM 7000F operating at 15 kV accelerating voltage.

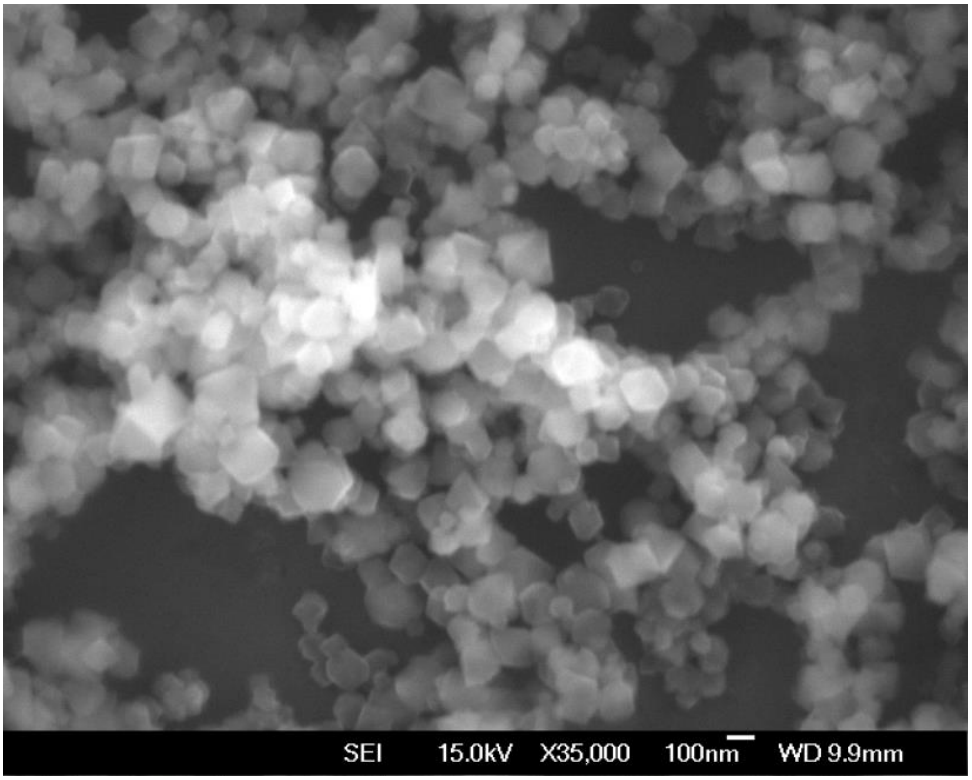

Figure 3.6 SEM image of MIL-101.

Diffuse reflectance UV-vis (DR UV-vis) spectra of catalysts were recorded on a GBC Cintra 404 spectrophotometer (discussed later).

3.2.4. Catalyst preparation and characterisation

Typically, a calculated amount of gold cluster dissolved in CH_2Cl_2 (10 mL, 1-2 mg/mL) was added drop-wise to a vigorously stirred slurry of SiO_2, TiO_2 or WO_3 (500 mg) in CH_2Cl_2 (15 mL). The mixture was stirred for 30 min and the solid was collected by centrifugation. A colourless supernatant solution confirmed complete cluster deposition. The catalysts were washed with CH_2Cl_2 (20 mL) and dried under vacuum at room temperature.

The gold content of the catalysts was determined quantitatively by atomic absorption spectroscopy (AAS) using a Varian SpectrAA 220FS instrument. A calibration curve was obtained *via* the analysis of calibration solutions, which were

prepared by dilution of commercially available standard solution of $HAuCl_4$ (1 mg/mL in 0.5 N HCl). Catalyst samples (typically 25-30 mg) were treated with a freshly prepared mixture of hydrochloric (37%) and nitric acids (65%) (volume ratio 3:1, total volume 10 mL) at 80 ºC overnight. The resulting mixture of dissolved gold and solid support was separated by centrifugation, solids were washed with 5% solution of *aqua regia* in water and both the liquid obtained after the removal of solid catalyst and the washings were collected. The volume of combined liquid was reduced to *ca.* 2 – 3 mL under heating at 115 ºC. The resultant liquid was transferred to either a 10 mL or 25 mL volumetric flask (depending on the expected gold loading) and topped up with 5% solution of *aqua regia*. The calibration coefficient obtained from the linearization of calibration curve was used to calculate gold loadings from the absorption values (Note 1).

Note 1. Derivation of the formula for the calculation of the gold loading.

If the weight of the sample treated with aqua regia is m_{sample}, and gold loading of the sample is ω (%) then the weight of gold that went to solution m_{gold} is

$$m_{gold} = \frac{m_{sample} \cdot \omega}{100\%}$$

The concentration of gold in the solution analysed by AAS C_{gold} can then be expressed as

$$C_{gold} = \frac{m_{gold}}{V_{flask}} = \frac{m_{sample} \cdot \omega}{V_{flask} \cdot 100\%},$$

where V_{flask} is the volume of the volumetric flask used to prepare the solution (see above). Using the linearization of calibration curve $a_{gold} = k \cdot C_{gold}$, where a_{gold} is the value of absorption obtained from AAS, k – calibration coefficient and C_{gold} - concentration of gold in the solution, the formula for gold loading could be obtained:

$$\omega = \frac{a_{gold} \cdot V_{flask} \cdot 100\%}{k \cdot m_{sample}}$$

The establishment of the concentration of leached gold species in a reaction mixture was performed using inductively coupled plasma mass spectrometry (ICP-MS). An aliquot of the reaction mixture, separated from the solid catalyst by filtration,

was placed into a ceramic boat and calcined in a tube furnace in air at 650 ºC. The boat was then treated with *aqua regia*, the liquid and washings were collected, transferred to a volumetric flask and diluted with Milli-Q water. The resulting solution was analysed using ICP-MS.

3.2.5. Catalyst testing

Cyclohexene oxidation was performed in a 25 mL glass reactor equipped with a reflux condenser. Except where specified below, the system was flushed with oxygen three times and remained connected to an O_2-filled rubber balloon throughout the reaction. Typically, a mixture of cyclohexene (5 mL), catalyst (50 mg) and n-decane (0.2 M, as an internal standard) was magnetically stirred (500 rpm) at 65 °C. After 16 hours, the reactor was cooled down to room temperature, the condenser was rinsed with acetone (5 mL) and the reaction mixture was separated from the solid catalyst by centrifugation. The catalyst was washed with acetone and dried under vacuum before recycling.

The liquid samples were analysed by gas chromatography (GC) using a Shimadzu GC-2010 equipped with an Rxi-5SilMS capillary column (30 m × 0.25 mm × 0.25 μm) and a flame ionization detector (FID). Products were identified by gas chromatography mass-spectrometry (GC-MS) using a Shimadzu GCMS-QP2010. Typical chromatogram is shown in Figure 3.7.

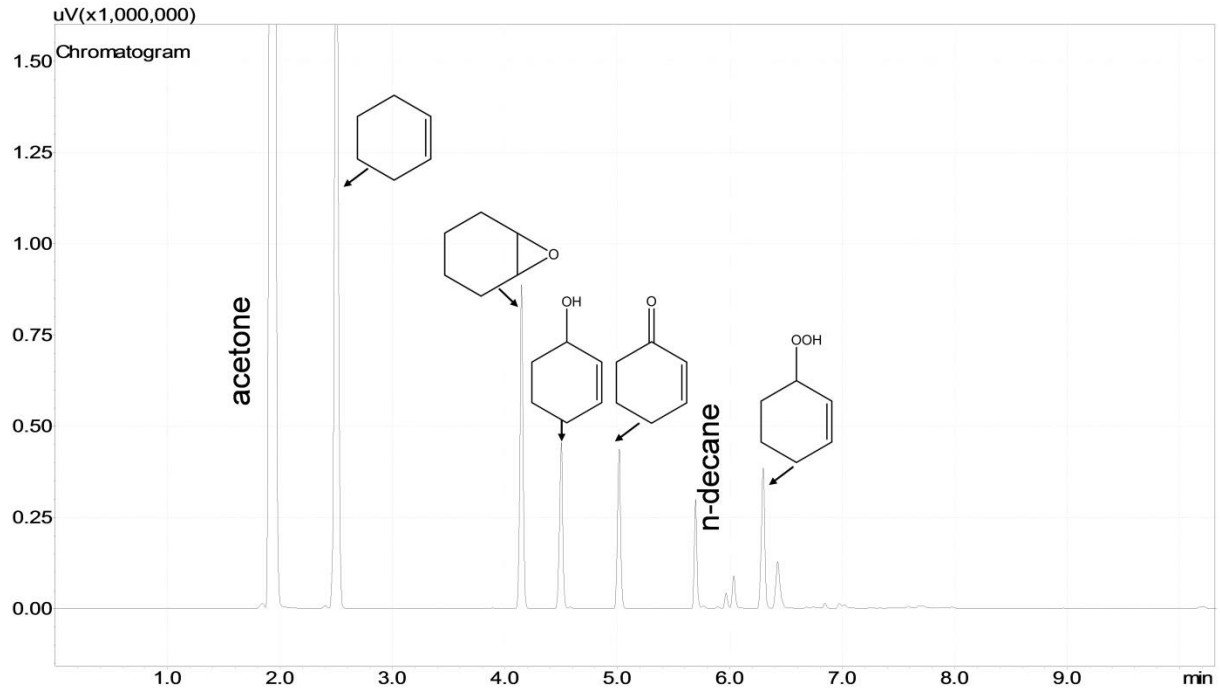

Figure 3.7 Chromatogram of reaction mixture obtained after cyclohexene oxidation, catalysed by Au/WO_3.

Quantitative analysis of reaction mixtures was performed by GC-FID using calibration solutions prepared from commercially available products. Solutions of 2-cyclohexen-1-ol, 2-cyclohexen-1-one and cyclohexene oxide of various concentrations, together with 0.2 M n-decane as internal standard, were prepared. Calibration curves were plotted in coordinates $S_{product}/S_{decane} - n_{product}/n_{decane}$, where $n_{product}/n_{decane}$ – is the molar ratio of product/n-decane in the calibration solution, $S_{product}$ – peak area of the corresponding product calculated from chromatogram, and S_{decane} – peak area of n-decane. Calibration coefficients were extracted from linear approximations of calibration curves (Figure 3.8).

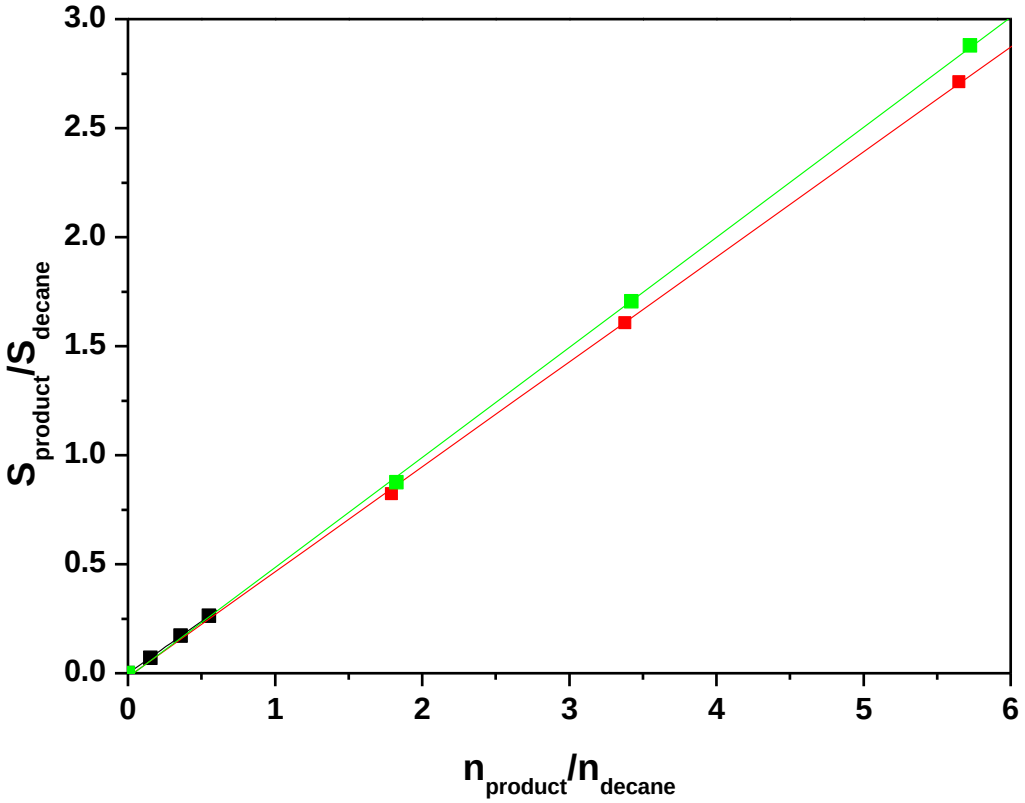

Figure 3.8 Calibration curves for cyclohexene oxide (green), 2-cyclohexen-1-one (red) and 2-cyclohexene-1-ol (black).

Calibration coefficients were used to determine the yield of the products from the ratio of the peak areas of product/n-decane, calculated from the chromatogram of the reaction mixture (Note 2).

Note 2. Derivation of the formula for the calculation of the product yield.

If the volume of cyclohexene solution, containing 0.2 M n-decane is V_{sol}, then the volume of n-decane in this solution is:

$$V_{dec} = \frac{V_{sol} \cdot C_{dec} \cdot M_{dec}}{\rho_{dec}},$$

where C_{dec} is the concentration of n-decane (M), M_{dec} – molar mass of n-decane and ρ_{dec} – density of n-decane.

The volume of cyclohexene can then be expressed as:

$$V_{CyH} = V_{sol} - V_{dec} = V_{sol} - \frac{V_{sol\cdot} \cdot C_{dec} \cdot M_{dec}}{\rho_{dec}} = V_{sol}(1 - \frac{C_{dec} \cdot M_{dec}}{\rho_{dec}})$$

the amount of cyclohexene:

$$n_{CyH} = \frac{V_{CyH} \cdot \rho_{CyH}}{M_{CyH}} = V_{sol}(1 - \frac{C_{dec} \cdot M_{dec}}{\rho_{dec}}) \cdot \rho_{CyH}/M_{CyH}$$

where M_{CyH} – molar mass of cyclohexene and ρ_{CyH} – density of cyclohexene. Given that the V_{sol} can be expressed as $V_{sol} = \frac{n_{dec}}{C_{dec}}$, the yield of the product is

$$Y_{product} = 100\% \cdot \frac{n_{product}}{n_{CyH}} = 100\% \cdot \frac{n_{product}}{n_{dec}} \cdot \frac{M_{CyH} \cdot C_{dec}}{\rho_{CyH\cdot}(1 - \frac{C_{dec} \cdot M_{dec}}{\rho_{dec}})}$$

and using the linearization of the calibration curve $\frac{S_{product}}{S_{dec}} = k \cdot \frac{n_{product}}{n_{dec}}$, where k is the calibration coefficient, $S_{product}$ – peak area of the corresponding product calculated from chromatogram, and S_{decane} – peak area of n-decane we can obtain the formula for the calculation of product yield from the areas of the peaks of product and n-decane obtained from chromatograms:

$$Y_{product} = 100 \cdot \frac{S_{product}}{S_{dec}} \cdot \frac{1}{k} \cdot \frac{M_{CyH} \cdot C_{dec}}{\rho_{CyH\cdot}(1 - \frac{C_{dec} \cdot M_{dec}}{\rho_{dec}})}$$

Some hydroperoxides, *e.g.* cyclohexane hydroperoxide, are known to decompose during GC analysis[153] to produce mainly the corresponding alcohols and ketones thus tampering their true concentrations.

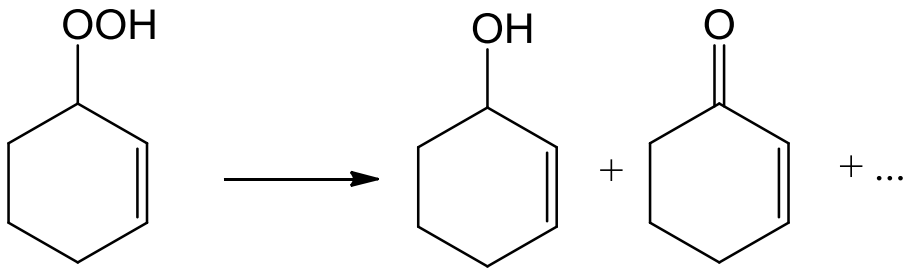

In order to establish correct concentrations analysed mixture is treated with PPh_3, which quantitatively converts hydroperoxide to the corresponding alcohol.[153]

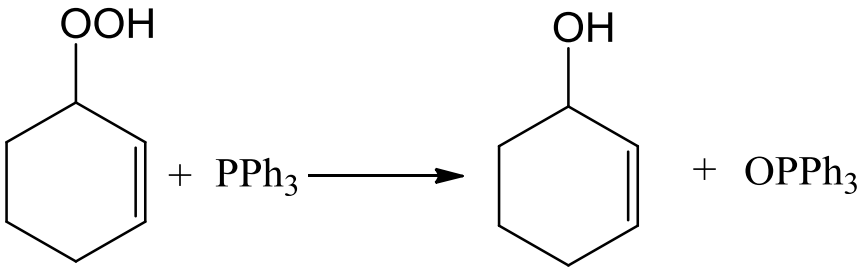

Estimation of true concentrations of alcohol and ketone is made from the comparison of the chromatograms of the mixture treated with PPh_3 and untreated one.[153] In our case, pre-treatment of the reaction mixture with PPh_3 did not change the concentration of 2-cyclohexen-1-one compared to an untreated mixture, indicating that cyclohexenyl hydroperoxide was not decomposing during GC analysis.

The concentration of cyclohexenyl hydroperoxide was determined using iodometric titration in 80% acetic acid.[154] Reverse titration was performed as follows: in a conical flask *ca.* 30 mg of KI and 1 mL of 80 % acetic acid were added to 200 µL of reaction solution. The mixture was left for 5 minutes to allow the formation of I_2 according to the following equation:

$$2I^- + CyOOH + 2H^+ = I_2 + CyOH + H_2O$$

The formed I_2 was then titrated with $Na_2S_2O_3$ (0.05 M, established by titration).

$$2S_2O_3^{2-} + I_2 = S_4O_6^{2-} + 2I^-$$

Before titration of I_2 the concentration of $Na_2S_2O_3$ solution was standardized using 0.1 M $K_2Cr_2O_7$ solution according to the following equations:

$$Cr_2O_7^{2-} + 6I^- + 14H^+ = 3I_2 + 2Cr^{3+} + 7H_2O$$

$$2S_2O_3^{2-} + I_2 = S_4O_6^{2-} + 2I^-$$

Because cyclohexenyl hydroperoxide did not decompose during the GC analysis we were able to obtain calibration coefficients for cyclohexenyl hydroperoxide on the basis of comparison of GC data and iodometric titration results.

Each catalytic experiment was reproduced at least three times. The typical standard errors of independent catalytic tests were <1.5%.

3.3. Results and discussion

3.3.1. Catalyst preparation and characterisation

As-made gold clusters were deposited onto the oxide supports from CH_2Cl_2 solution. We have chosen non-porous nanopowders of TiO_2, SiO_2 and WO_3 as supports with similar morphologies – particle sizes below 100 nm and surface areas ≤ 50 m^2g^{-1}. Two series of catalysts with target gold loadings ranging from 0.1 wt% to 0.5 wt% were prepared. It was found that clusters readily adhere to SiO_2 and TiO_2 from CH_2Cl_2 solution at all target loadings.

In the case of WO_3, for target loadings greater than 0.1 wt%, n-hexane (50 mL) was slowly added to the slurry to ensure deposition of Au_9, and maximum actual loadings of only *ca.* 0.3 wt% could be achieved. Deposition of Au_{101} on WO_3 was readily achieved without the use of n-hexane for all target loadings.

The actual gold loadings, established using AAS, are shown in Table 1, where the two-digit prefixes in the sample designations are indicative of the approximate loadings in wt%.

After deposition, the mean diameter of Au_{101} clusters, as determined by TEM, slightly increases (Table 3.1). We were unable to detect as-deposited Au_9 clusters using bright-field TEM, which indicates that the size of metal core remains below 1 nm. However, during the course of catalytic cyclohexene oxidation both types of clusters sinter to form particles with mean diameters ranging from *ca.* 4 to 10 nm (Table 3.1 and Figure 3.9). The mean diameter of the nanoparticles formed from Au_{101} during catalytic cycle is decreasing with lower gold loading. In contrast, Au_9 clusters form bigger nanoparticles at lower loading. This could suggest different sintering

mechanisms for two clusters – Au_9 acts as feedstock for nanoparticle growth, while Au_{101} clusters collide and agglomerate through surface diffusion. We suggest that agglomeration of Au_9 clusters occurs similarly to the process of crystals formation in which lower concentration of precursor leads to the creation of smaller amount of nucleation sites and thus to bigger crystals. Thus, at high gold loadings the majority of Au_9 clusters rapidly sinter into stable nanoparticles with mean diameters of 4-6 nm; while at lower surface concentrations clusters initially form fewer nanoparticles that act as nucleation sites that keep growing, consuming the remaining Au_9 clusters to eventually form 8-10 nm particles. As agglomeration of Au_{101} proceeds *via* cluster collision, the degree of sintering should decrease with the lower surface concentration of clusters.

Table 3.1 Catalysts properties

Catalyst	Gold loading, AAS (wt%)	Nanoparticle diameter, TEM (nm)	
		mean ± s.e.[f]	s.d.[e]
$0.5Au_{101}/WO_3$	0.52	2.2±0.1	0.7
$0.5Au_{101}/WO_3$[a]	0.47	5.1±0.3	2.1
$0.5Au_{101}/WO_3$[b]	0.47	5.4±0.2	1.8
$0.1Au_{101}/WO_3$	0.097	2.3±0.1	0.5
$0.1Au_{101}/WO_3$[a]	0.070	4.4±0.2	1.6
$0.3Au_9/WO_3$	0.31	<1[d]	-
$0.3Au_9/WO_3$[a]	0.28	5.1±0.1	1.5
$0.3Au_9/WO_3$[b]	0.28	5.8±0.2	2.1
$0.3Au_9/WO_3$[c]	0.28	6.1±0.2	2.0
$0.1Au_9/WO_3$	0.093	<1[d]	-
$0.1Au_9/WO_3$[a]	0.087	7.9±0.3	2.2
$0.5Au_{101}/SiO_2$	0.44	2.0±0.1	0.6
$0.5Au_{101}/SiO_2$[a]	0.29	5.1±0.2	2.0
$0.1Au_{101}/SiO_2$	0.12	1.6±0.1	0.4
$0.1Au_{101}/SiO_2$[a]	0.068	4.9±0.1	1.5
$0.3Au_9/SiO_2$	0.27	<1[d]	-
$0.3Au_9/SiO_2$[a]	0.20	6.3±0.2	1.6
$0.3Au_9/SiO_2$[b]	0.20	6.8±0.2	2.3
$0.1Au_9/SiO_2$	0.098	<1[d]	-
$0.1Au_9/SiO_2$[a]	0.073	9.6±0.6	3.9

[a] Recovered after the 1st catalytic cycle. [b] Recovered after the 2nd catalytic cycle. [c] Recovered after the 3rd catalytic cycle. [d] No gold particles were detected using bright-field TEM. [e] s.e. – standard error of the mean, s.d. – standard deviation of the distribution.

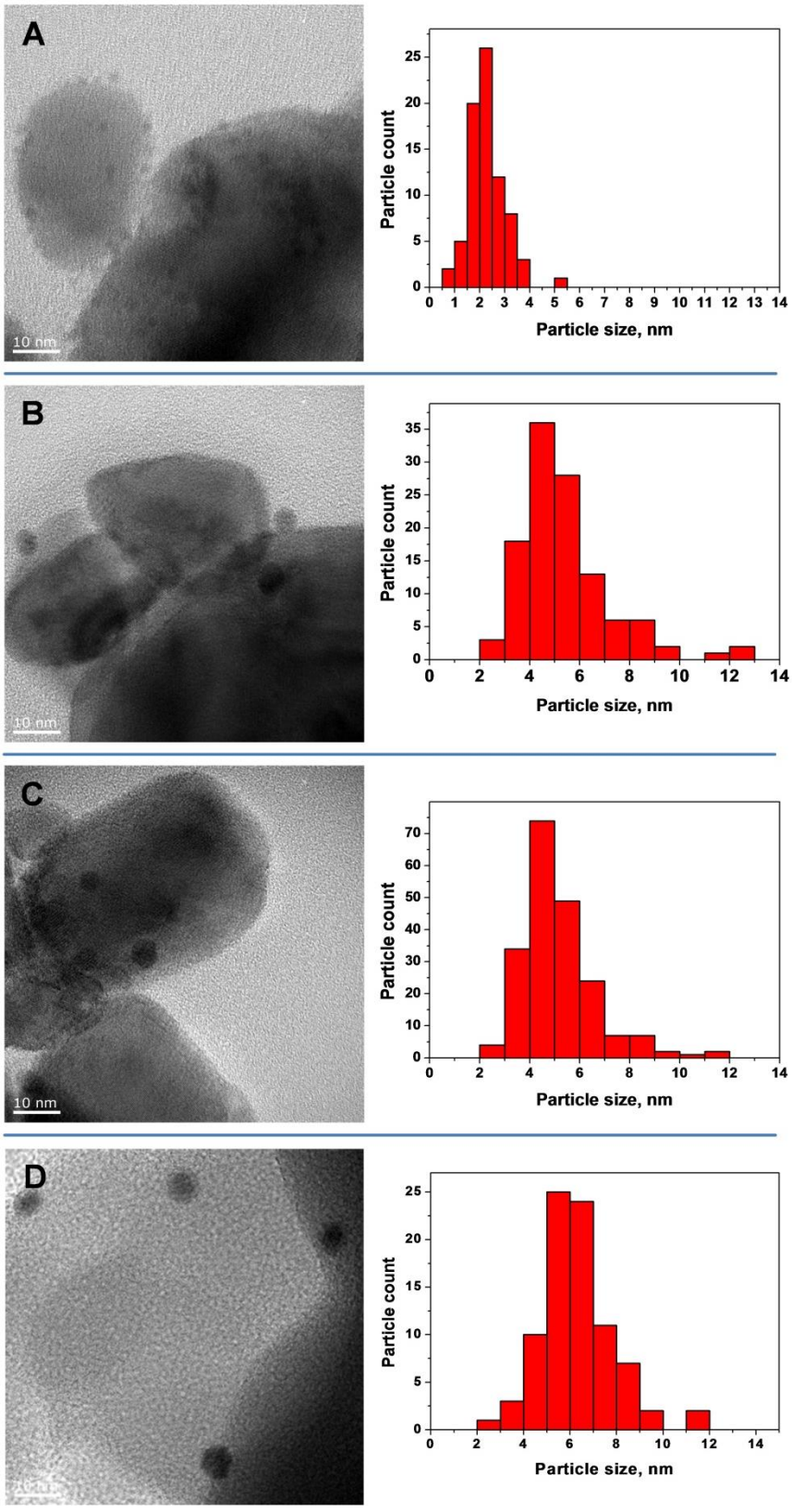

Figure 3.9 Representative TEM images and particle size distributions of the catalysts. (A) $0.5Au_{101}/WO_3$ as deposited. Catalysts recovered after 1st catalytic cycle: (B) $0.5Au_{101}/WO_3$ (C) $0.3Au_9/WO_3$ (D) $0.3Au_9/SiO_2$.

3.3.2. Aerobic oxidation of cyclohexene under solvent-free conditions

Table 3.2 summarizes the catalytic activity of Au_9 and Au_{101} deposited on TiO_2, SiO_2 and WO_3 at various gold loadings in the aerobic oxidation of cyclohexene, which was conducted under solvent-free conditions without the addition of radical initiator and using molecular oxygen as the only oxidant.

Table 3.2 Performance of catalysts in cyclohexene oxidation[a]

Catalyst	Conversion, %	Selectivity, %			
		Cy-oxide 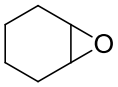	Cy-ol 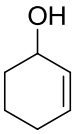	Cy-one 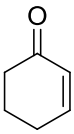	CyOOH 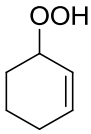
Blank	2	-	-	-	-
TiO_2	2	-	-	-	-
SiO_2	2	-	-	-	-
WO_3	9	33	30	4	32
$0.5Au_9/TiO_2$	2	-	-	-	-
$0.5Au_{101}/TiO_2$	2	-	-	-	-
$0.5Au_{101}/WO_3$	50	26	18	17	19
$0.1Au_{101}/WO_3$	36	35	23	12	18
$0.3Au_9/WO_3$	50	27	20	16	17
$0.1Au_9/WO_3$	33	34	24	11	21
$0.5Au_{101}/SiO_2$	48	6	15	24	38
$0.1Au_{101}/SiO_2$	39	7	11	17	54
$0.3Au_9/SiO_2$	43	7	12	19	51
$0.1Au_9/SiO_2$	25	5	7	12	68

[a] Reaction conditions: cyclohexene (5 mL), n-decane (0.2 M) as internal standard, catalyst (0.05 g), O_2 (~1 atm), 65 °C, 16 h, glass reactor.

Cyclohexene conversion and product distribution depend strongly on the nature of the support. TiO_2-based catalysts are inactive, showing conversions comparable to that of the reaction in the absence of catalyst (blank). Clusters deposited on SiO_2 show high conversions of cyclohexene, with cyclohexenyl hydroperoxide (CyOOH) being the main product. Other products were 2-cyclohexen-1-one (Cy-one), 2-cyclohexen-1-ol (Cy-ol) and cyclohexene oxide (Cy-oxide). WO_3-supported clusters have comparable activity, but the main product is cyclohexene oxide.

Unsupported gold nanoparticles previously have been shown to have high catalytic activity in some liquid-phase reactions;[155] thus, it is important to investigate whether observed catalytic activity should be attributed to supported or leached gold species. As seen from the AAS studies (Table 3.1), gold does leach into solution from as-prepared samples during the first catalytic cycle.

However, no such leaching was detected during subsequent recyclability tests. We suggest that as clusters agglomerate into bigger particles leaching of gold species stops. This suggestion correlates with the fact that the degree of leaching during the first cycle decreases with higher loading. A higher surface density of gold clusters accelerates agglomeration and hence fewer non-sintered clusters have time to leach into solution. Because the catalyst retains *ca.* 90% of its catalytic activity during catalytic cycles 2-5 (Figure 3.10), while leaching becomes undetectable on these stages, we conclude that the activity could be attributed to the supported, agglomerated particles and that gold species leached during the first cycle are essentially catalytically inactive.

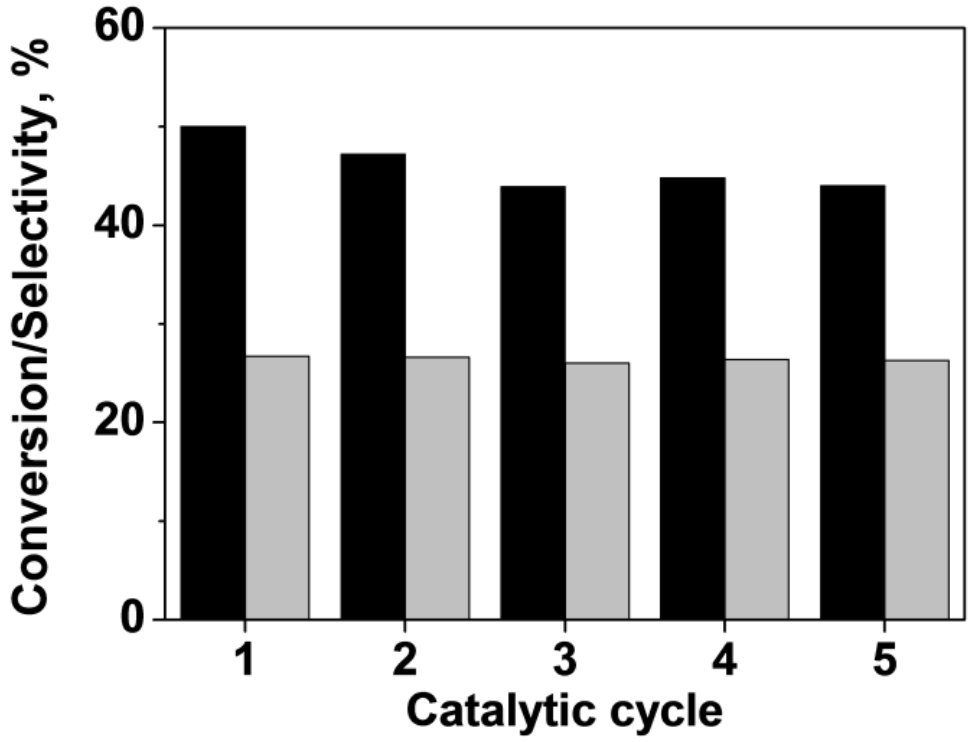

Figure 3.10 Recyclability of $0.3Au_9/WO_3$. Conversion of cyclohexene (black) and selectivity towards cyclohexene oxide (grey).

The methodology of hot filtering is typically used to determine whether the catalyst is homogeneous or heterogeneous.[156] In our case, the cyclohexene oxidation did not slow down upon the removal of Au/WO_3 using a 0.2 μm filter after 6 h of reaction, which, according to the method, should indicate the homogeneous nature of the catalysis. However, it is known that cyclohexenyl hydroperoxide can catalyse the autoxidation of cyclohexene.[157] Therefore, the hot filtering test is not suitable for distinguishing between heterogeneous and homogeneous catalysis for cyclohexene oxidation when cyclohexenyl hydroperoxide is formed in a sufficient amount, because the formed hydroperoxide would autocatalyse the reaction after the catalyst is removed.

In order to demonstrate that leached gold species are inactive in cyclohexene oxidation, we have performed a pair of tests in reaction-like conditions under which

gold leaching would occur but cyclohexenyl hydroperoxide formation would be suppressed. In the first test, an initial reaction was performed at 65 ºC for 6 h using as-made catalyst, but the reactor was filled with argon instead of oxygen. The solid catalyst was then removed by hot filtration and the liquid reaction mixture was subjected to typical reaction conditions (65 ºC or 16 h) with the reactor now filled with *ca.* 1 atm oxygen. The existence of gold leachate in the reaction mixture was confirmed using ICP-MS (concentration of Au in reaction mixture was *ca.* 1 ppm), but no detectable cyclohexene conversion was observed (Figure 3.11).

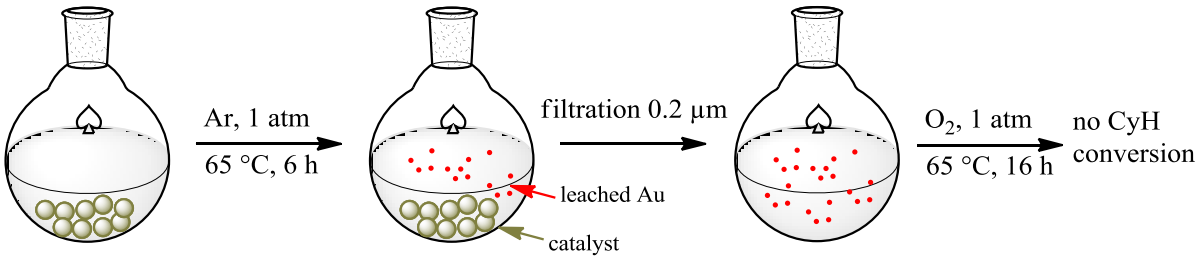

Figure 3.11 Filtration test in which hydroperoxide formation was supressed by argon atmosphere.

In the second test, cyclohexenyl hydroperoxide formation was suppressed by addition of n-hexane. First, the cyclohexene oxidation was conducted under oxygen atmosphere (*ca.* 1 atm) using the mixture of cyclohexene (50 µL) and n-hexane (2 mL). After 6 h, the liquid phase was separated by hot filtering and added to 5 mL of cyclohexene. When subjected to typical reaction conditions, the mixture showed no cyclohexene conversion after 16 h. In contrast, solid catalyst, isolated on the previous step, catalysed the oxidation of cyclohexene in the mixture of n-hexane (2 mL) and cyclohexene (5 mL), giving 11% conversion (Figure 3.12).

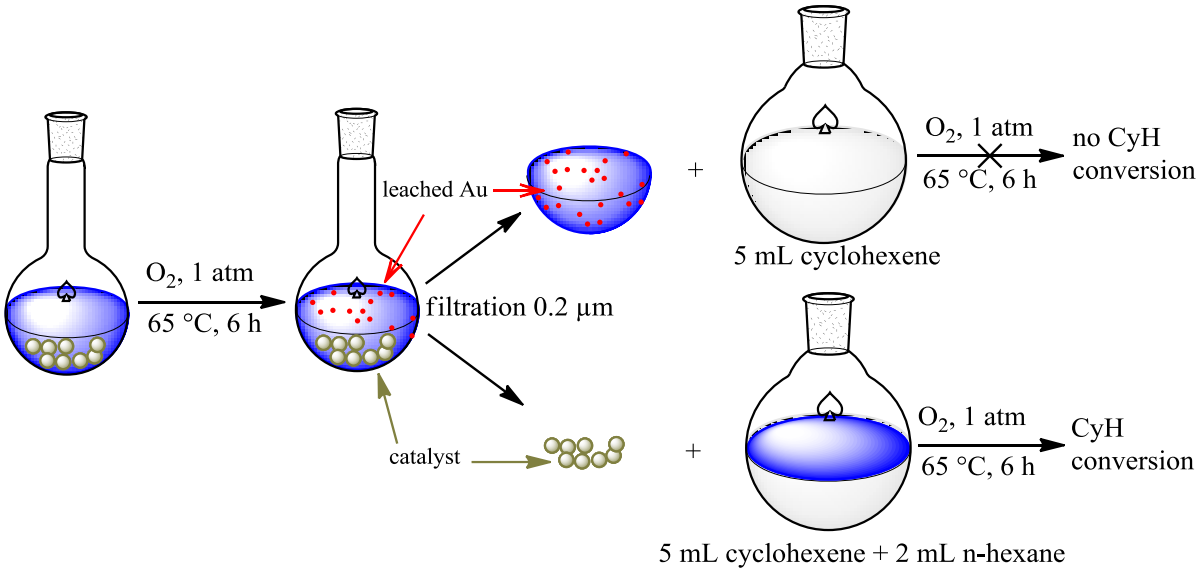

Figure 3.12 Filtration test in which hydroperoxide formation was supressed by the addition of n-hexane.

3.3.3. Investigation of catalyst bifunctionality

The similarity of morphology and size of the gold nanoparticles formed on SiO_2 and WO_3 supports during the catalytic reaction is indicated by both TEM (see Table 3.1 and Figure 3.9) and DR UV-vis spectroscopy. In the latter, the bands attributed to the localized surface plasmon resonance have similar shapes and positions for both types of catalysts (Figure 3.13).[113, 158, 159]

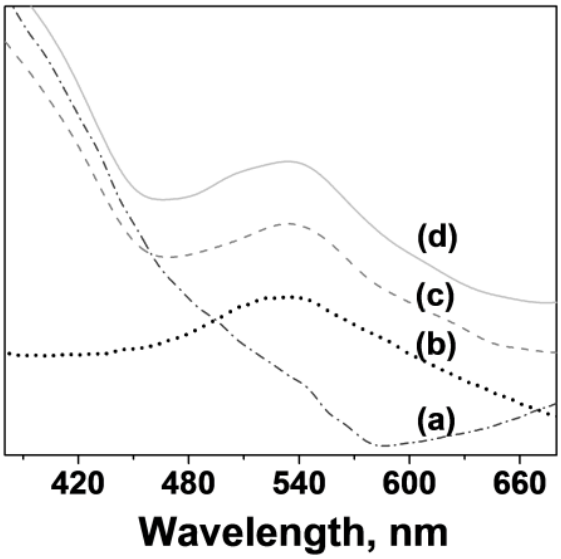

Figure 3.13 DR UV-Vis spectra of the catalysts. (a) $0.3Au_9/WO_3$ as deposited. Catalysts recovered after 1st catalytic cycle: (b) $0.3Au_9/SiO_2$, (c) $0.3Au_9/WO_3$ and (d) $0.5Au_{101}/WO_3$.

Interestingly, SiO_2- and WO_3-based catalysts with similar gold loadings also have comparable turnover frequencies (TOFs) calculated from the initial reaction rates (Figure 3.14, see Chapter 4 for experimental details). Additionally, the product evolution profiles for both types of catalysts have similar cyclohexenyl hydroperoxide accumulation stages.

Note 3. Calculation of TOF

TOFs in this chapter were calculated according to the following equation:

$$TOF, h^{-1} = \frac{n^0_{substrate} - n_{substrate}}{time(h) \cdot n_{Au}},$$

where $n^0_{substrate}$ is initial number of moles of the substrate, $n_{substrate}$ is a number of moles left in the reaction after time (h) and n_{Au} is the number of moles of Au introduced to a catalytic reaction.

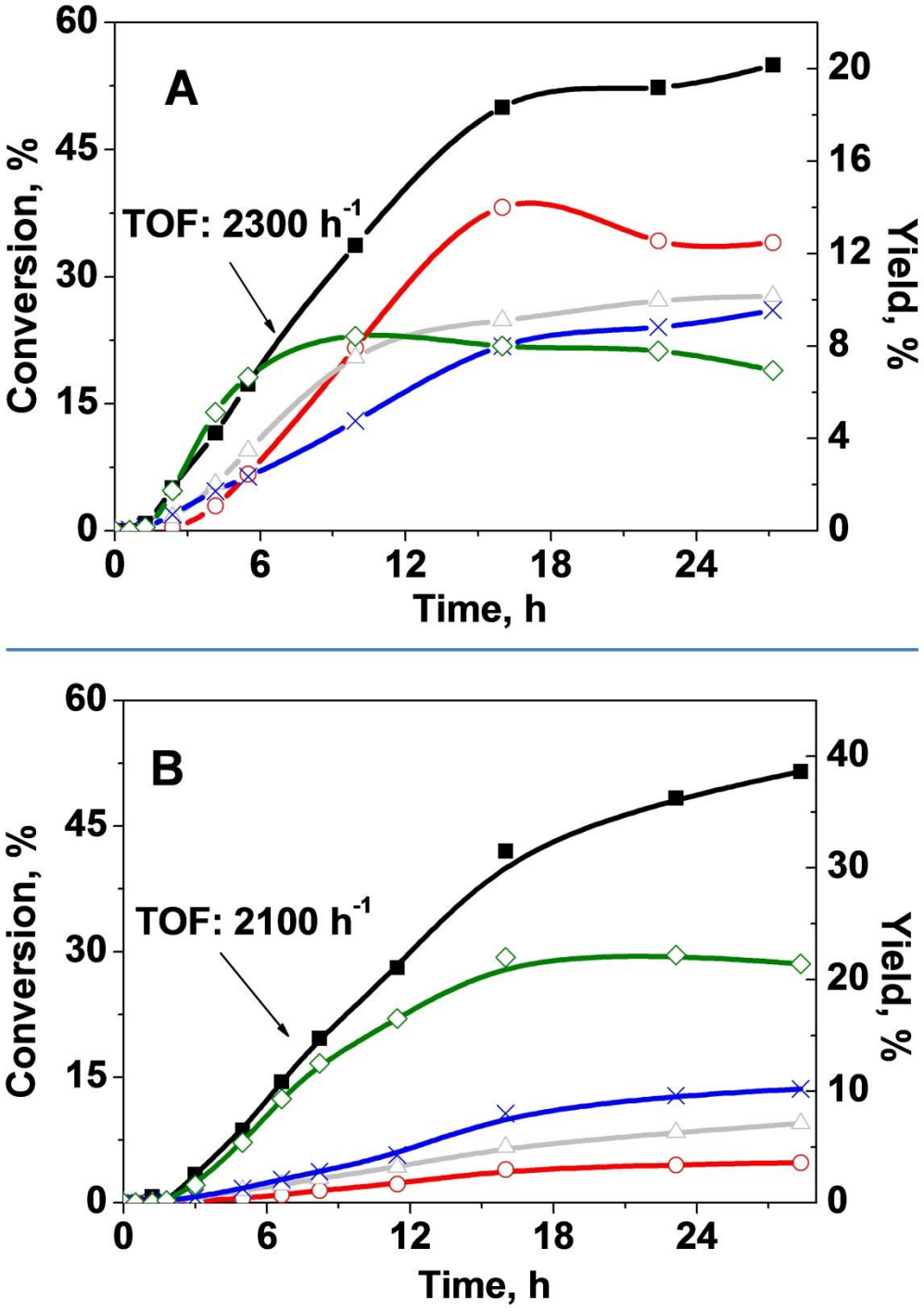

Figure 3.14 Reaction profile of cyclohexene oxidation catalysed by $0.3Au_9/WO_3$ (A) and $0.3Au_9/SiO_2$ (B). Cyclohexene conversion (■, black); left ordinate. Yield of cyclohexene hydroperoxide (◊, olive), cyclohexene oxide (○, red), 2-cylohexen-1-one (×, blue), 2-cyclohexen-1-ol (Δ, light-grey); right ordinate.

Based on these data, we suggest that gold particles catalyse cyclohexene conversion to cyclohexenyl hydroperoxide (reaction I, Figure 3.15), while WO_3 catalyses reaction of cyclohexenyl hydroperoxide with cyclohexene, producing cyclohexene oxide and 2-cyclohexen-1-ol (reaction II, Figure 3.15).

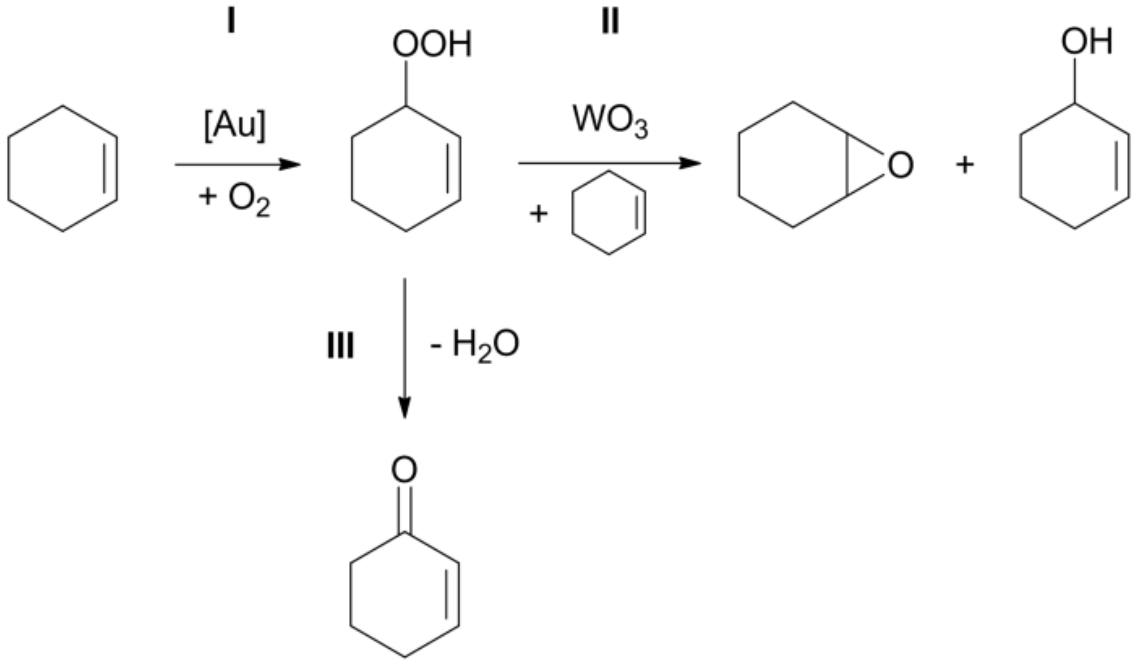

Figure 3.15 Proposed mechanism for cyclohexene oxidation.

To support this hypothesis we conducted a series of experiments in which pure WO_3 powder was mixed with $0.3Au_9/SiO_2$ at different ratios (Figure 3.16A). Interestingly, the addition of just 2 wt% of WO_3 (1 mg) changes the selectivity of the reaction, with cyclohexene oxide becoming the main product. With 10 wt% of WO_3 (5 mg) the distribution of products is almost identical to that for $0.3Au_9/WO_3$. It is possible, however, that in this series of experiments some gold species leach from silica-based catalyst and adsorb on tungsten oxide, thus forming a catalytic system with high selectivity towards cyclohexene oxide.

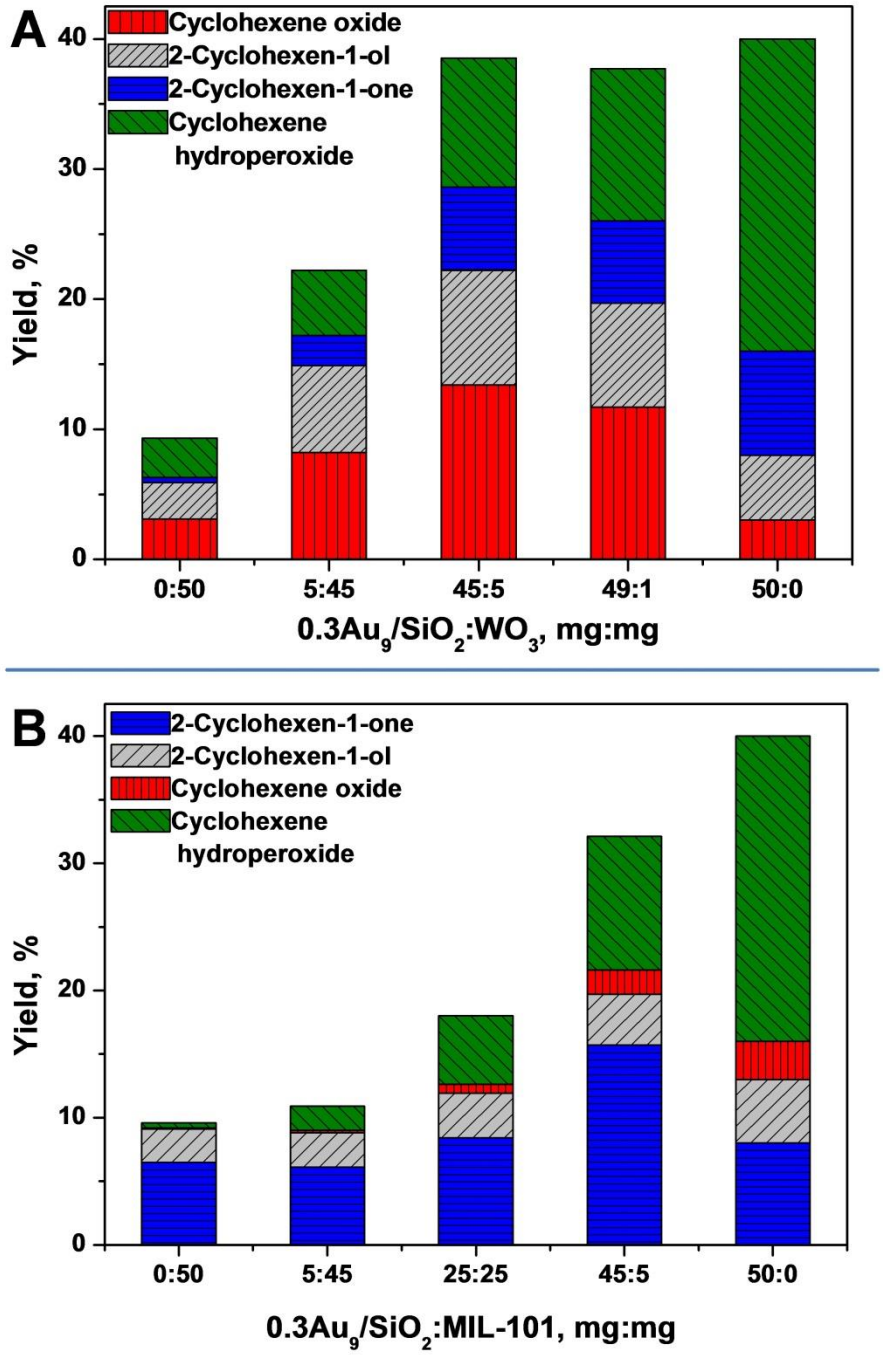

Figure 3.16 Effect of the co-catalyst on the selectivity in cyclohexene oxidation.

To exclude this possibility we performed a reaction with the silica-based catalyst, hot filtered the reaction mixture into a vial containing tungsten oxide (5 mg),

which was then collected by centrifugation. Inasmuch as potentially impregnated WO_3 was inactive in the conversion of the fresh cyclohexene, we conclude that the observed change of selectivity upon addition of WO_3 to Au/SiO_2 catalyst should be attributed to properties of pure WO_3 acting as a co-catalyst rather than to a synergistic effect between support and Au nanoparticles. The discovered ability of WO_3 to activate cyclohexenyl hydroperoxide, promoting its reaction with cyclohexene, is consistent with reports on activation of H_2O_2[160] and alkyl hydroperoxides[161] by WO_3 through the formation of peroxo complexes of tungsten which are highly active and selective in the epoxidation of olefins.[162]

We also found that the use of different co-catalyst can shift selectivity of Au/SiO_2 towards allylic oxidation products. As such a co-catalyst, we have chosen metal-organic framework MIL-101, which was recently reported as a catalyst for allylic oxidation of cyclohexene with molecular oxygen, with 2-cyclohexen-1-one being the main product.[163, 164] Results of catalytic testing of the mixture consisting of pure MOF and $0.3Au_9/SiO_2$ in different ratios show the effect of altering the selectivity of reaction similar to the one found for WO_3, but with 2-cyclohexen-1-one becoming the main product (Figure 3.16B). It could be suggested that MIL-101 catalyses the conversion of cyclohexenyl hydroperoxide to 2-cyclohexene-1-one (reaction III, Figure 3.15). Reaction catalysed by the mixture of MIL-101:$0.3Au_9/SiO_2$ (5:45, mg:mg) gives the maximum 2-cyclohexen-1-one yield of 16%, which is twice the yield we have been able to achieve with the pure MOF.

3.4. Conclusions

In this Chapter we have prepared a series of SiO_2-, TiO_2- and WO_3-supported gold catalysts by deposition of Au_9 and Au_{101} clusters. It was found that under the conditions of solvent-free aerobic oxidation of cyclohexene, clusters sinter into larger

nanoparticles with mean diameters ranging from *ca.* 4 to 10 nm, depending on the gold loading and the type of cluster. Leaching of gold species occurs during the first catalytic cycle but becomes undetectable after further cycles. Using a series of catalytic tests we have shown that leached gold species are inactive in cyclohexene oxidation.

We found that Au nanoparticles catalyse the formation of cyclohexenyl hydroperoxide, which can be converted to other products in the presence of different heterogeneous co-catalysts. Cyclohexene oxide is formed *via* the reaction of cyclohexenyl hydroperoxide with cyclohexene catalysed by WO_3, either present as a support or introduced to the reaction as a co-catalyst physically admixed with silica-supported gold catalyst. Selectivity towards formation of 2-cyclohexen-1-one can be shifted by using MIL-101 as a co-catalyst for gold supported on SiO_2.

We have shown that careful choice of support or co-catalyst for supported gold nanoparticles can tune the selectivity of cyclohexene oxidation towards cyclohexene oxide or 2-cyclohexen-1-one under solvent-free conditions without addition of radical initiator and using oxygen as the only oxidant. The results of this Chapter were published in D. S. Ovoshchnikov, B. G. Donoeva, B. E. Williamson and V. B. Golovko, *Catalysis Science & Technology*, 2014, **4**, 752-757 - Published by The Royal Society of Chemistry.

The findings of this Chapter indicate that it is agglomerated nanoparticles that are responsible for the catalytic activity, not the small clusters. Careful investigation of this phenomenon and formulation of the size effect of gold entities in cyclohexene oxidation are presented in Chapter 4.

Chapter 4 - Establishing a Au Nanoparticle Size Effect in the Oxidation of Cyclohexene

Work on this Chapter was performed in collaboration with Baira Donoeva, who performed TEM and catalytic studies of some catalysts. Also, discussions and formulation of ideas and experiments were done together with Baira.

4.1. Introduction

One of the crucial parameters determining the catalytic activity of gold is the size of gold particles, *e.g.* only particles with sizes below 5 nm are active in the low-temperature CO oxidation and their activity increases with decrease of the particle size.[81, 165-167] Attempts were also made to establish particle size effects for the liquid-phase oxidation reactions of larger organic molecules catalysed by supported gold nanoparticles. However, opposite trends in the effects of Au particle size on their catalytic activity in the same reactions are frequently reported.[31, 168-173] Typically, particle size effects are studied by comparing catalytic activities within a series of supported gold nanoparticles with different mean diameters, which are assumed to be constant during the reaction.[169, 171, 174, 175] Gold particles within such series are often prepared using different wet chemistry methods, which could affect the catalytic activity, thus obscuring the effect of the particle size. One of the findings of the work described in the previous Chapter is that triphenylphosphine-stabilized gold clusters were unstable during the cyclohexene oxidation and gradually agglomerated to form larger particles. In this Chapter we show how such particles that change their size

during the catalytic reaction could be employed for the investigation of particle size effect. Because catalytic activity can be observed only when active sites are present, monitoring of the catalytic activity along with the state of catalyst in such gradually changing system could provide insight regarding the optimal catalyst morphology. In this Chapter, we employed silica-supported phosphine-stabilized Au clusters with initial sizes below 2 nm and studied their activity in solvent-free aerobic oxidation of cyclohexene. By combining the investigation of cyclohexene oxidation kinetics with the monitoring catalyst transformations we established an Au nanoparticles size effect on their catalytic activity.

4.2. Experimental

4.2.1. Catalyst preparation

Au_9 and Au_{101}-based catalysts were prepared as described in Chapter 3. Briefly, clusters were synthesized according to the previously published methods[147, 148] and deposited on SiO_2 from dichloromethane solution.

Deposition of Au_9 cluster onto SBA-15 was performed using the methodology similar to the one described by Liu *et al.*[176] SBA-15 (synthesized by Baira Donoeva, 500 mg) was suspended in the mixture of C_2H_5OH and CH_2Cl_2 (5 mL, 1:4). Solution of Au_9 cluster (2.3 mg) in the same solvent mixture (5 mL) was slowly added to the suspension of SBA-15 under vigorous stirring. The mixture was stirred for 2.5 h. The solid was collected *via* centrifugation, washed with CH_2Cl_2 (10 mL) and dried under vacuum at room temperature.

Additionally, several catalysts were prepared *via* deposition of different gold colloids onto SiO_2. Stabilizer-free gold nanoparticles were synthesized using method reported by Martin *et al.*[177] Briefly, to 10 mL of Milli-Q water solutions of $HAuCl_4$ (100 µL, 50 mM) and later of $NaBH_4$ (300 µL, 50 mM) were added, while agitating on

mechanical shaker for 1 min. As-prepared solution of gold nanoparticles was filtered through the 0.2 μm filter and the concentration of gold in filtrate was established using AAS. A calculated volume of fresh Au nanoparticles solution in water was added to SiO_2 (0.5 g). The mixture was sonicated for 1 minute and water was slowly removed from the suspension using rotary evaporator (temperature of bath was ca. 30 ºC). After deposition onto SiO_2, the average diameter of Au particles was 9.1 nm. Citrate-stabilized Au nanoparticles were prepared following a protocol described by Turkevich *et al*.[86] Briefly, 450 mL of 0.24 mM $HAuCl_4$ and 1.6 mM sodium citrate solution was heated at 70 ˚C for 1 hour. The resulting red solution containing 13.9 nm Au particles was cooled down using an ice bath. 33.9 nm particles were prepared by heating 50 mL of 0.3 mM $HAuCl_4$ and 0.58 mM sodium citrate solution at 90 ˚C for 5 minutes. 47.4 nm particles were prepared by heating 50 mL of 1.2 mM $HAuCl_4$ and 1.9 mM sodium citrate at 60 ˚C for 2 hours. The resulting solutions of colloid Au particles were filtered through the 0.2 μm filter and analysed *via* AAS. A calculated volume of fresh Au nanoparticles solution in water was added to SiO_2 (0.5 g). The mixture was sonicated for 1 minute and water was slowly removed from the suspension using rotary evaporator (temperature of bath was ca. 30 ºC). The resulting solid was collected, dried under vacuum at room temperature and characterized using TEM.

4.2.2. Catalysts characterization

Catalysts were characterized using TEM, DR UV-vis and AAS (see Chapter 3 for details). X-ray photoelectron spectroscopy (XPS) of WO_3-based catalysts was performed at the Soft X-ray Beamline at the Australian Synchrotron using a SPECS Phoibos 150 hemispherical electron analyser with the photon energy set to 690 eV. The samples were deposited onto silicon wafer using drop coating technique. The

wafers were then attached to sample holder using carbon tape. Because of the strong charging effects, caused by the high intensity of the synchrotron beam/imperfections of sample preparation techniques available at the facility, we were unable to collect data on silica-based catalysts on the Synchrotron beam line. Therefore, the XPS analysis of SiO_2-based catalysts was conducted on a Kratos Axis DLD spectrometer with a monochromated Al-Kα X-ray source (performed by Dr Colin Doyle from Research Centre for Surface and Materials Science (RCSMS), at the University of Auckland). The samples were pressed into indium as the mounting medium. A supply of low-energy electrons was used for charge neutralization. Survey spectra were recorded with a pass energy of 80 eV and high-resolution spectra with a pass energy of 40 eV. Binding energies were normalized with respect to the position of the adventitious carbon C1s peak at 285.0 eV. Modelling of the data was performed using CasaXPS program (SiO_2-based samples) or MS Excel (WO_3-based samples). The background was simulated using the empirical Shirley method[178] (Equation 1, the case of the background under 2 peaks):

$$S(E) = I_2 + k\frac{A2(E)}{(A1(E)+A2(E))} \quad (1),$$

where *S(E)* is the background intensity at energy *E*, *A1* and *A2* – areas under peaks, *k* defines the step in background and is equal to $(I_1\text{-}I_2)$. Calculation of the Shirley background is performed *via* iteration: the integrated areas *A1(E)* and *A2(E)* are initially calculated from the approximation of *S(E)*, then refined using the background computed from the first approximation as input to improve the values computed for *A1(E)* and *A2(E)*. The peaks were fitted using either sum of Lorentzian and Gaussian functions[179] (MS Excel, equation 2) or Gaussian/Lorentzian product[180] (CasaXPS, equation 3):

$$SGL\ (x; F, E, m) = (1-m)\exp\left(-4ln2\frac{(x-E)^2}{F^2}\right) + m/(1+4\frac{(x-E)^2}{F^2}) \quad (2)$$

$$GL(x;F,E,m) = \exp\left(-4ln2(1-m)\frac{(x-E)^2}{F^2}\right)/(1+4m\frac{(x-E)^2}{F^2}) \quad (3)$$

where F is the full width at half maximum, E – position of the maximum of the peak, and m – mixing coefficient (0.3).

4.2.3. Catalyst testing

The catalytic activity of Au catalysts was tested in aerobic solvent-free cyclohexene oxidation without addition of a radical initiator. Kinetic studies of cyclohexene oxidation were performed in a glass reactor equipped with a reflux condenser similar to the one used in Chapter 3. 10 mL of cyclohexene containing 0.2 M of n-decane as an internal standard, 100 mg of catalyst and Teflon-coated magnetic stirrer were loaded into 100 mL 2-necked glass round bottom flask. The system was flushed with O_2 three times and connected to a rubber balloon filled with O_2. The mixture was magnetically stirred at 65 °C. Samples of the reaction mixture were taken using a glass syringe through the attachment with a Teflon septa connected to the second neck of the round-bottom flask. The reaction was stopped by cooling the reactor to room temperature; the condenser was rinsed with 5 mL of diethyl ether and the reaction mixture was separated from the solid catalyst by centrifugation. Catalysts were washed with diethyl ether and dried under vacuum at room temperature before recycling. Catalyst samples from separate experiments were accumulated to obtain the required mass of the catalyst for recycling. Each experiment was reproduced at least three times. The typical standard errors of independent catalytic tests were below 1.5 %. Analysis of the reaction mixtures was performed *via* GC-FID and GC-MS (see Chapter 3 for details).

4.3. Results and discussion

4.3.1. Induction period

In the previous Chapter we have observed that the gold nanoparticles formed from the <2 nm clusters, that were originally deposited on the supports, preserve their activity throughout several recycling steps, which is an indication that the sintered clusters are the active site of the reaction. We have also observed an induction period in the oxidation of cyclohexene, catalysed by as prepared catalysts, which is studied in more detailed in this Chapter.

We found that the length of the induction period depended on the Au loading of the catalyst (Figure 4.1A): the decrease of the Au loading of Au_9/SiO_2 from 0.5 to 0.02 wt% led to the elongation of the induction period from *ca.* 1 to 6.5 h. The length of the induction period also depended on the type of Au cluster: $0.1Au_{101}/SiO_2$ showed a significantly shorter induction period of 50 minutes compared with 3.5 hours for $0.1Au_9/SiO_2$ (Figure 4.1B).

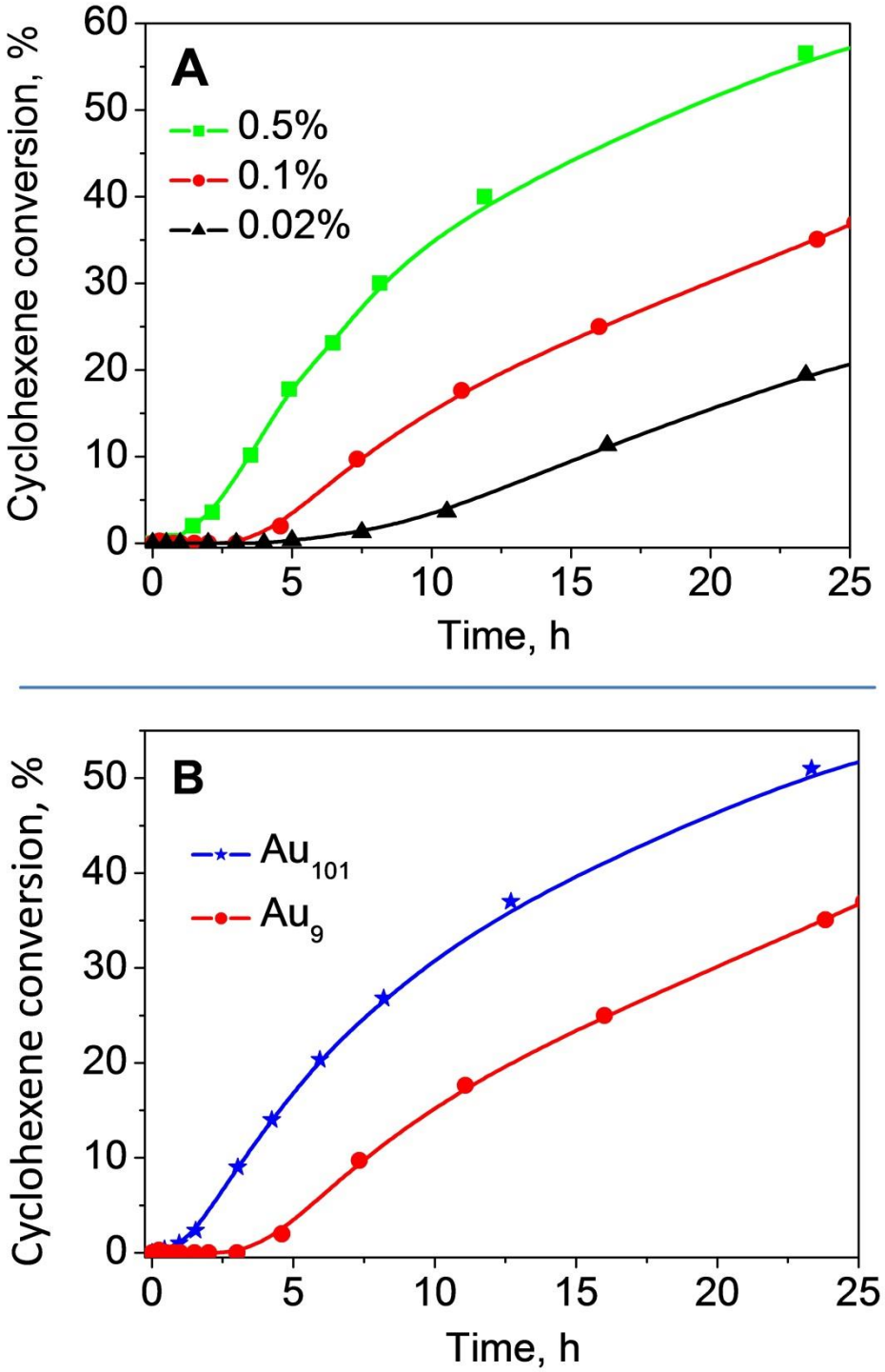

Figure 4.1 Cyclohexene oxidation catalysed by (A) Au_9/SiO_2 with gold loadings of 0.5, 0.1 and 0.02% and (B) $0.1Au_{101}/SiO_2$ and $0.1Au_9/SiO_2$. Conditions: solvent-free cyclohexene, 10 mL, O_2 1 atm, 65 °C, catalyst 0.1 g.

A change of the Au particle size during the reaction was monitored using transmission electron microscopy (TEM) and diffuse-reflectance UV-visible spectroscopy (DR UV-vis). TEM micrographs of $0.5Au_9/SiO_2$ sampled from the reaction after 0.5, 1 and 16 h are shown in Figure 4.2B-D.

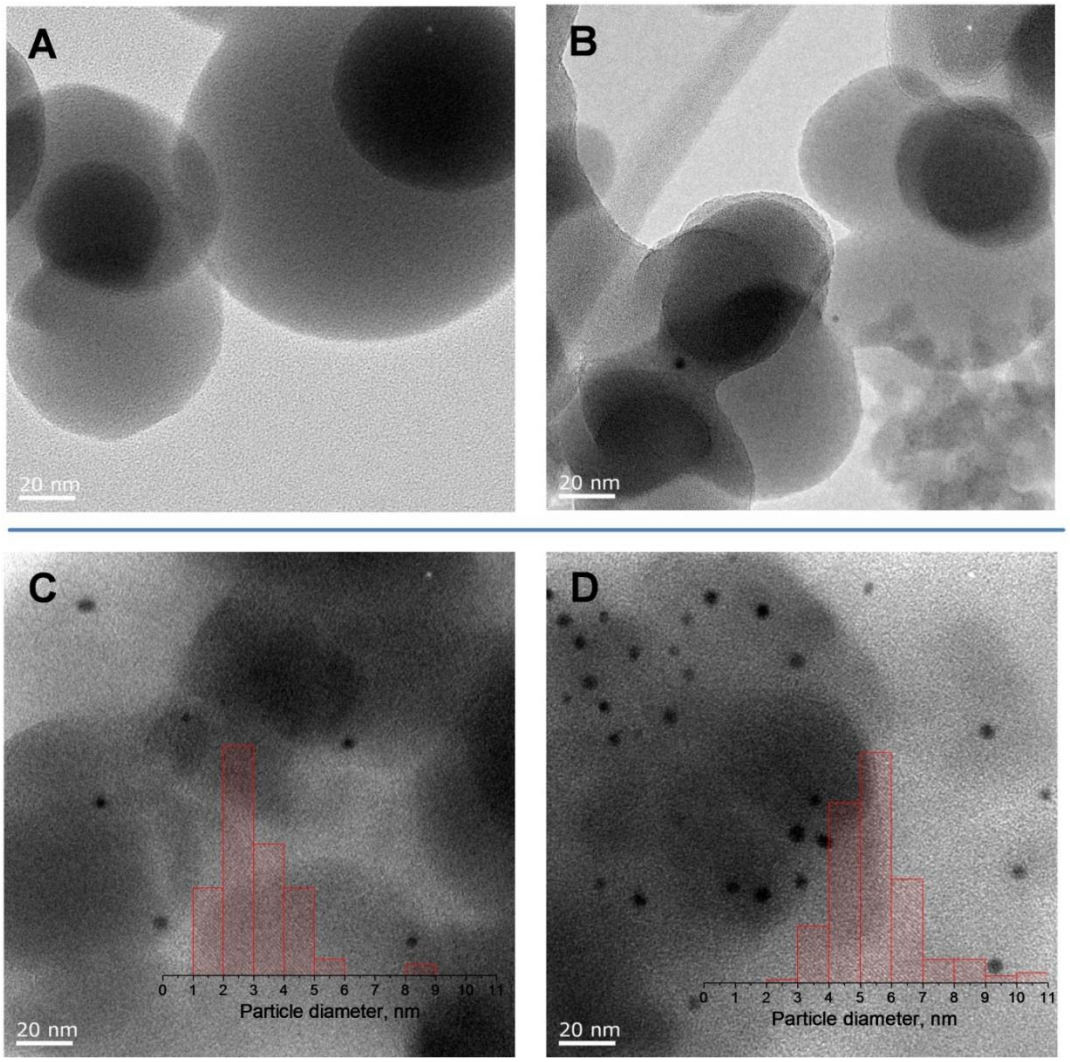

Figure 4.2 TEM micrographs of as-made $0.5Au_9/SiO_2$ (A) and $0.5Au_9/SiO_2$ sampled from the reaction after 0.5 h (B), 1 h (C), and 16 h (D).

Intact Au_9 clusters of as made $0.5Au_9/SiO_2$ are not visible in bright-field TEM images because of the poor contrast for supported Au clusters smaller than 1 nm (Figure 4.2A). During the reaction, larger particles, detectable by TEM, gradually form. The number of visible particles increases during the course of reaction, which is

indicated by the increase of the surface density of visible particles: *ca.* 40, 170 and 370 particles/μm^2 were detected in TEM micrographs of $0.5Au_9/SiO_2$ sampled from the reaction after 0.5, 1 and 16 h, respectively. The surface density of particles was estimated by counting the number of particles that could be observed on *ca.* 20 micrographs taken at 97kx magnification (frame size $3.2 \cdot 10^3$ nm^2). The mean diameter of detectable particles was 3.1 ± 0.1 (s.d. 1.2) nm after 1 h of reaction and it increased further to 5.4 ± 0.1 (s.d. 1.4) nm during the next 15 h. The evolution of the particle size as a function of time for $0.5Au_9/SiO_2$ is shown in Figure 4.3.

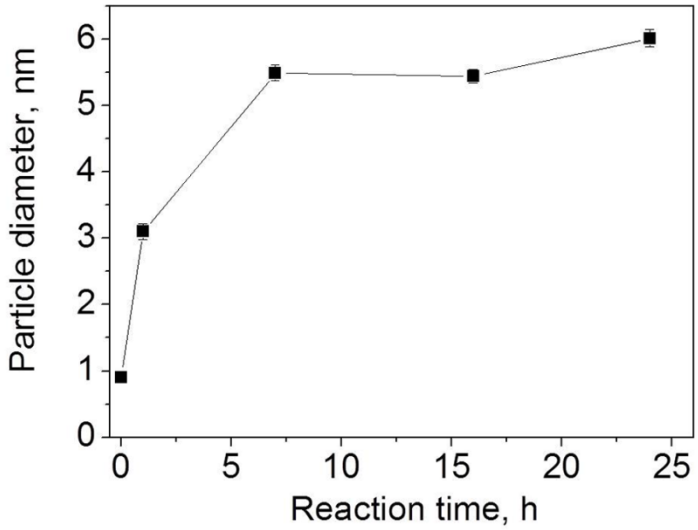

Figure 4.3 Evolution of the size of visible Au particles of $0.5Au_9/SiO_2$ during cyclohexene oxidation. t = 0 – the size of the unsupported cluster.

DR UV-vis study of $0.5Au_9/SiO_2$ showed the appearance of the surface plasmon resonance (SPR) band at 520 nm for samples of catalyst recovered after 1 h of reaction. Because only particles larger than 2 nm possess SPR, the appearance of SPR band indicates the formation of gold particles larger than 2 nm (Figure 4.4A).[181-183] Hence, both TEM and DR UV-vis studies of $0.5Au_9/SiO_2$ show the similar time of formation of particles larger than 2 nm.

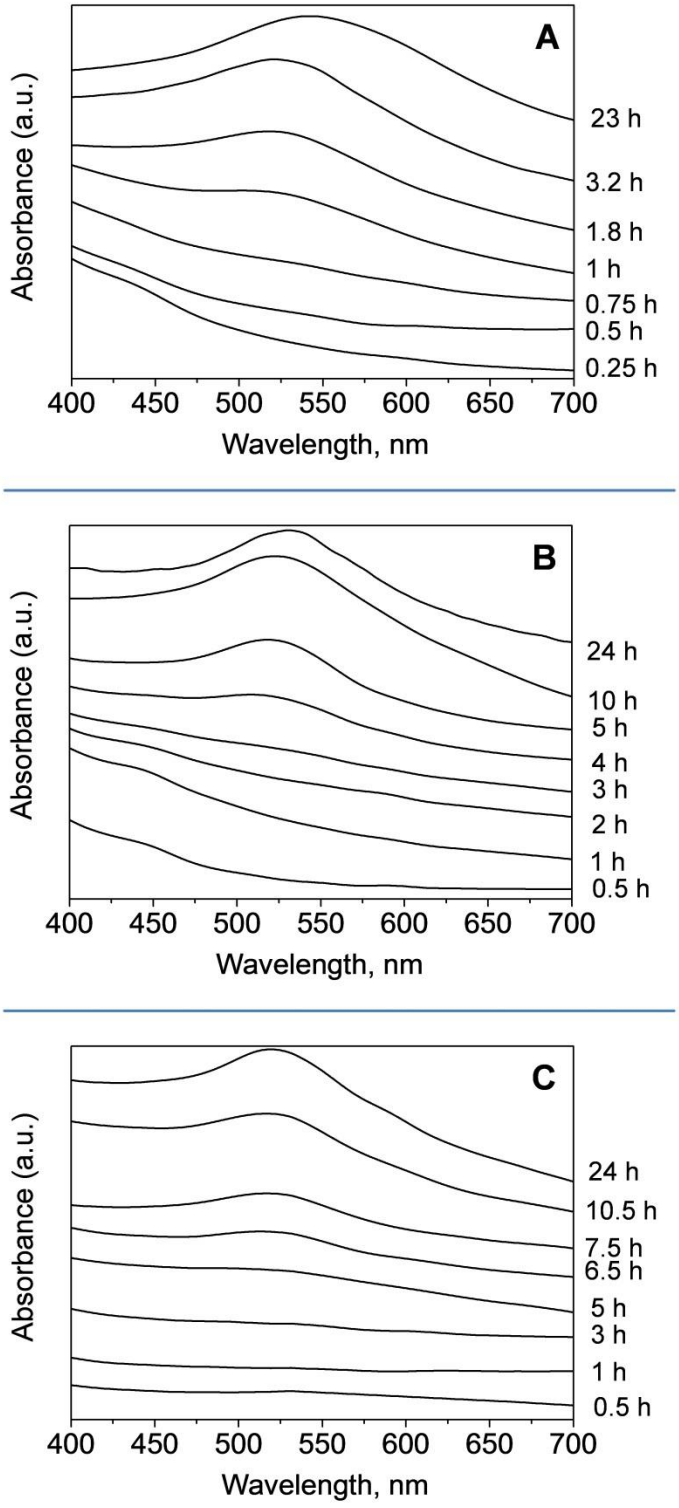

Figure 4.4 DR UV−vis spectra of $0.5Au_9/SiO_2$ (A), $0.1Au_9/SiO_2$ (B), and $0.02Au_9/SiO_2$ (C) sampled at reaction times indicated along the right-hand ordinates.

DR UV-vis studies of $0.1Au_9/SiO_2$ and $0.02Au_9/SiO_2$ showed that particles larger than 2 nm form only after *ca.* 4 and 6.5 h, respectively. Slower gold agglomeration for catalysts with lower Au loadings is most likely due to the lower density of Au particles on SiO_2 surface. As seen from the kinetics of cyclohexene oxidation (Figure 4.1A) and DR UV-vis data, in all cases formation of sufficient number of particles larger than 2 nm was accompanied with the appearance of catalytic activity, which indicates that such particles are active in cyclohexene oxidation. At the same time, there is no induction period in the kinetics of the cyclohexene oxidation catalysed by the Au_9/SiO_2, recycled after 16 h catalytic run - the catalyst which already contains gold nanoparticles larger than 2 nm (Figure 4.5). This fact supports the conclusion that particles larger than 2 nm are active in the cyclohexene oxidation.

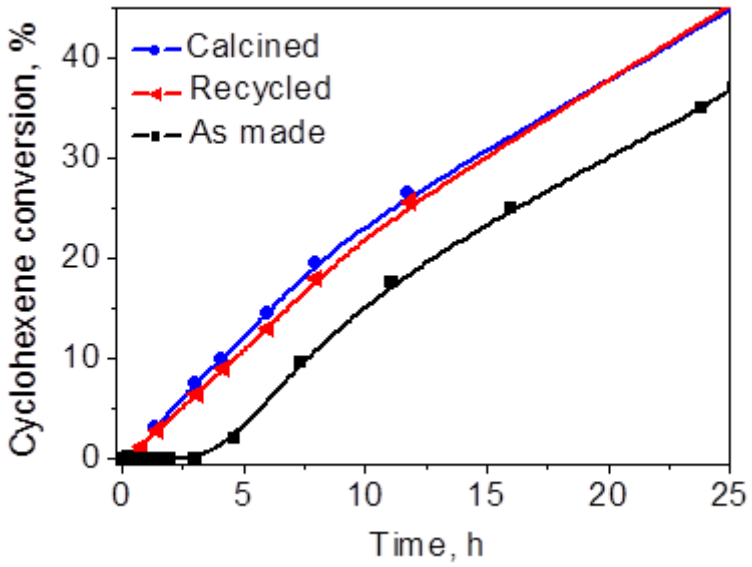

Figure 4.5 Cyclohexene oxidation catalysed by as-made, recycled, and pre-calcined $0.1Au_9/SiO_2$.

4.3.2. Presence of ligands *vs* nanoparticle size

Importantly, cyclohexene used for catalytic oxidation did not contain 2,6-di-tert-butyl-4-methylphenol, which is typically added as a stabilizer by chemical suppliers. When we used cyclohexene that contained the stabilizer, the Au_9 clusters did not agglomerate after 16 h under typical reaction conditions (65 °C, 1 atm O_2) and no cyclohexene conversion was observed. Stirring $0.5Au_9/SiO_2$ for 16 h under typical reaction conditions, but in n-hexane instead of cyclohexene, also did not lead to cluster agglomeration. These results imply that thermal treatment at 65 °C alone is not enough to induce agglomeration of Au_9 supported on SiO_2. We suggest that phosphine ligands were removed from the cluster *via* reaction with cyclohexenyl hydroperoxide (CyOOH), which is present in trace amounts in the stabilizer-free cyclohexene (*ca.* 0.015 wt% by GC), analogously to a recently reported removal of phosphine ligands from silica supported $[Au_6(Ph_2P(o\text{-}tolyl))_6](NO_3)_2$ by tert-butyl hydroperoxide.[184] Agglomeration did not occur in n-hexane or stabilized cyclohexene because neither of them contained even traces of peroxides. Thus, cluster agglomeration is possible only when PPh_3 ligands are removed from the gold core of Au_9. An indication of such step-by-step *in situ* transformation of gold clusters, which includes ligand removal from the cluster cores and subsequent particle agglomeration, can also be seen in Figure 4.4B. DR UV-vis spectra of catalyst sampled in the initial stages of the reaction possessed a weak band at 450 nm, originating from intact Au_9 clusters (Figure 4.8a). The features in the optical spectra of small phosphine-stabilized gold clusters are known to be due to the effects of the ligand shell bound to the gold core of the cluster.[185] Therefore, the disappearance of the band at 450 nm before the SPR band emerges indicates that agglomeration occurs after the ligand shell is at least partially removed. Because sintering is not possible when ligands are still bound to the gold cores of the clusters,

we conclude that particles forming during the reaction are predominantly phosphine-free. This suggestion is also supported by the XPS study of analogous system Au_9/WO_3. The phosphorous signal ($2p_{3/2}$), centred at 131.8 eV, is present in the as-prepared catalyst, but is absent in the spectra of the catalyst recovered after the reaction (Figure 4.6). The disappearance of the phosphorous signal is an indication of at least partial removal of the triphenylphosphine ligands during the cyclohexene oxidation.

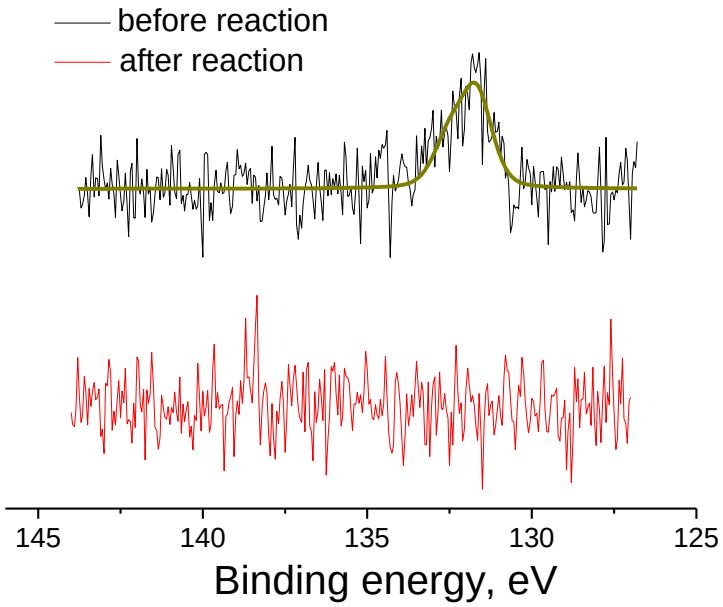

Figure 4.6 XPS 2P spectra of as made $0.1Au_9/WO_3$ (black) and $0.1Au_9/WO_3$ recovered after 16 h catalytic cycle of cyclohexene oxidation (red).

Pure Au_9 clusters lose phosphine ligands upon calcination at 230 °C for 40 min in Ar flow according to TGA (Figure 3.2). Calcination of $0.1Au_9/SiO_2$ under the same conditions in order to remove phosphine ligands from supported Au_9 led to the formation of 8.0 ± 0.3 (s.d. 2.6) nm particles (Figure 4.7B). Catalyst treated this way

showed a cyclohexene conversion profile similar to that of the recycled $0.1Au_9/SiO_2$ (particle size 9.6 ± 0.6 (s.d. 3.9) nm, Figure 4.7A), which indicates that phosphine-free particles of similar size and larger than 2 nm obtained in different ways have similar activity in the reaction (Figure 4.5).

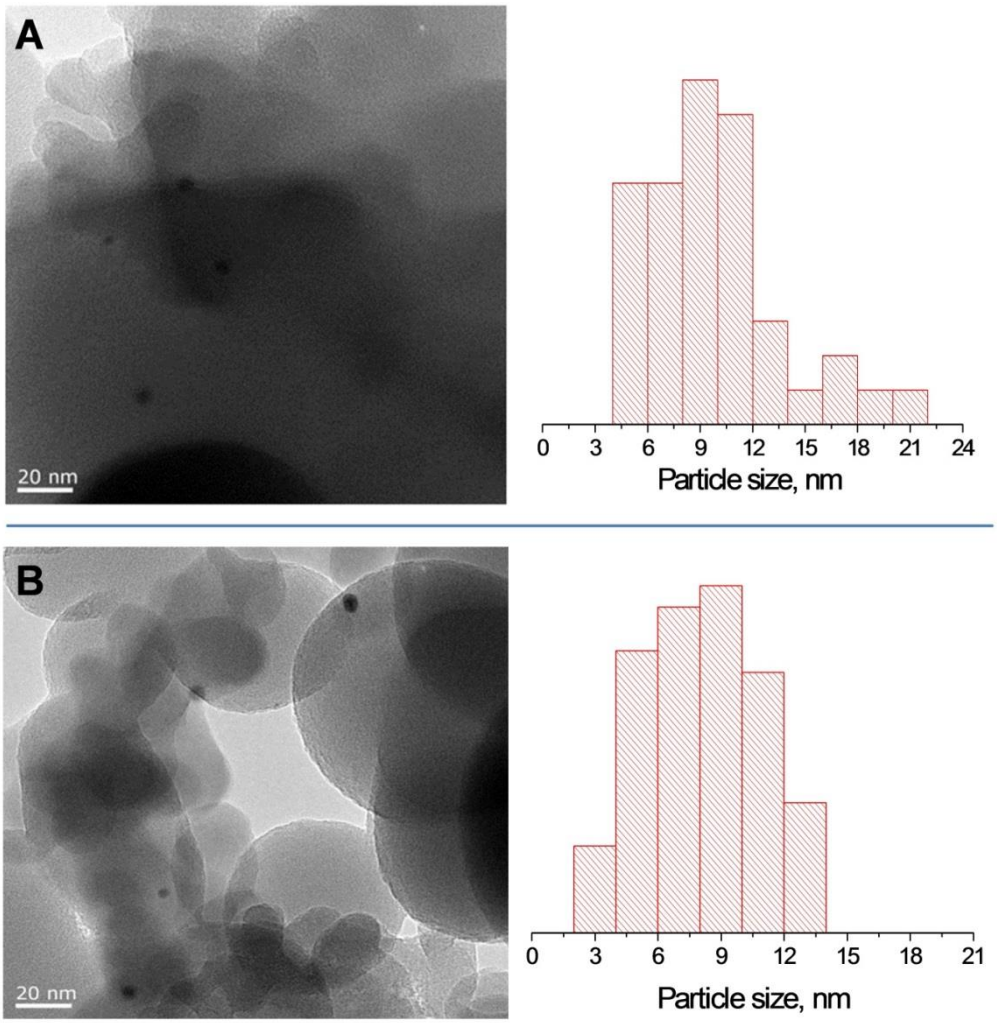

Figure 4.7 Representative TEM images and the corresponding particle size distributions of $0.1Au_9/SiO_2$ after cyclohexene oxidation (A) and calcined at 230 °C for 40 min, 1 °C/min, Ar flow 100 mL/min (B).

Inasmuch as two catalyst parameters change during the reaction, *i.e.* Au particle size and the presence of phosphine ligands, the initial inactivity of the as made catalysts could be due to one of the following: a) stabilizing ligands cover active gold

sites, thus hindering the catalytic activity; once the phosphine ligands are removed, the particles become active b) sub-2 nm gold particles, even without phosphine ligands, are inactive in cyclohexene oxidation and activity appears only after the particle size reaches a certain threshold.

Results of our experiments indicate that removal of phosphine ligands is not a sufficient condition for the appearance of catalytic activity and particle size plays a significant role:

a) As seen from DR UV-vis spectra (Figure 4.4B), the PPh_3 ligand shell was at least partially removed from Au_9 after 2 h, as indicated by disappearance of the band at 450 nm, but no activity was observed until particles larger than 2 nm had formed after *ca.* 4 hours of reaction (Figure 4.1A).

b) Because the core of Au_{101} is larger than that of Au_9, gold particles derived from Au_{101} need significantly less time to overcome the threshold in particle size, which leads to shorter induction period for Au_{101} catalyst (Figure 4.1B).

4.3.3. SBA-15-based system

To confirm that small (sub-2 nm) and phosphine-free Au particles are inactive in cyclohexene oxidation, we deposited Au_9 on SBA-15,[186] a mesoporous SiO_2-based material with large surface area (synthesized by Baira Donoeva). It was previously reported that ~1 nm ligand-free clusters deposited on SBA-15 could be obtained from analogous triphenylphosphine-stabilized gold cluster $[Au_{11}(PPh_3)_8Cl_2]Cl$.[176] In this report the sintering of the clusters during ligand removal was suppressed by the use of support with high surface area, and homogeneous distribution of clusters throughout the surface of the support. The latter was achieved by deposition of precursor from a mixture of ethanol and dichloromethane.[176] The following explanation of this method was suggested. Deposition of triphenylphosphine clusters from aprotic solvents such

as CH_2Cl_2 occurs due to interaction between the permanent dipole of OH groups of the support and a dipole induced within the phosphine layer of Au cluster. The mixture of ethanol and CH_2Cl_2 has higher permittivity, which reduces the attraction between cluster and support and leads to a more homogeneous deposition of the cluster onto the support compared to the case of pure CH_2Cl_2 as a solvent, where clusters immediately adsorb to the surface of the support. Following the same methodology, we have supported Au_9 onto SBA-15. To remove phosphine ligands from the cluster core, the catalyst was calcined at 230 °C for 40 min in Ar flow (denoted as $0.1Au_9$/SBA_c230). The large surface area of the support and the homogeneous distribution of clusters prevented particles from sintering during calcination, as evidenced by the absence of the SPR band in the DR UV-vis spectrum of $0.1Au_9$/SBA_c230 (Figure 4.8). On the other hand, the absence of absorption bands at 450, 380 and 315 nm, characteristic for the intact Au_9 cluster, indicates successful removal of ligands during calcination. TEM of $0.1Au_9$/SBA_c230 also confirmed very minimal agglomeration – only a few particles of 2-3 nm were detected, which correlates with the results obtained for Au_{11} clusters in the similar system.[176] Thus, phosphine-free sub-2 nm particles supported on SBA-15 were obtained.

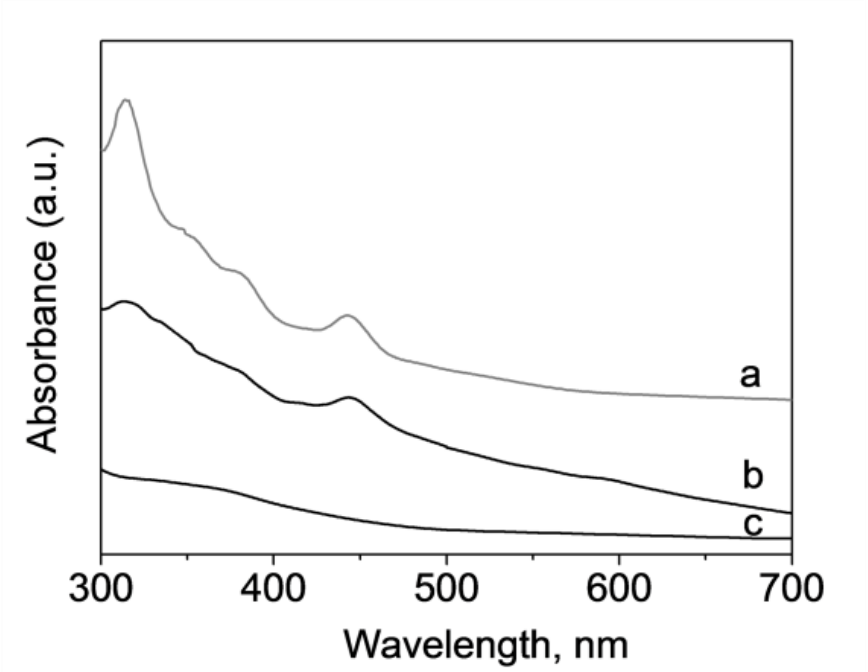

Figure 4.8 UV-vis spectrum of Au_9 dissolved in CH_2Cl_2 (a) and DR UV-vis spectra of as made $0.1Au_9$/SBA-15 (b) and $0.1Au_9$/SBA_c230 (c).

Although the Au particles were phosphine-free, the kinetics of cyclohexene oxidation in the presence of $0.1Au_9$/SBA_c230 showed an induction period of *ca.* 3.5 hours. The appearance of catalytic activity correlated with the formation of plasmonic particles (Figure 4.9), similarly to the behaviour observed for SiO_2-based catalysts, discussed earlier. Recycled $0.1Au_9$/SBA_c230 did not show an induction period in cyclohexene oxidation. This result confirmed that phosphine-free Au particles with sizes below 2 nm are inactive in the cyclohexene oxidation. The change of catalytic behaviour of Au particles once they become larger than 2 nm could be due to the transition from non-metallic to metallic properties, which occurs at sizes of *ca.* 2 nm.[187]

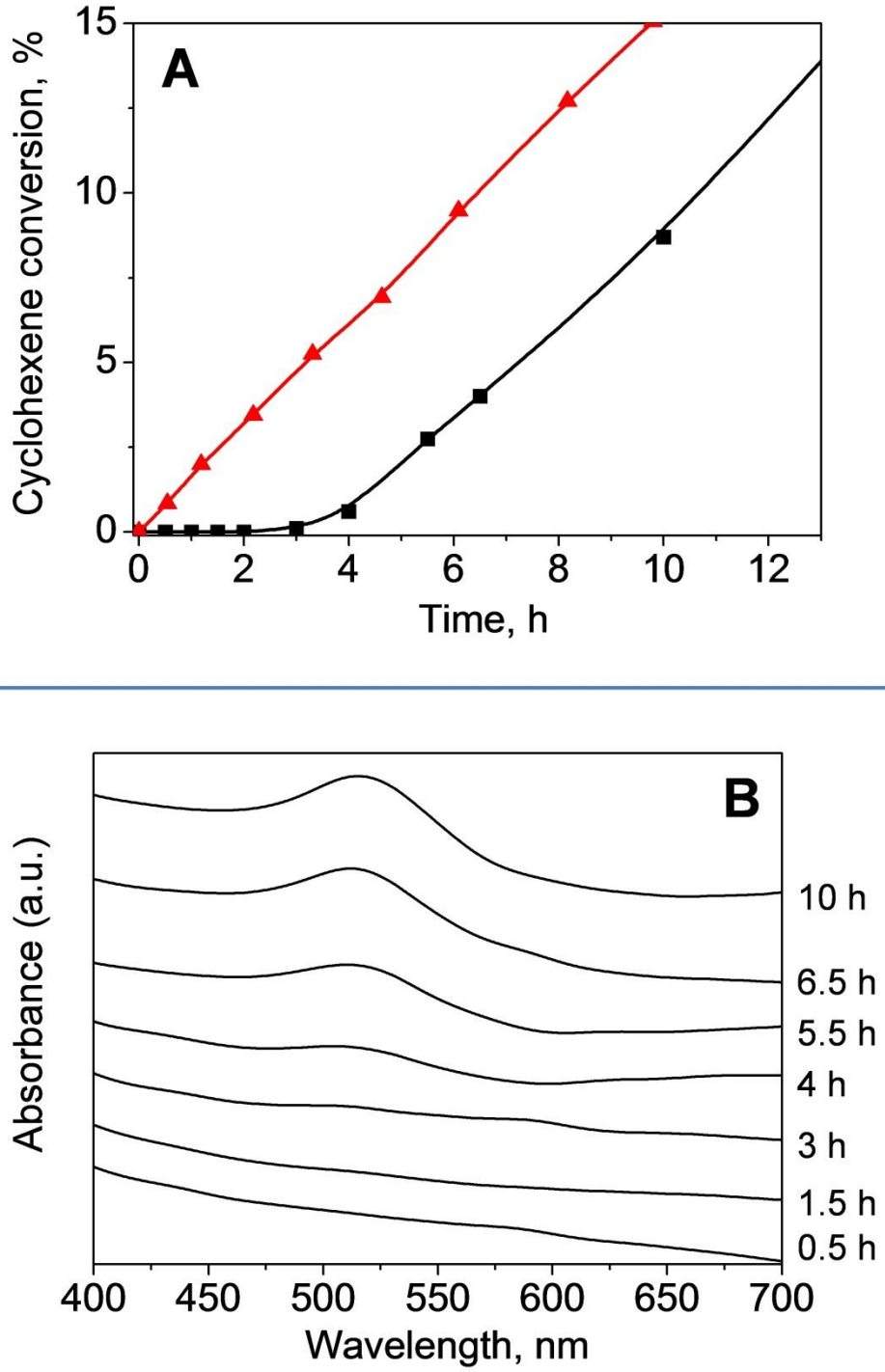

Figure 4.9 (A) Cyclohexene oxidation catalysed by 0.1Au$_9$/SBA_c230 (black) and recycled 0.1Au$_9$/SBA_c230 (red). (B) DR UV-vis spectra of 0.1Au$_9$/SBA_c230 sampled from cyclohexene oxidation at different reaction times.

4.3.4. Additional considerations

Recently, numerous reports of catalysis, driven or enhanced by the surface plasmon resonance of Au nanoparticles, have started to appear (see Introduction). Because catalytic activity in our study appeared only when gold nanoparticles larger than 2 nm, *i.e.* plasmonic particles, were formed, we investigated whether the observed activity was enabled by the SPR. We have compared the activity of $0.5Au_9/SiO_2$ in cyclohexene oxidation under ambient light with the one in the dark. Comparable activity (46% conversion in ambient light/43% in the dark) indicated that catalytic activity was mostly not enhanced by the SPR in this study.

As prepared catalysts and catalysts recovered after reaction were studied using XPS. $Au4f_{7/2}$ binding energy of Au_9 deposited on either SiO_2 or WO_3 (85 eV) is shifted towards higher energies relative to bulk gold (84 eV) due to the small size and charge of the cluster (Figure 4.10).[188, 189] No signal from pristine Au_9 clusters was detected in the post-reaction catalysts, indicating that most of the gold present in the catalytic system is in the metallic state and no intact clusters are left after the reaction. Because of the small scanning depth of the beam (due to the small mean free path of electron), sensitivity of XPS is much higher towards smaller particles; hence, the absence of peak centred at 85 eV is a strong indication that no unsintered Au_9 clusters are left after reaction. For the same reason, increase in particle size leads to a decrease in Au peak intensity. Unlike the recently reported activity of positively charged 20-150 nm Au nanoparticles in styrene oxidation,[168] catalytic activity in our case was solely due to the metallic Au^0 particles, as evidenced by the activity of the post-reaction catalysts in the second catalytic cycle.

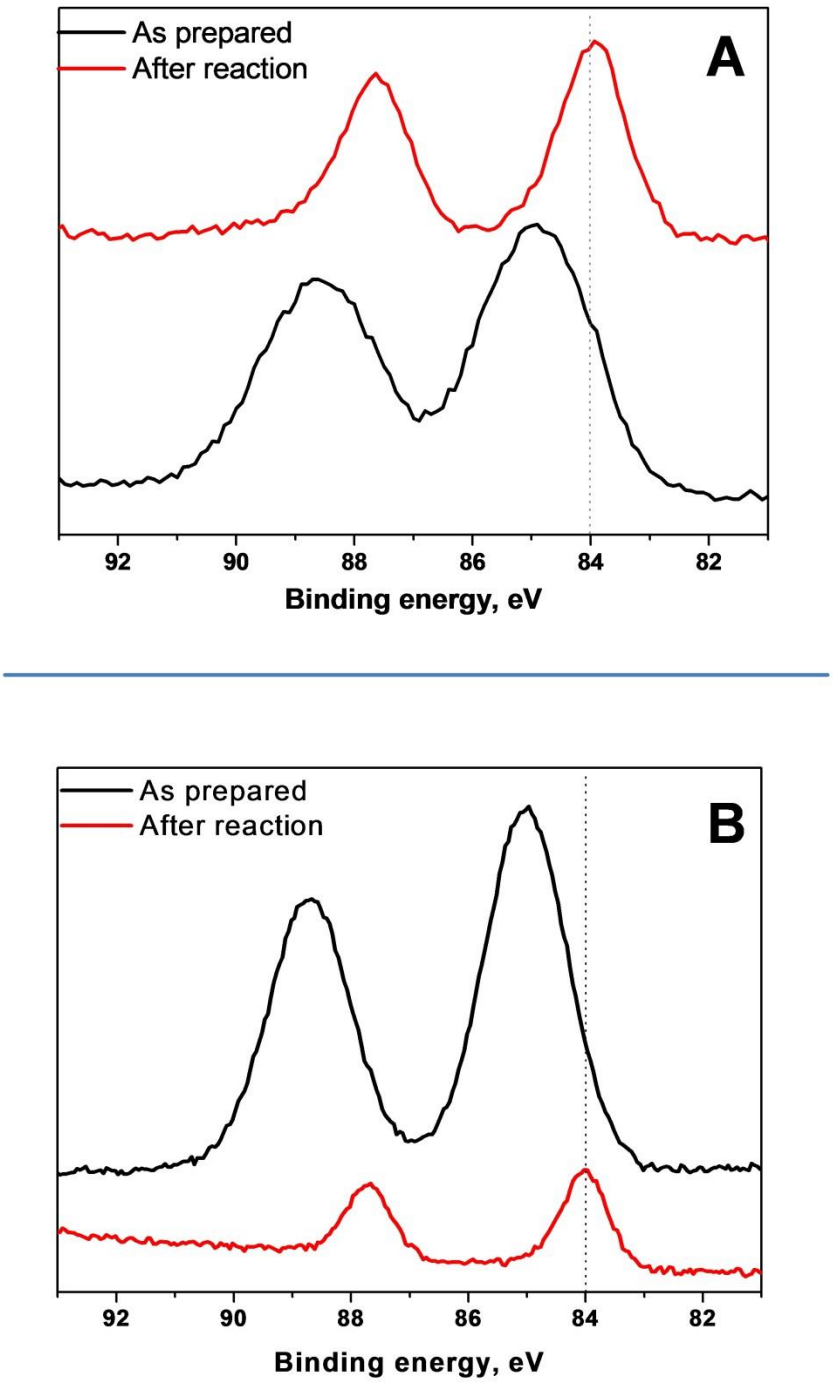

Figure 4.10 XPS Au4f spectra of (A) $0.5Au_9/SiO_2$ and (B) $0.3Au_9/WO_3$: as made (black line) and recovered after 16 h catalytic cycle of cyclohexene oxidation (red line). Dotted vertical line indicates $Au4f_{7/2}$ peak position corresponding to metallic gold.

Finally, we tested the activity of catalysts obtained by deposition of colloid stabilizer-free[177] and citrate-stabilized[86] Au nanoparticles onto SiO_2. Four catalysts 0.1Au-9.1/SiO_2, 0.1Au-13.7/SiO_2, 0.1Au-33.9/SiO_2 and 0.1Au-47.4/SiO_2 with particle sizes of 9.1, 13.7, 33.9 and 47.4 nm, respectively, and with the total gold loadings of 0.1 wt% were prepared (Figure 4.11).

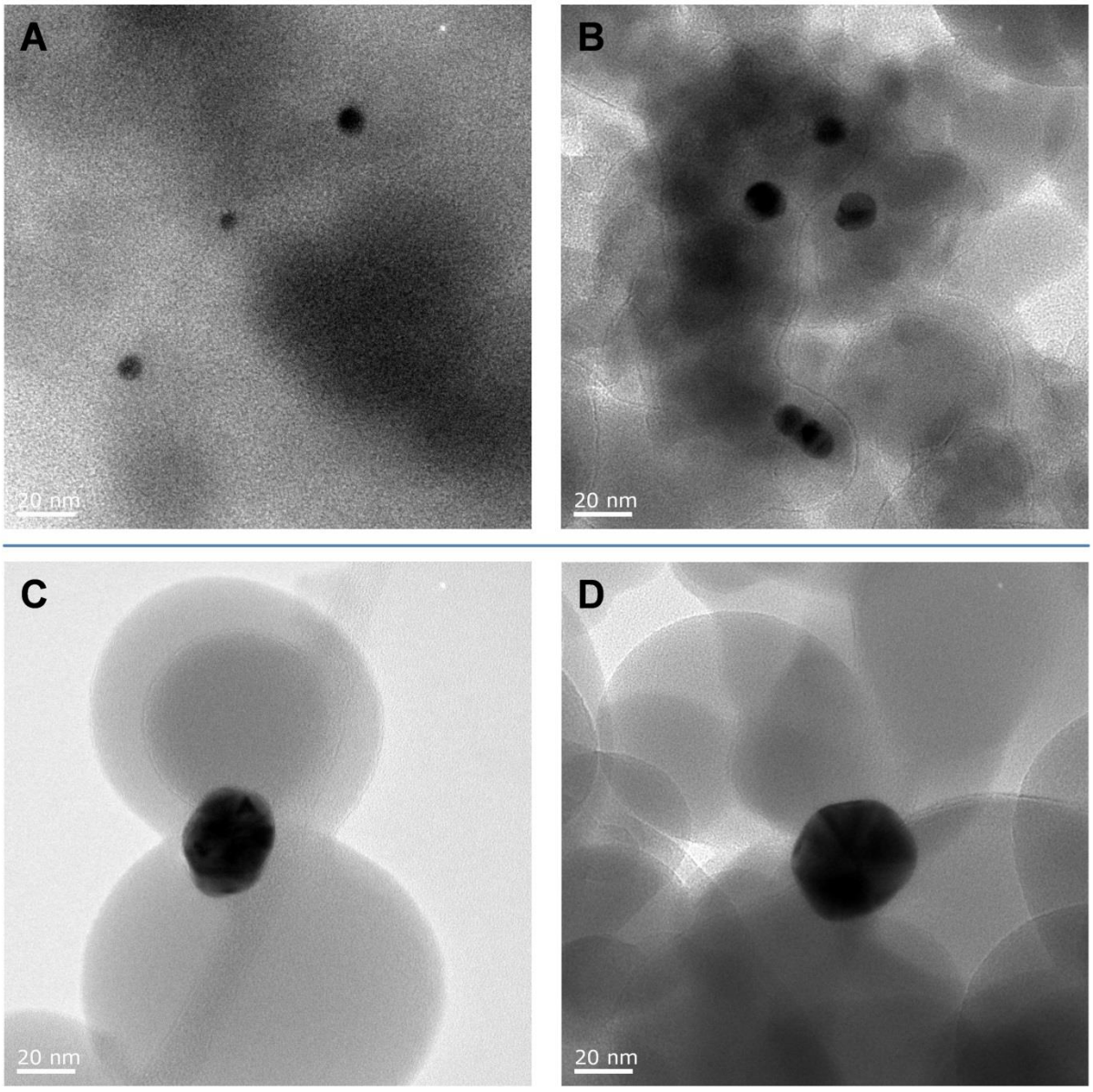

Figure 4.11 Representative TEM images of colloid 9.1 nm (A), 13.7 nm (B), 33.9 nm (C) and 47.4 nm (D) Au particles immobilized on SiO_2 (0.1 wt% Au).

All the catalysts were active in cyclohexene oxidation and no induction period was observed (Figure 4.12). Comparison of initial reaction rates and turnover frequencies (TOFs) of the Au colloid-based catalysts is shown in Table 4.1. TOFs in this case were calculated according to the equation: $TOF, s^{-1} = \frac{n^0_{substrate} - n_{substrate}}{time(s) \cdot n^{surface}_{Au}}$, where $n^0_{substrate}$ is initial number of moles of the substrate, $n_{substrate}$ is a number of moles left in the reaction after time (s) and n_{Au} is the number of moles of surface Au atoms, estimated according to the particle geometry. The catalytic activity of $0.1Au/SiO_2$ gradually decreased with the increase of Au particle size, which is in accordance with the smaller fraction of surface Au atoms for larger particles. Indeed, TOF values normalized by surface Au are very close for differently sized supported Au nanoparticles (Table 4.1). This result confirms that Au^0 particles larger than 2 nm are responsible for the observed catalytic activity in the oxidation of cyclohexene.

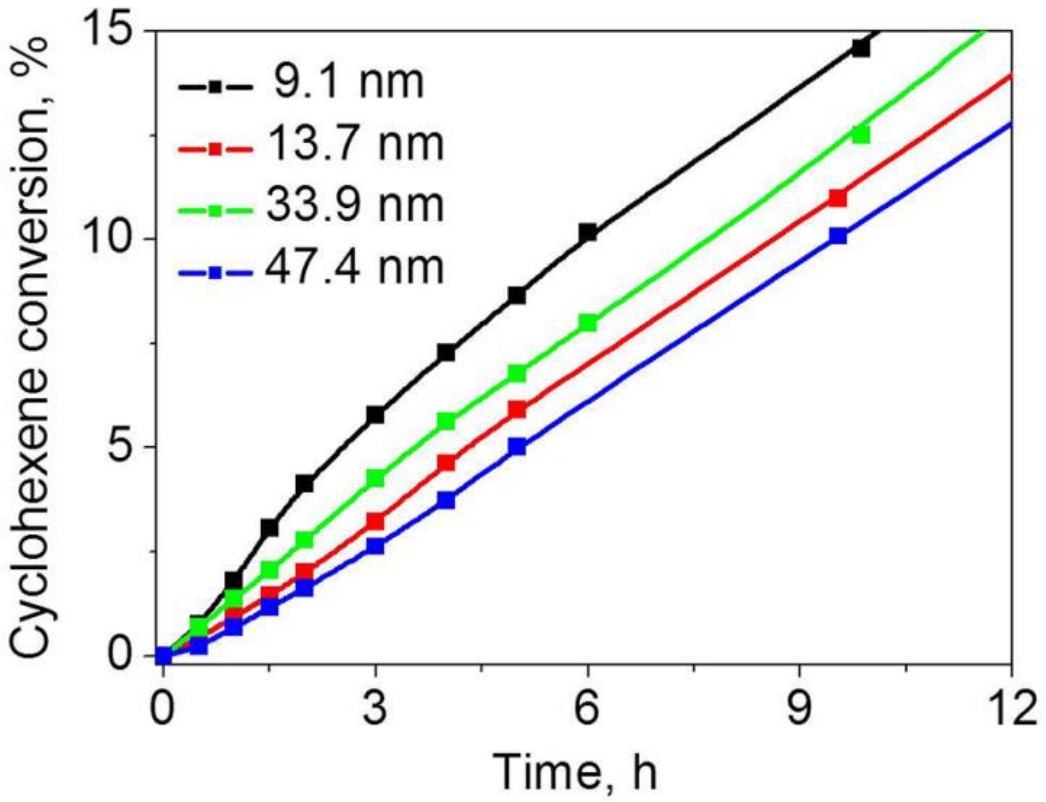

Figure 4.12 Cyclohexene oxidation catalysed by 9.1, 13.7, 33.9 and 47.4 nm Au particles supported on SiO_2 with the total gold loading of 0.1 wt%.

Table 4.1 Comparison of initial reaction rates and TOFs of Au/SiO_2 catalysts in cyclohexene oxidation.

Catalyst	Reaction rate, $mol_{substrate}/s$ ($\times 10^{-6}$)	TOF_{Au}, s^{-1}	$TOF_{surface\ Au}$, s^{-1}
$0.1Au\text{-}9.1/SiO_2$	0.58	1.14	17.5[a]
$0.1Au\text{-}13.7/SiO_2$	0.39	0.78	18.0[a]
$0.1Au\text{-}33.9/SiO_2$	0.28	0.53	21.7[b]
$0.1Au\text{-}47.4/SiO_2$	0.20	0.40	18.9[b]

Fraction of surface Au atoms was estimated assuming [a]spherical and [b]cuboctahedral shape of Au nanoparticles.

In this Chapter we showed that only Au^0 particles larger than 2 nm were active in aerobic cyclohexene oxidation; however, oxygen adsorption and its dissociative activation on large metallic gold particles were shown to be extremely impeded.[190, 191] On the other hand, extended gold surfaces were long known to catalyse hydrogen abstraction from hydrocarbons,[192] and thus activation of cyclohexene rather than O_2 by gold nanoparticles is the more probable pathway in our case. This suggestion is also supported by the fact that the main product of cyclohexene oxidation in this work is cyclohexenyl hydroperoxide, which is formed in the reaction between dissolved oxygen and cyclohexenyl radicals generated *via* allylic hydrogen abstraction from cyclohexene. When a sufficient amount of cyclohexenyl hydroperoxide is formed it further acts as a radical chain propagator in cyclohexene autoxidation.[157] A similar mechanism was recently described for cyclohexane oxidation catalysed by Au/MgO.[193] Higher activity of Au catalysts in cyclohexene oxidation compared to cyclohexane oxidation[169, 193, 194] can be explained by more facile H-abstraction from an allylic position because allylic C-H is weaker than alkylic C-H bond.

Thus, we showed that at low temperatures sub-2 nm particles are not able to catalyse hydrogen abstraction from the cyclohexene and metallic Au particles larger than 2 nm are the active sites associated with the observed catalytic activity. Such a size effect is opposite to that discovered for oxidation reactions where O_2 activation is involved, *e.g.* styrene oxidation, for which either sub-2 nm particles[31, 191] or large, positively charged particles[168] were suggested as the active sites.

4.4. Conclusions

In summary, we have established relationship between the size of supported gold nanoparticles and their activity in solvent-free aerobic oxidation of cyclohexene by employing gradually changing catalysts. We showed that phosphine-stabilized gold clusters and phosphine-free Au particles smaller than 2 nm are inactive in this reaction, and that catalytic activity appears only upon formation of sufficient number of metallic particles larger than 2 nm. Further increase in Au particle size results in gradual decrease in catalytic activity, which correlates with the reduction of the Au surface area. The size-dependency observed in this study is in agreement with the suggested mechanism of substrate activation through the abstraction of hydrogen catalysed by metallic gold nanoparticles.

The results of this Chapter were published in B. G. Donoeva, D. S. Ovoshchnikov and V. B. Golovko, *ACS Catalysis*, 2013, 2986-2991. Selected material was adapted with permission.

Chapter 5 - Oxidation of Amines to nitriles photocatalysed by supported hydrous ruthenium oxide

Discussions and formulation of ideas and experiments of this Chapter were done in collaboration with Baira Donoeva.

5.1. Introduction

Nitriles are important compounds used as intermediates for the production of agricultural chemicals, dyes, polymers and fine chemicals.[195, 196] Additionally, compounds containing cyano group are used as pharmaceuticals[197] and functional materials.[198] Traditional methods of the synthesis of nitriles (Figure 5.1), such as *via* Sandmeyer reaction[199] or ammoxidation,[196] either generate excessive waste or require high temperatures (up to 550 ºC).

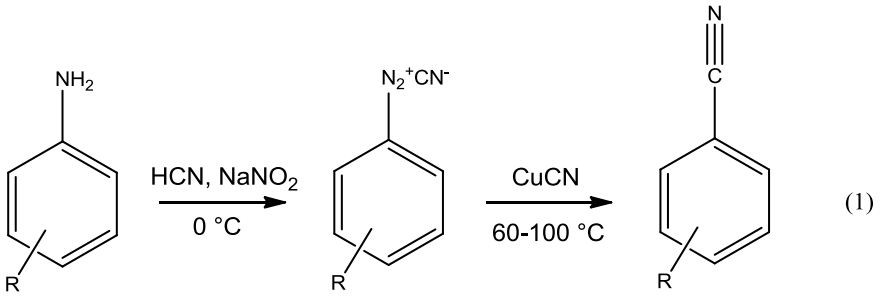

Figure 5.1 Traditional synthesis of nitriles: Sandmeyer reaction (1) and production of acrylonitrile from propene *via* ammoxidation (2).

Alternative pathways that are currently being developed include transformations of amides,[200] aldoximes,[201] alcohols[202] and amines.[203-207] In particular, supported hydrated ruthenium oxide was shown as an effective catalyst for the aerobic oxidation of amines into nitriles at high temperature.[203-206] The catalytic properties of hydrous RuO_2 supported on alumina were first demonstrated in the aerobic oxidation of alcohols[208] and then this catalyst was shown to be very efficient in highly selective conversion of amines to nitriles.[203, 204] After alumina, various other materials were used as supports for hydrous RuO_2, including Co_3O_4[206] and Fe_3O_4,[205] with the latter allowing the catalyst to be magnetically separated. Recently, the oxidation of ethylamine over ruthenium oxide supported on alumina was shown as an alternative pathway for production of acetonitrile.[209]

On the other hand, both ruthenium oxide and hydrous ruthenium oxide are also known for their metallic conductivity[210] and thus can be combined with semiconductors to form photocatalytic systems.[211, 212] For example, anhydrous ruthenium oxide deposited on TiO_2 was shown to be active in water splitting,[213, 214] methanol oxidation[215] and dye degradation.[211]

Recently, visible light driven conversion of amines to imines with high selectivity has been performed using TiO_2,[216, 217] Nb_2O_5,[109] Ag/AgI supported on titanate nanotubes,[218] Au-Pd/ZrO_2[124] and Au/TiO_2 photocatalysts[126] (Figure 5.2). In this Chapter we show that hydrous ruthenium oxide supported on P25 TiO_2 ($RuO_2 \cdot xH_2O/TiO_2$) efficiently catalyses the aerobic oxidation of amines to nitriles under visible light irradiation and ambient conditions.

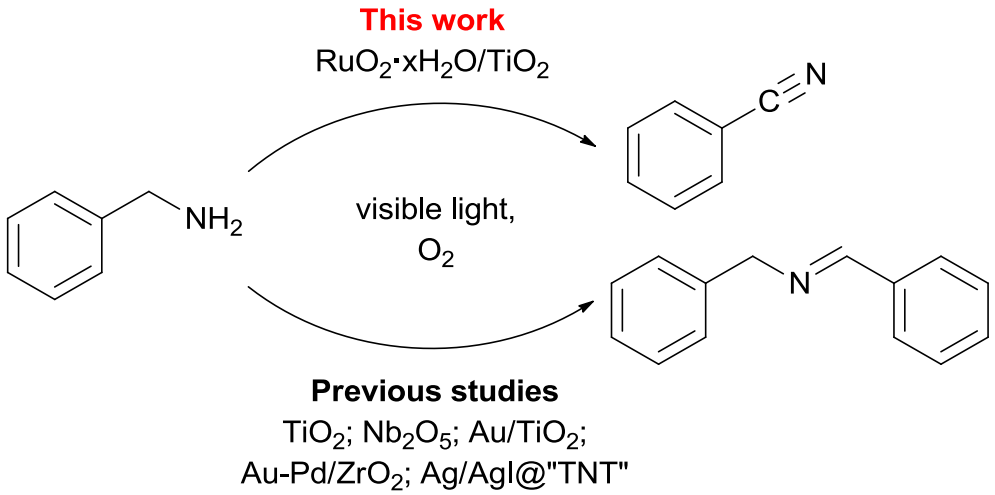

Figure 5.2 Photocatalytic oxidation of benzylamine under irradiation with visible light.

5.2. Experimental procedures

5.2.1. Materials

Benzylamine (>99%), 4-methoxybenzylamine (98%), 4-methylbenzylamine (99%), 4-fluorobenzylamine (AR), 4-chlorobenzylamine (AR), 2-methylbenzylamine (96%), 1-pentylamine (97%), 1-octylamine (96%), dibenzylamine (97%), N-benzylidenebenzylamine (99%), benzonitrile (>97%), 4-methoxybenzonitrile (99%), *p*-tolunitrile (98%), 4-fluorobenzonitrile (99%), 4-chlorobenzonitrile (99%), *o*-tolunitrile (AR), dioxane (AR), lithium aluminium deuteride (98 atom % D, 90%), *tert*-butanol (99%), ammonium oxalate (99%), sodium azide (AR) and 2,2,6,6-tetramethyl-piperidin-1-yl)oxyl (TEMPO, 98%), acetonitrile (AR) were purchased from Aldrich, Riedel de Haen, Hopkin & Williams Ltd and British Drug House and were used as received, except for 4-fluorobenzylamine, 4-chlorobenzylamine and *o*-tolunitrile, which were additionally purified by vacuum distillation. $RuCl_3 \cdot xH_2O$ was purchased from Precious Metals Online.

$PhCD_2NH_2$ was synthesized following the procedure reported by Sun *et al.*[219] Lithium aluminium deuteride (395 mg, 9.5 mmol) was slowly added to benzonitrile (876 mg, 8.5 mmol) dissolved in ice cooled THF (5 mL, anhydrous). The mixture was refluxed overnight. After cooling on ice, diethyl ether (5 mL), H_2O (5 mL), and 15% (w/v) NaOH (1 mL) were added successively, resulting in the formation of precipitate. The solid was removed by filtration and the products were extracted from liquid with diethyl ether (3 × 15 mL) and purified by vacuum distillation. NMR (400 MHz; $CDCl_3$) 7.2-7.3 ppm (5H, m, C_6H_5), 1.5 ppm (2H, s, NH_2), which is consistent with literature data.[220]

5.2.2. Catalyst synthesis

Deposition of ruthenium oxide species onto P25 TiO_2 was conducted following slightly modified procedure previously employed for the preparation of supported ruthenium oxide catalysts.[206, 208, 209] A solution of $RuCl_3 \cdot xH_2O$ (6.5 mg) in deionized (Milli-Q) water (2 mL) was slowly added drop-wise to TiO_2 (250 mg, Evonik P25) dispersed in deionized water (5 mL). Solution of NaOH (150 mg) in deionized water (5 mL) was added drop-wise and the mixture was left stirring for 30 min. The solid was recovered by centrifugation, washed twice with deionized water (15 mL) and, in order to facilitate drying, with ethanol (15 mL), followed by diethyl ether (15 mL). The catalyst was dried under vacuum at room temperature and then calcined for 30 min in a convection oven preheated to 150 ºC. Before each catalytic reaction, portions of the catalyst were additionally calcined under the same conditions for 15 min.

5.2.3. Catalyst characterisation

The ruthenium content in the catalyst was established by ICP-MS. A sample of the catalyst was treated with a mixture of HCl and HNO_3 (6:1, v/v)[221] at 80 ºC

overnight, the solid was removed by centrifugation and the liquid, together with washings, was transferred to a volumetric flask and topped up with Milli-Q water. The ruthenium loading was established using ICP-MS (Agilent 7500 cx) and was found to be 0.8 wt%.

The chemical state of the ruthenium was established using XPS; in particular the position of $Ru3d_{5/2}$ peak was analysed. The XPS study was conducted using a Kratos Axis DLD spectrometer with a monochromated Al Kα X-ray source by Dr Colin Doyle from RCSMS, University of Auckland. A supply of low-energy electrons was used for charge neutralization. A survey spectrum was recorded with a pass energy of 80 eV. Binding energies were normalized with respect to the position of the adventitious carbon C1s peak at 285.0 eV. Hydrous ruthenium oxide is known to have a $Ru3d_{5/2}$ binding energy shifted to higher energy (*ca.* 281.4 eV) compared with anhydrous RuO_2 (280.7 eV) due to the presence of OH groups.[222] The $Ru3d_{5/2}$ peak position for the $RuO_2 \cdot xH_2O/TiO_2$ catalyst was found to be 281.4 eV (Figure 5.3), which indicates that hydrous ruthenium oxide was deposited onto the TiO_2 surface. The survey spectrum showed no Cl peaks, indicating complete conversion of $RuCl_3$ to hydrous RuO_2.

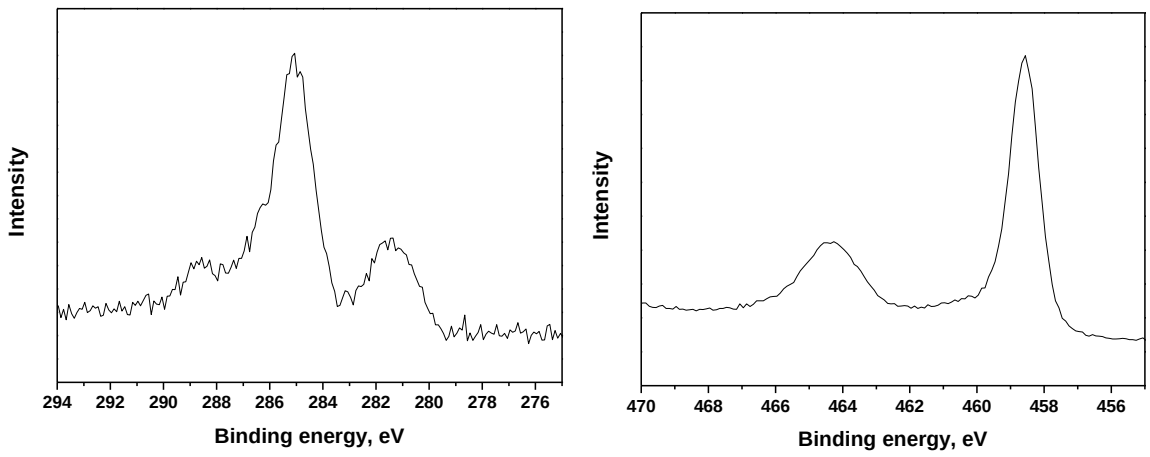

Figure 5.3 XPS spectra of $RuO_2 \cdot xH_2O/TiO_2$: Ru 3d (left) and Ti 2p (right).

A diffuse-reflectance UV-Vis spectrum was recorded using the Citra 4040 spectrometer equipped with an integrating sphere and operating in reflectance mode. The catalyst samples were diluted with $BaSO_4$ (sample:$BaSO_4$ 20:80, wt%:wt%), the resulting mixture was uniformly mixed, ground and hand-pressed into the sample-holder. UV-vis spectra were recorded in reflectance mode and obtained reflectance values (R) were transformed to the Kubelka-Munk function F(R) according to the formula:

$$F(R) = \frac{(1-R)^2}{2R}$$

The spectra were plotted in coordinates of F(R) vs λ. In contrast to TiO_2 (base-treated), which absorbs only in UV region, the $RuO_2{\cdot}xH_2O/TiO_2$ catalyst showed a continuous absorption across the whole visible range, with a pronounced band centred at *ca.* 450 nm (Figure 5.4). The absorption of light by RuO_2 in the visible range is due to the combination of interband transitions and localised surface plasmon resonance.[132]

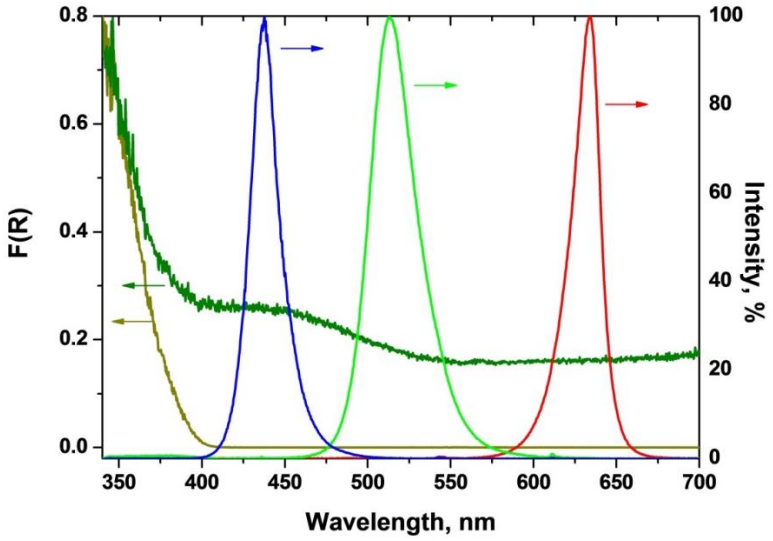

Figure 5.4 Diffuse reflectance spectra of $RuO_2 \cdot xH_2O/TiO_2$ (dark green) and base-treated P25 TiO_2 (brown). Normalised emission spectra of blue, green and red LEDs.

5.2.4. Catalyst testing

The photocatalytic oxidation of amines was performed in toluene at 30 ± 1 ºC under ~1 atm of O_2. Amine (0.1 mmol), solvent (3 mL) and n-decane (internal standard for GC-FID analysis, 10 µL) were mixed together with 50 mg of catalyst (4 mol% Ru) in a Pyrex glass two-necked round-bottom flask equipped with a reflux condenser. The system was flushed with O_2 three times and connected to a rubber balloon filled with O_2. The reactor was placed in a beaker filled with deionized water and the temperature was maintained using a hotplate stirrer. The mixture was irradiated using a single 50 W LED. Three different LEDs were employed in this work: blue (intensity maximum at 440 nm, Figure 5.4), green (513 nm) and red (634 nm). The distances between the reactor and different LEDs were adjusted to obtain the same 1.5 W/cm^2 intensity of the light supplied to the reaction. The intensity of the light produced by LEDs was measured using a silicon detector PDA36A (Thorlabs) connected to an oscilloscope. The spectra of LEDs were obtained using a USB 200-VIS-NIR spectrometer (Ocean optics).

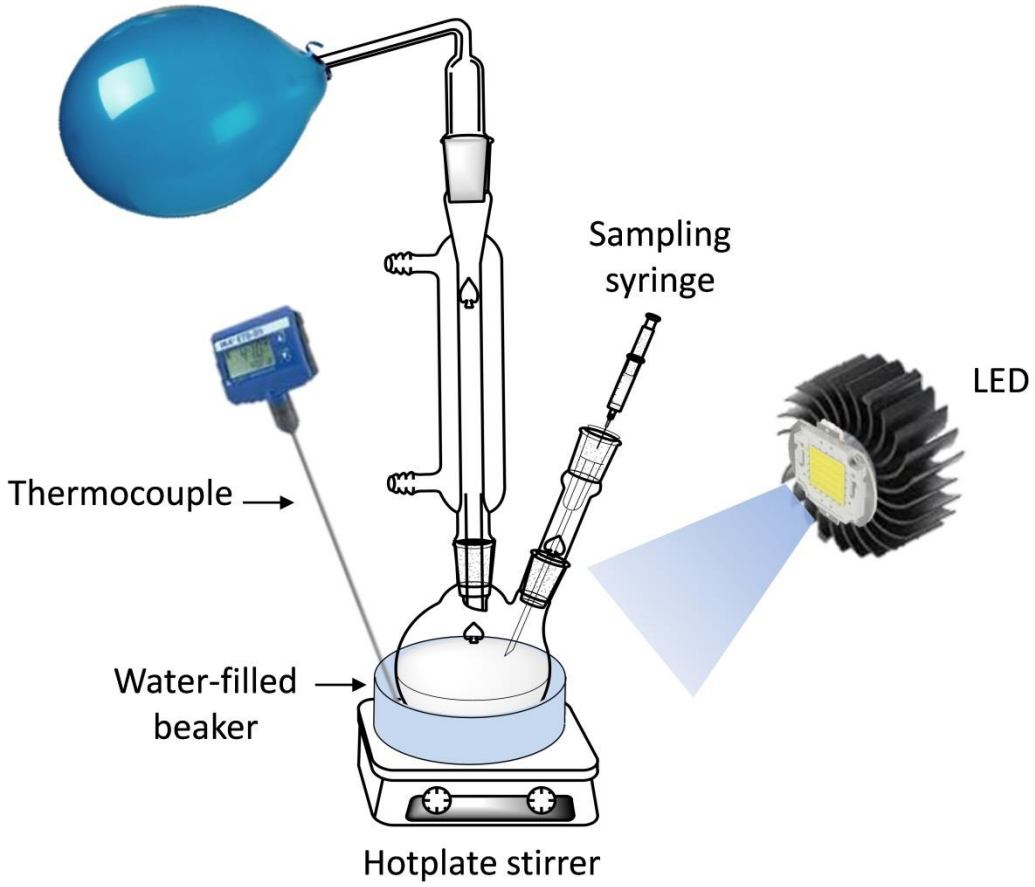

Figure 5.5 Schematic representation of catalytic setup.

Samples of the reaction mixture were taken using a glass syringe (using the same method as described in Chapter 4), separated from the solid catalyst by centrifugation and analysed by GC-FID using a Shimadzu GC-2010 instrument equipped with an Rtx-50 capillary column (30 m × 0.25 mm × 0.25 μm). The products of amine oxidation were identified by GC-mass spectrometry (Shimadzu GCMS-QP2010) and quantified using solutions of reference compounds with known concentrations. A typical chromatogram is shown in Figure 5.6.

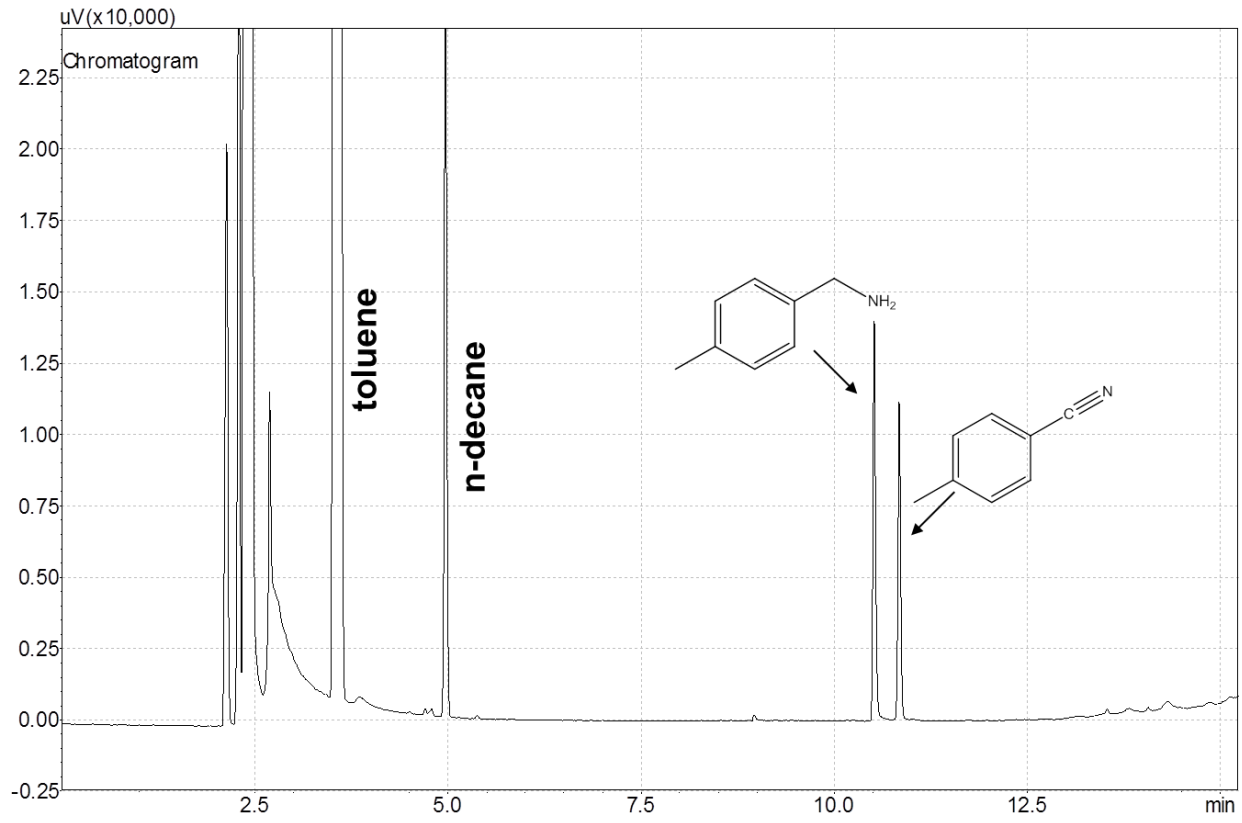

Figure 5.6 Chromatogram of reaction mixture sampled from the reaction of oxidation of 4-methylbenzylamine in toluene.

The photocatalytic oxidation of amines in water was performed in a similar manner, except dioxane (10 µL) was used as an internal standard instead of n-decane. At the end of each reaction, acetonitrile (9 mL) was added to the reaction mixture. An aliquot of the thoroughly stirred resulting mixture was further diluted with acetonitrile (1:3 v/v), dried over anhydrous $MgSO_4$ and analysed using GC-FID.

The photocatalytic aerobic oxidation of benzylamine using the Sun as a light source was conducted in toluene at 30 ± 3 ºC. Benzylamine (0.1 mmol), toluene (3 mL) and n-decane (10 µL) were mixed together with 50 mg of catalyst (4 mol% Ru) in a Pyrex-glass 2-necked round-bottom flask. The system was flushed with O_2 three times and connected to a rubber balloon filled with O_2. The reactor was placed in a

beaker filled with deionized water and the temperature of the system was maintained at 30 ± 3 ºC. The catalytic setup was placed by the open window of the laboratory (latitude 43º31' south, longitude 172º34' east) so that the reactor would be directly irradiated by the Sun for the duration of the experiment (6 h). Samples of the reaction mixture were taken using a glass syringe and analysed using GC-FID.

5.3. Results and discussion

The rate of aerobic benzylamine oxidation in the presence of $RuO_2 \cdot xH_2O/TiO_2$ was found to be significantly affected by visible light irradiation, with the degree of acceleration of the reaction rate depending on the wavelength of light. The highest rate of amine oxidation was achieved under irradiation with a blue LED (440 nm), with the yield of benzonitrile reaching 92% in 4 h. The catalyst was less active under irradiation with green (513 nm) or red (634 nm) light, with the yield of benzonitrile being 64% and 26%, respectively. Aerobic benzylamine oxidation performed in the absence of light showed conversion of only 12% in 4 h. In all cases the reaction selectivity towards benzonitrile was high and exceeded 93%.

A plot of $\ln(C_0/C)$ as a function of time gives a straight line indicating that the amine oxidation exhibits a pseudo-first-order kinetics (Figure 5.7). The rate constant of the reaction is obtained from the slope of the line.

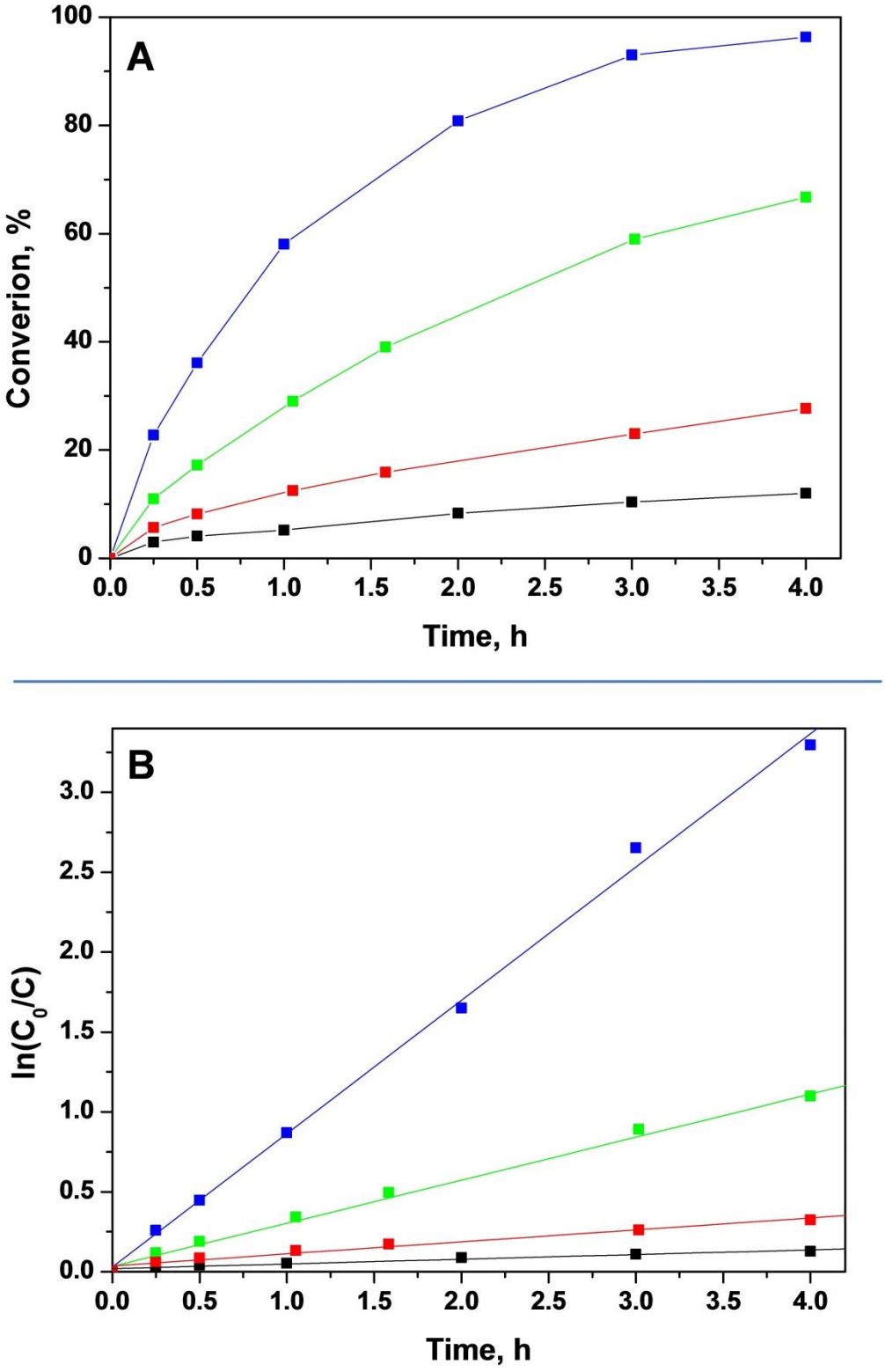

Figure 5.7 Kinetics of aerobic oxidation of benzylamine (A) and corresponding $\ln(C_0/C)$ *vs.* time linear plot (B). Reaction performed under irradiation with blue (■), green (■) or red (■) light or in the absence of light (■)

Based on these data, the turnover frequency could be calculated according to the following equation:

$$TOF_{Ru} = \frac{W_i}{C_{Ru}} = \frac{k \cdot C_{amine}}{C_{Ru}} = \frac{k \cdot n_{amine}}{n_{Ru}}$$

where W_i – initial reaction rate, k – rate constant, n_{amine} – number of moles of amine, n_{Ru} – number of moles of ruthenium. Rate constants and TOF_{Ru} calculated for the benzylamine oxidation under irradiation with various types of LEDs are summarised in Table 5.1.

Table 5.1 Photocatalytic oxidation of benzylamine[a]

Catalyst	Light	Product	Conversion /Yield,[b] %	k, h^{-1}	TOF_{Ru}, h^{-1}
$RuO_2 \cdot xH_2O$/ TiO_2	Blue	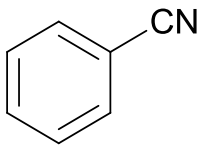	98/92	0.85	21.4
	Green		67/64	0.27	7.0
	Red		28/26	0.07	1.9
	–		12/11	0.03	0.7
P25 TiO_2 base treated	Blue	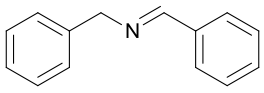	96/84	-	-
	Green		8/6	-	-
	Red		4/3	-	-
	–		3/2	-	-

[a] Reaction conditions: benzylamine (0.1 mmol), O_2 (~1 atm), toluene (3 mL), catalyst 50 mg (4 mol% Ru), irradiance 1.5 W/cm^2, 30 ºC, 4 h. [b] Determined by GC

To adequately compare the catalytic performance of $RuO_2 \cdot xH_2O/TiO_2$ with that of P25 TiO_2, the latter was also subjected to the conditions of the catalyst synthesis (NaOH treatment and calcination at 150 ºC). The catalyst thus obtained is denoted as P25 TiO_2 base treated. P25 TiO_2 base treated was found to be also active in

the oxidation of benzylamine under visible light irradiation. However, *N*-benzylidenebenzilamine was formed instead of benzonitrile (Table 5.1), which is consistent with previous reports.[216] As expected, TiO_2 was only active under irradiation with blue light, while almost no conversion was observed under either green or red light irradiation.

Photocatalytic oxidation was further extended to various amines. Table 5.2 summarises the results of aerobic amine oxidation catalysed by $RuO_2 \cdot xH_2O/TiO_2$ under irradiation with blue light. Good to excellent yields were obtained for the oxidation of both benzylic and primary aliphatic amines. *Para*- and *ortho*-substituted benzylic amines were oxidised to corresponding nitriles with selectivity ranging from 83% to 98%.

Table 5.2 Photocatalytic oxidation of amines[a]

N	Substrate	Product	Time, h	Light	Conversion,[b] %	Yield,[b] %	TOF_{Ru},[c] h^{-1}
1	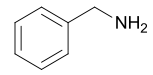	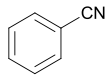	4	+	98	92	21.4
				–	12	11	-
2	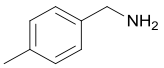	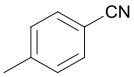	4	+	98	84	25.4
				–	13	9	-
3	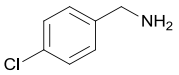	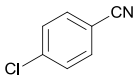	4	+	95	79	19.6
				–	12	6	-
4	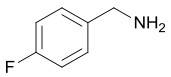	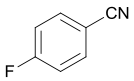	4	+	93	77	16.4
				–	12	6	-
5	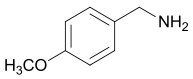	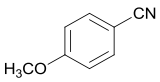	4	+	95	86	18.8
				–	12	9	-
6	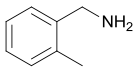	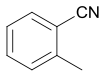	4	+	99	97	23.2
				–	14	9	-
7	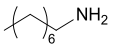	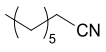	10	+	99	72	11.4
				–	12	8	-
8	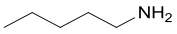	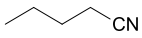	7	+	99	81	12.9
				–	18	13	-
9	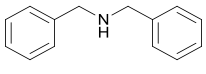	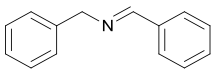	27	+	92	16[d]	3.5
10[e]	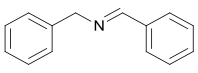	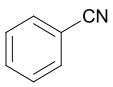	3	+	93	41[f]	21.2

[a]Reaction conditions: benzylamine (0.1 mmol), O_2 (~1 atm), toluene (3 mL), catalyst 50 mg (4 mol% Ru), blue LED, irradiance 1.5 W/cm^2, 30 °C. [b]Determined by GC. [c]Calculated from the initial reaction rates. [d]Other products: benzaldehyde (yield 42%) and benzonitrile (yield 22%). [e]N-BBA (0.05 mmol). [f]Other product: benzaldehyde (51%).

An investigation of the changes in the reaction rate of the oxidation of substituted benzylic compounds, such as amines studied here, can give an insight into the mechanism of the reaction. For *para*- and *meta*-XC_6H_4Y, where X is a substituent and Y is a site of reaction, Hammett[223] proposed the following equation:

$$\log\left(\frac{k_X}{k_H}\right) = \sigma\rho$$

where k_H is the rate constant or equilibrium constant for X = H, k_X is the constant for the group X, ρ is a constant for a given reaction under given set of conditions and σ is a constant characteristic that sums up the total electrical effects of the group X when attached to a benzene ring. The value of ρ is set to 1.0 for the ionization of substituted benzoic acids in water at 25 ºC. The values of σ were then calculated for each group. [224] A positive value of σ indicates an electron-withdrawing group and a negative value – an electron-donating one. The constant ρ measures the susceptibility of the reaction to electrical effects; reactions with positive ρ indicate negative charge build-up in the transition state and are accelerated by electron-withdrawing groups and *vice versa*.[225] The kinetics of the oxidation of *para*-substituted benzylamines and corresponding plots of $\ln(C_0/C)$ *vs.* time are shown in Figure 5.8.

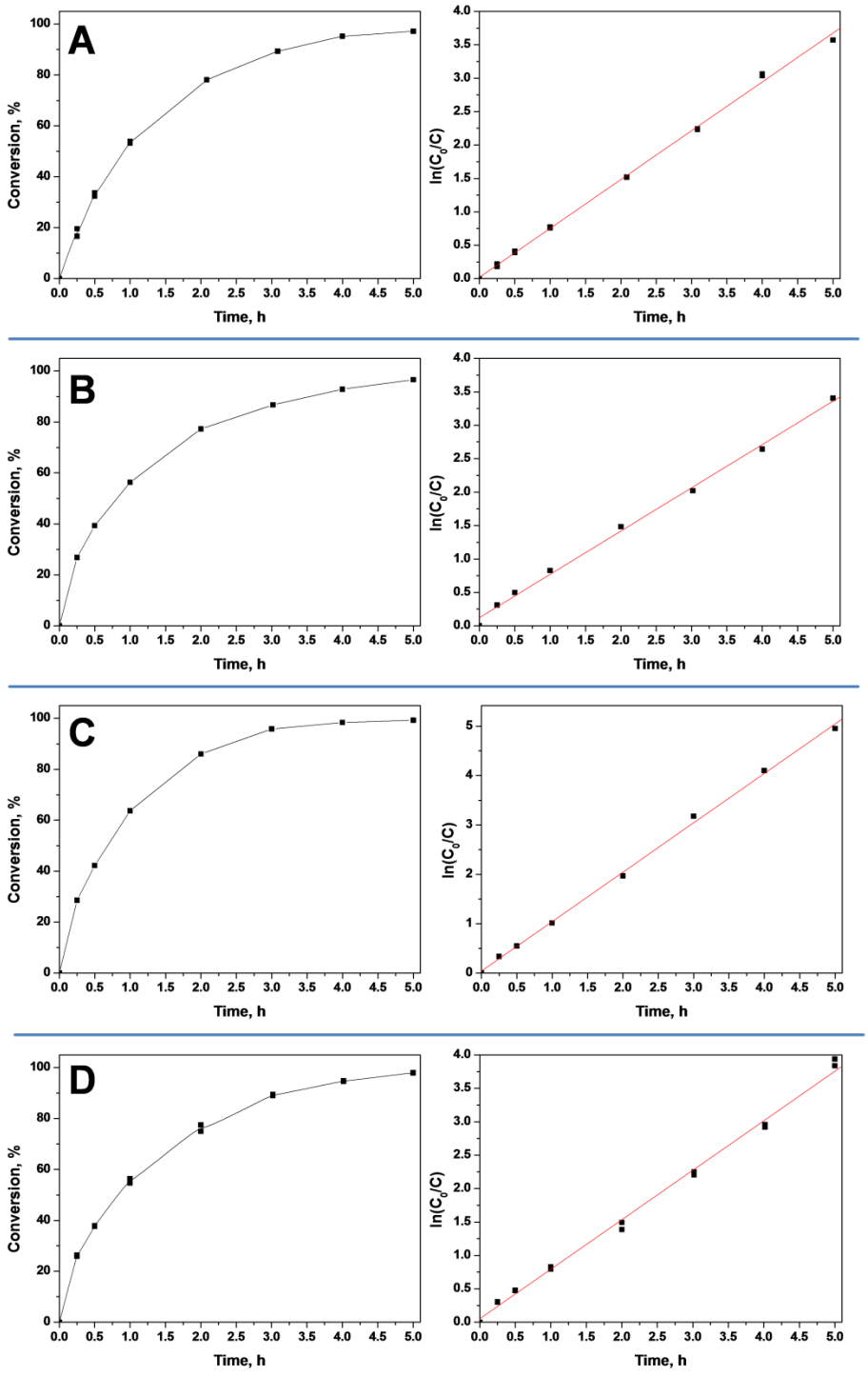

Figure 5.8 Kinetics of aerobic oxidation of substituted benzylamines (left) and corresponding plot of $\ln(C_0/C)$ *vs.* time (right): 4-Cl (A), 4-F (B), 4-CH_3 (C) and 4-CH_3O (D).

The rate constants of the oxidation of substituted benzylamines obtained from the plot of $\ln(C_0/C)$ as a function of time were used to obtain Hammett plot (Figure 5.9). The slope of the linear plot gave the value of parameter ρ close to zero, indicating that the reaction is not sensitive to substituents and that electronic perturbation is unlikely to occur in the C-H activation step.

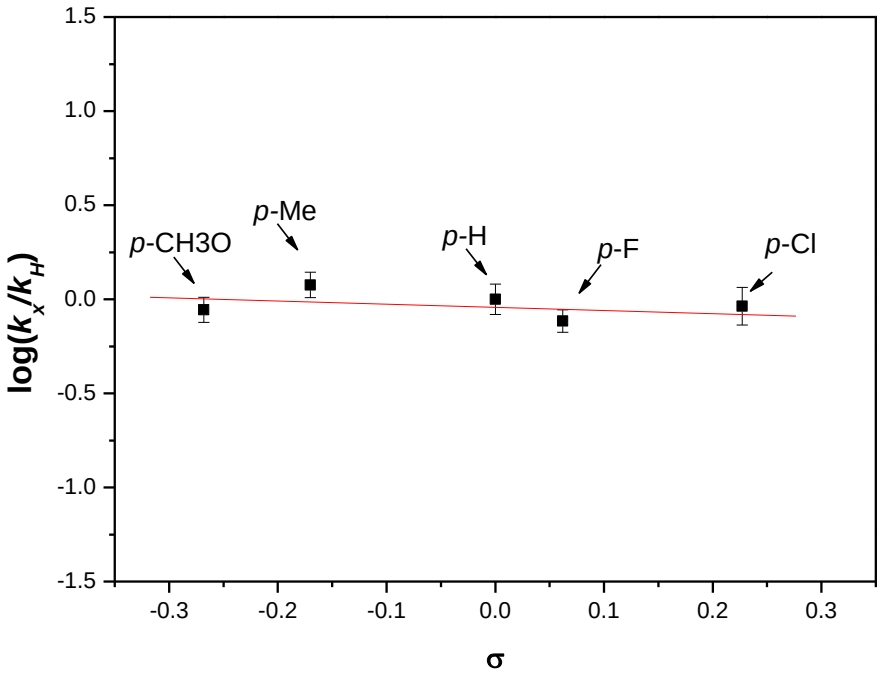

Figure 5.9 Hammett plot for the aerobic oxidation of substituted benzylamines.

The rate of oxidation of primary aliphatic amines was lower than that of benzylic amines, with conversion of pentylamine and octylamine reaching 99% in 7 h and 10 h, respectively. Kinetic curves of the oxidation of aliphatic amines are shown in Figure 5.10.

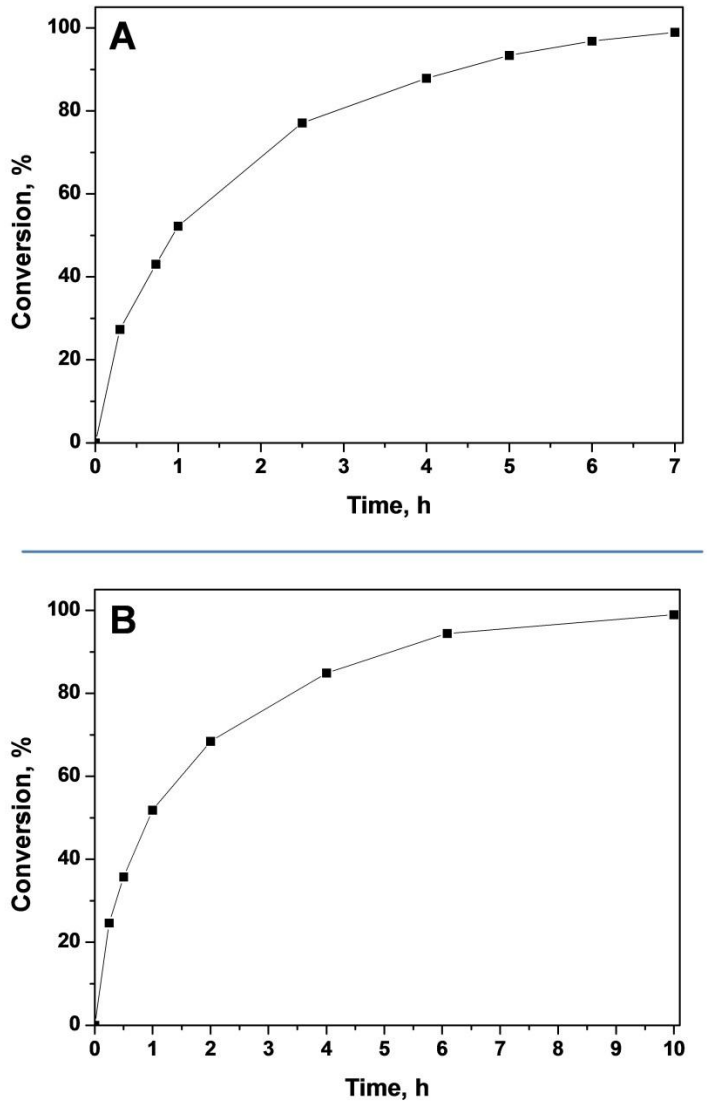

Figure 5.10 Kinetics of oxidation of pentylamine (A) and octylamine (B).

Interestingly, photocatalytic oxidation of dibenzylamine showed much lower selectivity towards *N*-benzylidenebenzylamine than the thermal reaction reported by Yamaguchi and Mizuno (17% *vs.* 84%),[208] with higher yields of benzaldehyde and benzonitrile (entry 9, Table 5.2). This can be explained by the fact that under visible light irradiation $RuO_2 \cdot xH_2O/TiO_2$ can promote oxidation of *N*-benzylidene-benzylamine to benzaldehyde and benzonitrile (entry 10, Table 5.2).

The kinetic isotope effect was examined by comparison of the kinetics of oxidation of benzyl-α-α-D_2-amine and benzylamine. A small value of the ratio of rate constants k_H/k_D = 1.3 ± 0.1 indicates that the cleavage of C-H bond is not involved in the rate-determining step, similarly to the oxidation of benzylic amines to imines photocatalysed by TiO_2 (k_H/k_D = 1.3).[216]

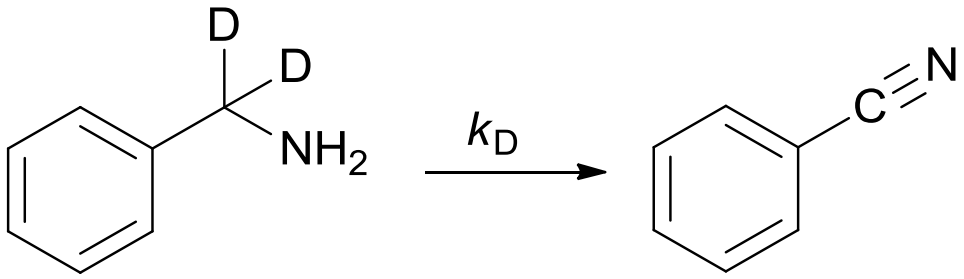

The catalyst $RuO_2 \cdot xH_2O/TiO_2$ is also capable of promoting amine oxidation under sunlight irradiation at near-ambient temperature (30 ± 3 ºC). The catalytic setup was placed by an open window so that the reactor would be directly irradiated by the Sun for the duration of the experiment of 6 h. The yield of benzonitrile reached 46% with TOF_{Ru} of 5.2 h^{-1}. The kinetics of benzylamine oxidation is shown in Figure 5.11.

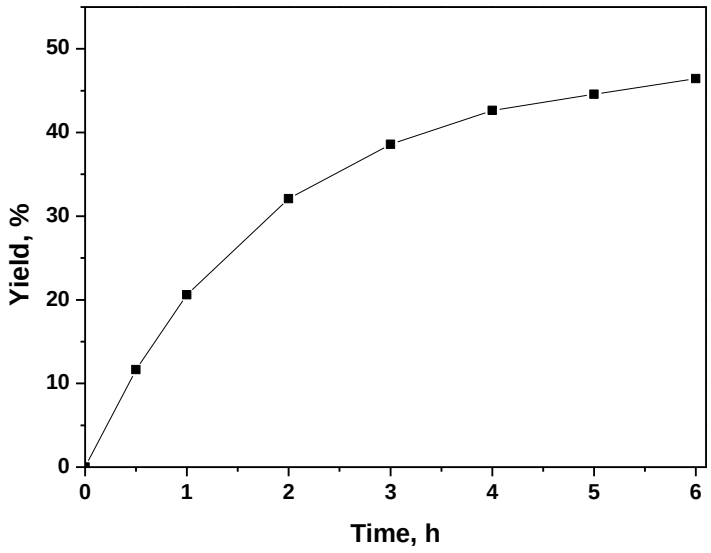

Figure 5.11 Kinetics of benzylamine oxidation under sunlight irradiation.

Water is the solvent of choice for conducting green chemical processes.[226] However, poor selectivity of photocatalytic processes utilizing water as a solvent could be expected in some cases due to the generation of active oxygen species from the oxidation of H_2O.[227] For example, lower selectivity was reported for the TiO_2-catalysed oxidation of amines in water compared to that in CH_3CN.[217] In order to test the applicability of water as a solvent in our system, we have conducted aerobic oxidation of benzylamine and pentylamine in water in the presence of $RuO_2 \cdot xH_2O/TiO_2$ under irradiation with the blue LED. Oxidation of both amines gave corresponding nitriles in good yields: the yield of benzonitrile reached 90% after 4 h, while the yield of valeronitrile was 94% after 7 h. These results show that water could be efficiently used as a solvent for the aerobic oxidation of both benzylic and primary aliphatic amines using $RuO_2 \cdot xH_2O/TiO_2$ catalyst.

In order to better understand the mechanism of photocatalytic amine oxidation in water, we have performed a series of experiments with the addition of different radical scavengers (Figure 5.12). Oxidation of benzylamine in the presence of ammonium oxalate (hole scavenger)[228-231] gave only 9% of benzonitrile, indicating the involvement of holes in the photocatalytic amine oxidation. Addition of $^{\bullet}OH$ radical scavenger *tert*-butanol[232-234] did not affect benzylamine oxidation, implying that such species are not involved in the process. The presence of either TEMPO ($^{\bullet}O_2^-$ radical scavenger)[235, 236] or NaN_3 (scavenger of singlet oxygen, $^1O_2$)[237-239] led to decreases of benzonitrile yield to 82% and 36%, respectively, indicating the involvement of both $^{\bullet}O_2^-$ and $^1O_2$, with singlet oxygen being the predominant active species.

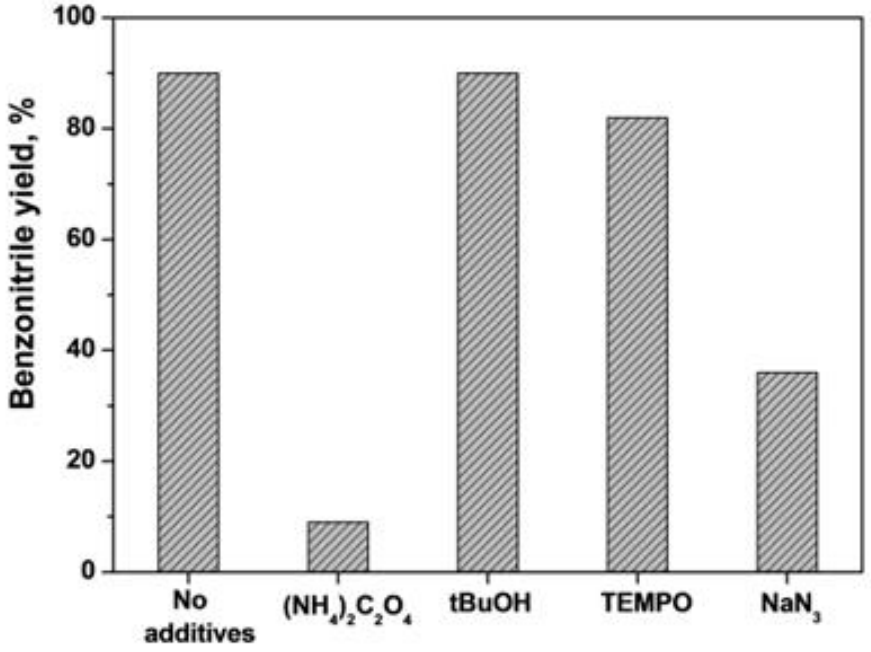

Figure 5.12 Effect of the addition of various radical scavengers on the oxidation of benzylamine. Reaction conditions: benzylamine (0.1 mmol), scavenger (0.1 mmol), water (3 mL), O_2 (~1 atm), $RuO_2 \cdot xH_2O/TiO_2$ (50 mg), blue LED 1.5 W/cm^2, 4 h.

Based on these results, two possible mechanisms (or their combination) for the photocatalysed oxidation of amines could be suggested. In the first mechanism (Figure 5.13A), incident photons are adsorbed by hydrous ruthenium oxide through interband transition[132] and/or the localised surface plasmon resonance (1),[212] the photoexcited electrons are transferred into the TiO_2 conduction band (2), with subsequent formation of superoxide radicals $^{\bullet}O_2^-$ (3); the holes remaining in $RuO_2 \cdot xH_2O$ oxidise $^{\bullet}O_2^-$ to form singlet oxygen[240-242] (4) and, finally, $RuO_2 \cdot xH_2O$ catalyses the oxidation of amines to nitriles with $^1O_2$ (5). Additionally, the holes can oxidise amines, in which case the superoxide radical would be directly involved in the oxidation process. Alternatively, singlet oxygen could be generated *via* the photoexcitation of Ti^{III} centres (trapped electrons) with subsequent energy transfer towards the formation of $^1O_2$ (Figure 5.13B).[243] In this mechanism, photogenerated holes in $RuO_2 \cdot xH_2O$ are not

consumed for the generation of $^1O_2$ and can directly oxidise amines. This mechanism could explain low dependence of the process on the superoxide radical (Figure 5.12).

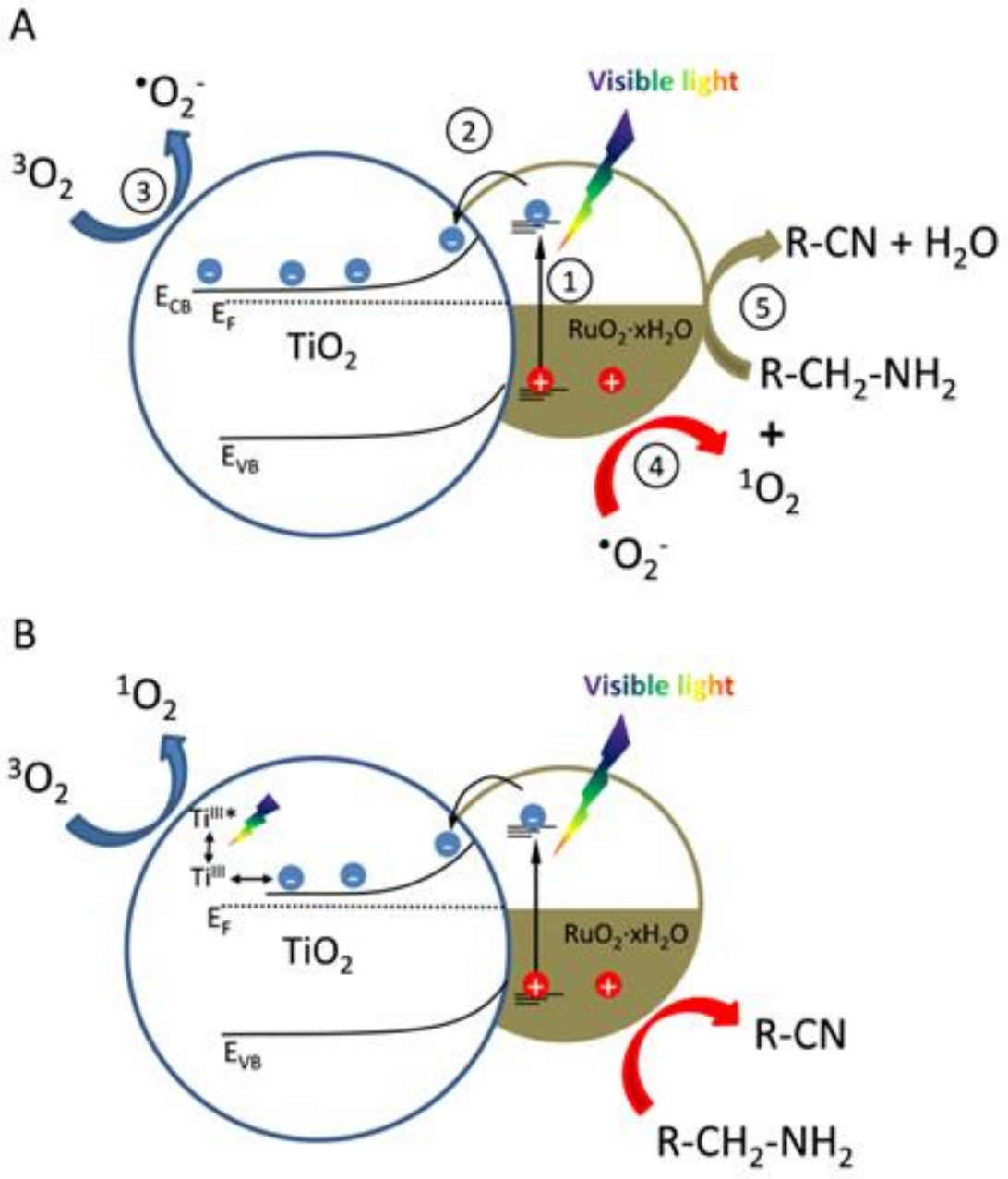

Figure 5.13 Schematic diagram of possible mechanisms of amine oxidation upon visible light irradiation in water: (A) oxidation of amines by singlet oxygen, (B) amine oxidation by photogenerated holes.

The involvement of such active species as singlet oxygen and holes could be the reason for further oxidation of N-benzylidene-benzylamine in the photocatalytic process observed here, which did not occur in the reported earlier thermally activated process (*vide supra*).

5.4. Conclusions

In this Chapter we have shown that hydrous ruthenium oxide supported on TiO_2 can be employed as a highly selective photocatalyst under visible light irradiation driving the aerobic oxidation of a wide range of amines, including benzylic and aliphatic, to the corresponding nitriles. It was found that irradiation with light of various wavelengths accelerates the oxidation to different degrees. The reaction is accelerated more efficiently under irradiation with light of shorter wavelength. Amine oxidation can also be driven by sunlight at ambient temperature. Importantly, water can be used as a solvent for the oxidation of both benzylic and aliphatic amines without significant loss in activity and selectivity. The reaction mechanism was investigated by performing a series of experiments, including comparison of the reaction rates of oxidation of *para*-substituted benzylamines, deuterated benzylamine and conducting benzylamine oxidation in the presence of various scavengers. We have found that photocatalysed amine oxidation is insensitive to the substituents; singlet oxygen and photogenerated holes were identified as predominant active species.

Conclusions

In the first part of this work (Chapters 3 and 4) sub-2 nm phosphine-stabilised gold clusters were employed as precursors to supported gold catalysts. The study of their catalytic behaviour was performed in the solvent-free aerobic oxidation of cyclohexene. It was found that under the conditions of this catalytic reaction, gold clusters lose their phosphine shell and sinter into nanoparticles with mean diameters ranging from 4 to *ca.* 10 nm, with the size of the formed nanoparticles depending on the type of the cluster and gold loading. Detailed kinetic investigations demonstrated that the nanoparticles formed from gold clusters are actually the active sites of the reaction, while gold entities smaller than 2 nm are inactive in cyclohexene oxidation.

The gold in aerobic cyclohexene oxidation was suggested to promote the formation of cyclohexenyl hydroperoxide. The latter can be converted to other products in the presence of different heterogeneous co-catalysts. Cyclohexene oxide can be formed *via* the reaction of cyclohexenyl hydroperoxide with cyclohexene catalysed by WO_3, either present as a support or introduced to the reaction as a co-catalyst physically admixed with silica-supported gold catalyst. Alternatively, 2-cyclohexen-1-one can be formed when metal-organic framework MIL-101 is used as a co-catalyst for SiO_2-based gold catalyst. Additionally, it was shown that the nature of catalysis in solvent-free cyclohexene oxidation is truly heterogeneous. In the future, the method of establishing the threshold in size of active gold nanoparticles described in Chapter 4 could be extended to other reactions catalysed by supported gold nanoparticles.

In the second part of this thesis (Chapter 5), the activity of supported hydrous ruthenium oxide as a photocatalyst for aerobic amine oxidation under visible light

irradiation was investigated. It was shown for the first time that hydrous ruthenium oxide supported on TiO_2 is a highly selective photocatalyst for transformation of benzylic and aliphatic amines to corresponding nitriles. The activity of the catalyst increased with shorter wavelengths of the utilized light, with the highest activity obtained when the reaction was conducted under irradiation with blue LED. It was demonstrated that amine oxidation in the presence of the photocatalyst can also be driven by sunlight at ambient temperature. Water can also be used as a solvent for the oxidation of both benzylic and aliphatic amines without significant loss in activity and selectivity. Finally, the reaction mechanism was investigated by performing a series of experiments including comparison of the reaction rates of oxidation of *para*-substituted benzylamines, deuterated benzylamine and conducting benzylamine oxidation in the presence of various scavengers. It was found that photocatalysed amine oxidation is insensitive to the substituents; singlet oxygen and photogenerated holes were identified as predominant active species. The findings of Chapter 5 could serve as a basis for further investigation of photocatalytic properties of supported hydrous RuO_2 in other RuO_2-specific reactions.

References

1. Y. Yu, J. Huang, T. Ishida and M. Haruta, in *Modern Heterogeneous Oxidation Catalysis*, Wiley-VCH Verlag GmbH & Co. KGaA, 2009, pp. 77-124.
2. R. A. Sheldon, I. W. C. E. Arends and U. Hanefeld, in *Green Chemistry and Catalysis*, Wiley-VCH Verlag GmbH & Co. KGaA, 2007, pp. 1-47.
3. P. Serp, K. Philippot and Editors, *Nanomaterials in Catalysis*, Wiley-VCH Verlag GmbH & Co. KGaA, 2013.
4. J. M. Thomas, K. I. Zamaraev and Editors, *Perspectives in Catalysis*, Blackwell, 1992.
5. A. Jess and P. Wasserscheid, *Chemical Technology: An Integral Textbook*, Wiley-VCH Verlag GmbH, 2013.
6. J. R. H. Ross, Elsevier Science, Burlington, 2011.
7. J. Hagen, *Industrial Catalysis: A Practical Approach*, Wiley, 1999.
8. R. B. N. Baig and R. S. Varma, *Chemical Communications*, 2013, **49**, 752-770.
9. J. Falbe and H. Bahrmann, *Chemie in unserer Zeit*, 1981, **15**, 37-45.
10. G. A. Somorjai and M. Yang, *Topics in Catalysis*, 2003, **24**, 61-72.
11. H. Liu, T. Jiang, B. Han, S. Liang and Y. Zhou, *Science (Washington, DC, U. S.)*, 2009, **326**, 1250-1252.
12. G. Schmid, N. Klein, B. Morun, A. Lehnert and J. O. Malm, *Pure and Applied Chemistry*, 1990, **62**, 1175-1177.
13. C. Della Pina, E. Falletta, L. Prati and M. Rossi, *Chemical Society Reviews*, 2008, **37**, 2077-2095.
14. G. C. Bond, P. A. Sermon, G. Webb, D. A. Buchanan and P. B. Wells, *Journal of the Chemical Society, Chemical Communications*, 1973, 444b-445.
15. M. Haruta, T. Kobayashi, H. Sano and N. Yamada, *Chemistry Letters*, 1987, 405-408.
16. G. J. Hutchings, *Journal of Catalysis*, 1985, **96**, 292-295.
17. A. S. K. Hashmi and G. J. Hutchings, *Angewandte Chemie International Edition*, 2006, **45**, 7896-7936.
18. A. Corma and H. Garcia, *Chemical Society Reviews*, 2008, **37**, 2096-2126.

19. K. Weissermel and H.-J. Arpe, in *Industrial Organic Chemistry*, Wiley-VCH Verlag GmbH, 2008, pp. 267-312.
20. D. Thompson, *Gold Bulletin*, 1998, **31**, 111-118.
21. B. Taylor, J. Lauterbach and W. N. Delgass, *Applied Catalysis A: General*, 2005, **291**, 188-198.
22. L. Cumaranatunge and W. N. Delgass, *Journal of Catalysis*, 2005, **232**, 38-42.
23. C. Corti, R. Holliday and Editors, *Gold: Science And Applications*, CRC Press, 2010.
24. A. Corma and H. García, *Chemical Reviews*, 2002, **102**, 3837-3892.
25. S. Lee, L. M. Molina, M. J. López, J. A. Alonso, B. Hammer, B. Lee, S. Seifert, R. E. Winans, J. W. Elam, M. J. Pellin and S. Vajda, *Angewandte Chemie International Edition*, 2009, **48**, 1467-1471.
26. M. Ojeda and E. Iglesia, *Chemical Communications*, 2009, 352-354.
27. N. Dimitratos, J. A. Lopez-Sanchez and G. J. Hutchings, *Chemical Science*, 2012, **3**, 20-44.
28. M. D. Hughes, Y.-J. Xu, P. Jenkins, P. McMorn, P. Landon, D. I. Enache, A. F. Carley, G. A. Attard, G. J. Hutchings, F. King, E. H. Stitt, P. Johnston, K. Griffin and C. J. Kiely, *Nature*, 2005, **437**, 1132-1135.
29. C. H. A. Tsang, Y. Liu, Z. Kang, D. D. D. Ma, N.-B. Wong and S.-T. Lee, *Chemical Communications*, 2009, 5829-5831.
30. Z.-Y. Cai, M.-Q. Zhu, J. Chen, Y.-Y. Shen, J. Zhao, Y. Tang and X.-Z. Chen, *Catalysis Communications*, 2010, **12**, 197-201.
31. M. Turner, V. B. Golovko, O. P. H. Vaughan, P. Abdulkin, A. Berenguer-Murcia, M. S. Tikhov, B. F. G. Johnson and R. M. Lambert, *Nature*, 2008, **454**, 981-983.
32. K. Weissermel and H.-J. Arpe, in *Industrial Organic Chemistry*, Wiley-VCH Verlag GmbH, 2008, pp. 239-266.
33. K. Zhu, J. Hu and R. Richards, *Catalysis Letters*, 2005, **100**, 195-199.
34. L. Li, C. Jin, X. Wang, W. Ji, Y. Pan, T. van der Knaap, R. van der Stoel and C. T. Au, *Catalysis Letters*, 2009, **129**, 303-311.
35. Y.-J. Xu, P. Landon, D. Enache, A. Carley, M. W. Roberts and G. Hutchings, *Catalysis Letters*, 2005, **101**, 175-179.
36. L.-X. Xu, C.-H. He, M.-Q. Zhu and S. Fang, *Catalysis Letters*, 2007, **114**, 202-205.

37. B. P. C. Hereijgers and B. M. Weckhuysen, *Journal of Catalysis*, 2010, **270**, 16-25.
38. M. Conte, X. Liu, D. M. Murphy, K. Whiston and G. J. Hutchings, *Physical Chemistry Chemical Physics*, 2012, **14**, 16279-16285.
39. L. Kesavan, R. Tiruvalam, M. H. A. Rahim, M. I. bin Saiman, D. I. Enache, R. L. Jenkins, N. Dimitratos, J. A. Lopez-Sanchez, S. H. Taylor, D. W. Knight, C. J. Kiely and G. J. Hutchings, *Science*, 2011, **331**, 195-199.
40. C. D. Pina, E. Falletta and M. Rossi, *Chemical Society Reviews*, 2012, **41**, 350-369.
41. S. E. Davis, M. S. Ide and R. J. Davis, *Green Chemistry*, 2013, **15**, 17-45.
42. L. Prati and M. Rossi, *Journal of Catalysis*, 1998, **176**, 552-560.
43. F. Porta, L. Prati, M. Rossi and G. Scari, *Journal of Catalysis*, 2002, **211**, 464-469.
44. F. Porta, L. Prati, M. Rossi, S. Coluccia and G. Martra, *Catalysis Today*, 2000, **61**, 165-172.
45. S. Biella, L. Prati and M. Rossi, *Journal of Catalysis*, 2002, **206**, 242-247.
46. L. Prati and F. Porta, *Applied Catalysis A: General*, 2005, **291**, 199-203.
47. A. Villa, D. Wang, P. Spontoni, R. Arrigo, D. Su and L. Prati, *Catalysis Today*, 2010, **157**, 89-93.
48. A. Abad, P. Concepción, A. Corma and H. García, *Angewandte Chemie International Edition*, 2005, **44**, 4066-4069.
49. C. Y. Ma, B. J. Dou, J. J. Li, J. Cheng, Q. Hu, Z. P. Hao and S. Z. Qiao, *Applied Catalysis B: Environmental*, 2009, **92**, 202-208.
50. F.-Z. Su, Y.-M. Liu, L.-C. Wang, Y. Cao, H.-Y. He and K.-N. Fan, *Angewandte Chemie*, 2008, **120**, 340-343.
51. T. Ishida, M. Nagaoka, T. Akita and M. Haruta, *Chemistry – A European Journal*, 2008, **14**, 8456-8460.
52. H. Liu, Y. Liu, Y. Li, Z. Tang and H. Jiang, *The Journal of Physical Chemistry C*, 2010, **114**, 13362-13369.
53. S. Biella and M. Rossi, *Chemical Communications*, 2003, 378-379.
54. N. Zheng and G. D. Stucky, *Journal of the American Chemical Society*, 2006, **128**, 14278-14280.
55. B. Guan, D. Xing, G. Cai, X. Wan, N. Yu, Z. Fang, L. Yang and Z. Shi, *Journal of the American Chemical Society*, 2005, **127**, 18004-18005.

56. H. Tsunoyama, H. Sakurai, Y. Negishi and T. Tsukuda, *Journal of the American Chemical Society*, 2005, **127**, 9374-9375.
57. D. I. Enache, J. K. Edwards, P. Landon, B. Solsona-Espriu, A. F. Carley, A. A. Herzing, M. Watanabe, C. J. Kiely, D. W. Knight and G. J. Hutchings, *Science*, 2006, **311**, 362-365.
58. D. Wang, A. Villa, F. Porta, L. Prati and D. Su, *The Journal of Physical Chemistry C*, 2008, **112**, 8617-8622.
59. A. Villa, G. M. Veith and L. Prati, *Angewandte Chemie International Edition*, 2010, **49**, 4499-4502.
60. A. Abad, C. Almela, A. Corma and H. Garcia, *Chemical Communications*, 2006, 3178-3180.
61. B. Zhu and R. J. Angelici, *Chemical Communications*, 2007, 2157-2159.
62. B. Zhu, M. Lazar, B. G. Trewyn and R. J. Angelici, *Journal of Catalysis*, 2008, **260**, 1-6.
63. M.-H. So, Y. Liu, C.-M. Ho and C.-M. Che, *Chemistry – An Asian Journal*, 2009, **4**, 1551-1561.
64. A. Grirrane, A. Corma and H. Garcia, *Journal of Catalysis*, 2009, **264**, 138-144.
65. A. Grirrane, A. Corma and H. García, *Science*, 2008, **322**, 1661-1664.
66. A. Grirrane, A. Corma and H. Garcia, *Nature Protocols*, 2010, **11**, 429-438.
67. S. K. Klitgaard, K. Egeblad, U. V. Mentzel, A. G. Popov, T. Jensen, E. Taarning, I. S. Nielsen and C. H. Christensen, *Green Chemistry*, 2008, **10**, 419-423.
68. S. Kegnaes, J. Mielby, U. V. Mentzel, C. H. Christensen and A. Riisager, *Green Chemistry*, 2010, **12**, 1437-1441.
69. T. Ishida and M. Haruta, *ChemSusChem*, 2009, **2**, 538-541.
70. G. C. Bond, C. Louis, D. T. Thompson and Editors, *Catalysis by Gold*, World Scientific, 2006.
71. P. A. Sermon, G. C. Bond and P. B. Wells, *Journal of the Chemical Society, Faraday Transactions 1: Physical Chemistry in Condensed Phases*, 1979, **75**, 385-394.
72. N. W. Cant and W. K. Hall, *The Journal of Physical Chemistry*, 1971, **75**, 2914-2921.
73. S. Lin and M. A. Vannice, *Catalysis Letters*, 1991, **10**, 47-61.

74. S. D. Lin, M. Bollinger and M. A. Vannice, *Catalysis Letters*, 1993, **17**, 245-262.
75. T. Fukushima, S. Galvagno and G. Parravano, *Journal of Catalysis*, 1979, **57**, 177-182.
76. J. Y. Lee and J. Schwank, *Journal of Catalysis*, 1986, **102**, 207-215.
77. H. S. Oh, J. H. Yang, C. K. Costello, Y. M. Wang, S. R. Bare, H. H. Kung and M. C. Kung, *Journal of Catalysis*, 2002, **210**, 375-386.
78. M. Haruta, *CATTECH*, 2002, **6**, 102-115.
79. A. M. Venezia, G. Pantaleo, A. Longo, G. Di Carlo, M. P. Casaletto, F. L. Liotta and G. Deganello, *The Journal of Physical Chemistry B*, 2005, **109**, 2821-2827.
80. M. Haruta, S. Tsubota, T. Kobayashi, H. Kageyama, M. J. Genet and B. Delmon, *Journal of Catalysis*, 1993, **144**, 175-192.
81. M. Haruta, *Journal of New Materials for Electrochemical Systems*, 2004, **7**, 163-172.
82. S. Tsubota, D. A. H. Cunningham, Y. Bando and M. Haruta, in *Studies in Surface Science and Catalysis*, eds. J. M. B. D. P. A. J. G. Poncelet and P. Grange, Elsevier, 1995, vol. Volume 91, pp. 227-235.
83. F. Moreau, G. C. Bond and A. O. Taylor, *Journal of Catalysis*, 2005, **231**, 105-114.
84. R. Zanella, S. Giorgio, C. R. Henry and C. Louis, *The Journal of Physical Chemistry B*, 2002, **106**, 7634-7642.
85. R. Zanella, L. Delannoy and C. Louis, *Applied Catalysis A: General*, 2005, **291**, 62-72.
86. J. Turkevich, P. C. Stevenson and J. Hillier, *Discussions of the Faraday Society*, 1951, **11**, 55-75.
87. R. B. Grubbs, *Polymer Reviews*, 2007, **47**, 197-215.
88. P. L. Floch, *Coordination Chemistry Reviews*, 2006, **250**, 627-681.
89. C. Garcia-Martinez Joaquin, M. Wilson Orla, W. J. Scott Robert and M. Crooks Richard, in *Metal-Containing and Metallosupramolecular Polymers and Materials*, American Chemical Society, 2006, vol. 928, ch. 16, pp. 215-229.
90. R. W. J. Scott, O. M. Wilson and R. M. Crooks, *Chemistry of Materials*, 2004, **16**, 5682-5688.

91. G. Budroni and A. Corma, *Angewandte Chemie International Edition*, 2006, **45**, 3328-3331.
92. P. Serp, P. Kalck and R. Feurer, *Chemical Reviews*, 2002, **102**, 3085-3128.
93. M. Okumura, S. Tsubota and M. Haruta, *Journal of Molecular Catalysis A: Chemical*, 2003, **199**, 73-84.
94. A. Fernandez, A. Caballero, A. R. Gonzalez-Elipe, J. M. Herrmann, H. Dexpert and F. Villain, *The Journal of Physical Chemistry*, 1995, **99**, 3303-3309.
95. S. C. Chan and M. A. Barteau, *Langmuir*, 2005, **21**, 5588-5595.
96. B. C. Satishkumar, M. V. Erasmus, A. Govindaraj and C. N. R. Rao, *Journal of Physics D: Applied Physics*, 1996, **29**, 3173.
97. A. Fási, I. Pálinkó, J. W. Seo, Z. Kónya, K. Hernadi and I. Kiricsi, *Chemical Physics Letters*, 2003, **372**, 848-852.
98. W. Chen, W. Cai, L. Zhang, G. Wang and L. Zhang, *Journal of Colloid and Interface Science*, 2001, **238**, 291-295.
99. H.-L. Jiang, B. Liu, T. Akita, M. Haruta, H. Sakurai and Q. Xu, *Journal of the American Chemical Society*, 2009, **131**, 11302-11303.
100. D. Ravelli, D. Dondi, M. Fagnoni and A. Albini, *Chemical Society Reviews*, 2009, **38**, 1999-2011.
101. M. J. Kale, T. Avanesian and P. Christopher, *ACS Catalysis*, 2013, **4**, 116-128.
102. S. Linic, P. Christopher and D. B. Ingram, *Nature Materials*, 2011, **10**, 911-921.
103. A. Kudo and Y. Miseki, *Chemical Society Reviews*, 2009, **38**, 253-278.
104. A. Fujishima and K. Honda, *Nature*, 1972, **238**, 37-38.
105. X. Lang, X. Chen and J. Zhao, *Chemical Society Reviews*, 2014, **43**, 473-486.
106. S. Higashimoto, N. Kitao, N. Yoshida, T. Sakura, M. Azuma, H. Ohue and Y. Sakata, *Journal of Catalysis*, 2009, **266**, 279-285.
107. T. Shishido, T. Miyatake, K. Teramura, Y. Hitomi, H. Yamashita and T. Tanaka, *The Journal of Physical Chemistry C*, 2009, **113**, 18713-18718.
108. F. Parrino, A. Ramakrishnan and H. Kisch, *Angewandte Chemie International Edition*, 2008, **47**, 7107-7109.
109. S. Furukawa, Y. Ohno, T. Shishido, K. Teramura and T. Tanaka, *ACS Catalysis*, 2011, **1**, 1150-1153.
110. X. Lang, W. Ma, Y. Zhao, C. Chen, H. Ji and J. Zhao, *Chemistry – A European Journal*, 2012, **18**, 2624-2631.

111. J. A. Creighton and D. G. Eadon, *Journal of the Chemical Society, Faraday Transactions*, 1991, **87**, 3881-3891.
112. S. Link and M. A. El-Sayed, *The Journal of Physical Chemistry B*, 1999, **103**, 4212-4217.
113. K. L. Kelly, E. Coronado, L. L. Zhao and G. C. Schatz, *The Journal of Physical Chemistry B*, 2002, **107**, 668-677.
114. J. M. Luther, P. K. Jain, T. Ewers and A. P. Alivisatos, *Nature Materials*, 2011, **10**, 361-366.
115. M. Kanehara, H. Koike, T. Yoshinaga and T. Teranishi, *Journal of the American Chemical Society*, 2009, **131**, 17736-17737.
116. C. Rhodes, S. Franzen, J.-P. Maria, M. Losego, D. N. Leonard, B. Laughlin, G. Duscher and S. Weibel, *Journal of Applied Physics*, 2006, **100**, -.
117. M. K. Kumar, S. Krishnamoorthy, L. K. Tan, S. Y. Chiam, S. Tripathy and H. Gao, *ACS Catalysis*, 2011, **1**, 300-308.
118. C. Burda, X. Chen, R. Narayanan and M. A. El-Sayed, *Chemical Reviews*, 2005, **105**, 1025-1102.
119. S. Sarina, E. R. Waclawik and H. Zhu, *Green Chemistry*, 2013, **15**, 1814-1833.
120. D. Tsukamoto, Y. Shiraishi, Y. Sugano, S. Ichikawa, S. Tanaka and T. Hirai, *Journal of the American Chemical Society*, 2012, **134**, 6309-6315.
121. S.-i. Naya, A. Inoue and H. Tada, *Journal of the American Chemical Society*, 2010, **132**, 6292-6293.
122. A. Tanaka, K. Hashimoto and H. Kominami, *Journal of the American Chemical Society*, 2012, **134**, 14526-14533.
123. A. Tanaka, K. Hashimoto and H. Kominami, *Chemical Communications*, 2011, **47**, 10446-10448.
124. S. Sarina, H. Zhu, E. Jaatinen, Q. Xiao, H. Liu, J. Jia, C. Chen and J. Zhao, *Journal of the American Chemical Society*, 2013, **135**, 5793-5801.
125. Y. Sugano, Y. Shiraishi, D. Tsukamoto, S. Ichikawa, S. Tanaka and T. Hirai, *Angewandte Chemie International Edition*, 2013, **52**, 5295-5299.
126. S.-i. Naya, K. Kimura and H. Tada, *ACS Catalysis*, 2012, **3**, 10-13.
127. H. Zhu, X. Ke, X. Yang, S. Sarina and H. Liu, *Angewandte Chemie International Edition*, 2010, **49**, 9657-9661.

128. A. Tanaka, Y. Nishino, S. Sakaguchi, T. Yoshikawa, K. Imamura, K. Hashimoto and H. Kominami, *Chemical Communications*, 2013, **49**, 2551-2553.
129. M. Gonzalez-Bejar, K. Peters, G. L. Hallett-Tapley, M. Grenier and J. C. Scaiano, *Chemical Communications*, 2013, **49**, 1732-1734.
130. Q. Hao, B. K. Juluri, Y. B. Zheng, B. Wang, I. K. Chiang, L. Jensen, V. Crespi, P. C. Eklund and T. J. Huang, *The Journal of Physical Chemistry C*, 2010, **114**, 18059-18066.
131. T. Pakizeh, C. Langhammer, I. Zorić, P. Apell and M. Käll, *Nano Letters*, 2009, **9**, 882-886.
132. J. S. de Almeida and R. Ahuja, *Physical Review B*, 2006, **73**, 165102.
133. Y. Shiraishi, D. Tsukamoto, Y. Sugano, A. Shiro, S. Ichikawa, S. Tanaka and T. Hirai, *ACS Catalysis*, 2012, **2**, 1984-1992.
134. Y. Shiraishi, H. Sakamoto, Y. Sugano, S. Ichikawa and T. Hirai, *ACS Nano*, 2013, **7**, 9287-9297.
135. H. M. McNair, J. M. Miller and Editors, *Basic Gas Chromatography (2nd Edition)*, John Wiley & Sons, Inc., 2009.
136. Y. Leng, in *Materials Characterization*, John Wiley & Sons (Asia) Pte Ltd, 2008, pp. 79-119.
137. J. G. Dillard, in *Characterization of Composite Materials*, ed. H. Ishida, Newnes, Boston, 1994, pp. 1-25.
138. H. Kaur, Pragati Prakashan, New Delhi, 1 edn., 2009.
139. Z. Chen, T. Deutsch, H. Dinh, K. Domen, K. Emery, A. Forman, N. Gaillard, R. Garland, C. Heske, T. Jaramillo, A. Kleiman-Shwarsctein, E. Miller, K. Takanabe and J. Turner, in *Photoelectrochemical Water Splitting*, Springer New York, 2013, ch. 5, pp. 49-62.
140. R. A. Sheldon and H. van Bekkum, in *Fine Chemicals through Heterogeneous Catalysis*, Wiley-VCH Verlag GmbH, 2007, pp. 473-551.
141. B. Rieger, A. Kuenkel, G. W. Coates, R. Reichardt, E. Dinjus, T. A. Zevaco and Editors, *Synthetic biodegradable polymers. [In: Adv. Polym. Sci., 2012; 245]*, Springer GmbH, 2012.
142. R. A. Sheldon and J. K. Kochi, *Metal-Catalyzed Oxidations of Organic Compounds*, Academic Press, 1981.

143. N. Prileschajew, *Berichte der Deutschen Chemischen Gesellschaft*, 1909, **42**, 4811-4815.
144. G. Grigoropoulou, J. H. Clark and J. A. Elings, *Green Chemistry*, 2003, **5**, 1-7.
145. K. Tanaka and F. Toda, *Chemical Reviews*, 2000, **100**, 1025-1074.
146. M. Stratakis and H. Garcia, *Chemical Reviews*, 2012, **112**, 4469-4506.
147. W. W. Weare, S. M. Reed, M. G. Warner and J. E. Hutchison, *Journal of the American Chemical Society*, 2000, **122**, 12890-12891.
148. F. Wen, U. Englert, B. Gutrath and U. Simon, *European Journal of Inorganic Chemistry*, 2008, **2008**, 106-111.
149. A. M. Mueting, B. D. Alexander, P. D. Boyle, A. L. Casalnuovo, L. N. Ito, B. J. Johnson, L. H. Pignolet, M. Leeaphon, K. E. Meyer and a. et, *Inorganic Syntheses*, 1992, **29**, 279-298.
150. L. Bromberg, Y. Diao, H. Wu, S. A. Speakman and T. A. Hatton, *Chemistry of Materials*, 2012, **24**, 1664-1675.
151. B. Fultz and J. Howe, *Transmission Electron Microscopy and Diffractometry of Materials*, Springer, 2007.
152. G. Ferey, C. Mellot-Draznieks, C. Serre, F. Millange, J. Dutour, S. Surble and I. Margiolaki, *Science (Washington, DC, U. S.)*, 2005, **309**, 2040-2042.
153. G. B. Shul'pin, *Journal of Molecular Catalysis A: Chemical*, 2002, **189**, 39-66.
154. H. A. Liebhafsky and W. H. Sharkey, *Journal of the American Chemical Society*, 1940, **62**, 190-192.
155. Y. Mikami, A. Dhakshinamoorthy, M. Alvaro and H. Garcia, *Catalysis Science & Technology*, 2013, **3**, 58-69.
156. R. A. Sheldon, M. Wallau, I. W. C. E. Arends and U. Schuchardt, *Accounts of Chemical Research*, 1998, **31**, 485-493.
157. S. M. Mahajani, M. M. Sharma and T. Sridhar, *Chemical Engineering Science*, 1999, **54**, 3967-3976.
158. A. Henglein, *Langmuir*, 1999, **15**, 6738-6744.
159. P. V. Kamat, *The Journal of Physical Chemistry B*, 2002, **106**, 7729-7744.
160. R. Bera and S. Koner, *Inorganica Chimica Acta*, 2012, **384**, 233-238.
161. A. T. Bolsoni, J. S. dos Santos, M. D. Assis and H. P. Oliveira, *Journal of Non-Crystalline Solids*, 2011, **357**, 3301-3306.
162. K. Kamata, K. Yonehara, Y. Sumida, K. Hirata, S. Nojima and N. Mizuno, *Angewandte Chemie International Edition*, 2011, **50**, 12062-12066.

163. N. V. Maksimchuk, O. V. Zalomaeva, I. Y. Skobelev, K. A. Kovalenko, V. P. Fedin and O. A. Kholdeeva, *Proceedings of the Royal Society A: Mathematical, Physical and Engineering Science*, 2012.
164. I. Y. Skobelev, A. B. Sorokin, K. A. Kovalenko, V. P. Fedin and O. A. Kholdeeva, *Journal of Catalysis*, 2013, **298**, 61-69.
165. M. Haruta, *Catal. Today*, 1997, **36**, 153-166.
166. B. Hvolbæk, T. V. W. Janssens, B. S. Clausen, H. Falsig, C. H. Christensen and J. K. Nørskov, *Nano Today*, 2007, **2**, 14-18.
167. M. M. Schubert, S. Hackenberg, A. C. van Veen, M. Muhler, V. Plzak and R. J. Behm, *Journal of Catalysis*, 2001, **197**, 113-122.
168. L. Wang, B. Zhang, W. Zhang, J. Zhang, X. Gao, X. Meng, D. S. Su and F.-S. Xiao, *Chemical Communications*, 2013, **49**, 3449-3451.
169. Y. Liu, H. Tsunoyama, T. Akita, S. Xie and T. Tsukuda, *ACS Catalysis*, 2010, **1**, 2-6.
170. L.-X. Xu, C.-H. He, M.-Q. Zhu, K.-J. Wu and Y.-L. Lai, *Catalysis Letters*, 2007, **118**, 248-253.
171. P. Haider, B. Kimmerle, F. Krumeich, W. Kleist, J.-D. Grunwaldt and A. Baiker, *Catalysis Letters*, 2008, **125**, 169-176.
172. P. Haider, A. Urakawa, E. Schmidt and A. Baiker, *Journal of Molecular Catalysis A: Chemical*, 2009, **305**, 161-169.
173. Y. Liu, H. Tsunoyama, T. Akita and T. Tsukuda, *Chemistry Letters*, 2010, **39**, 159-161.
174. K.-Q. Sun, S.-W. Luo, N. Xu and B.-Q. Xu, *Catalysis Letters*, 2008, **124**, 238-242.
175. Tana, F. Wang, H. Li and W. Shen, *Catalysis Today*, 2011, **175**, 541-545.
176. Y. Liu, H. Tsunoyama, T. Akita and T. Tsukuda, *The Journal of Physical Chemistry C*, 2009, **113**, 13457-13461.
177. M. N. Martin, J. I. Basham, P. Chando and S.-K. Eah, *Langmuir*, 2010, **26**, 7410-7417.
178. D. A. Shirley, *Physical Review B*, 1972, **5**, 4709-4714.
179. H. P. Hughes and J. A. Scarfe, *Journal of Physics: Condensed Matter*, 1996, **8**, 1421.
180. http://www.casaxps.com/help_manual/line_shapes.htm.
181. P. V. Kamat, *Journal of Physical Chemistry B*, 2002, **106**, 7729-7744.

182. K. L. Kelly, E. Coronado, L. L. Zhao and G. C. Schatz, *Journal of Physical Chemistry B*, 2003, **107**, 668-677.
183. A. Henglein, *Langmuir*, 1999, **15**, 6738-6744.
184. J. Kilmartin, R. Sarip, R. Grau-Crespo, D. Di Tommaso, G. Hogarth, C. Prestipino and G. Sankar, *ACS Catalysis*, 2012, **2**, 957-963.
185. G. H. Woehrle and J. E. Hutchison, *Inorganic Chemistry*, 2005, **44**, 6149-6158.
186. D. Zhao, J. Feng, Q. Huo, N. Melosh, G. H. Frederickson, B. F. Chmelka and G. D. Stucky, *Science (Washington, D. C.)*, 1998, **279**, 548-552.
187. G. C. Bond and D. T. Thompson, *Catalysis Reviews*, 1999, **41**, 319-388.
188. V. D. Borman, M. A. Pushkin, V. N. Tronin and V. I. Troyan, *Journal of Experimental and Theoretical Physics*, 2010, **110**, 1005-1025.
189. C. Battistoni, G. Mattogno, F. Cariati, L. Naldini and A. Sgamellotti, *Inorganica Chimica Acta*, 1977, **24**, 207-210.
190. T. V. W. Janssens, B. S. Clausen, B. Hvolbaek, H. Falsig, C. H. Christensen, T. Bligaard and J. K. Norskov, *Topics in Catalysis*, 2007, **44**, 15-26.
191. L. Alves, B. Ballesteros, M. Boronat, J. R. Cabrero-Antonino, P. Concepción, A. Corma, M. A. Correa-Duarte and E. Mendoza, *Journal of the American Chemical Society*, 2011, **133**, 10251-10261.
192. G. C. Bond, *Gold Bulletin*, 1972, **5**, 11-13.
193. M. Conte, X. Liu, D. M. Murphy, K. Whiston and G. J. Hutchings, *Physical Chemistry Chemical Physics*, 2012, **14**, 16279-16285.
194. G. Lü, D. Ji, G. Qian, Y. Qi, X. Wang and J. Suo, *Applied Catalysis A: General*, 2005, **280**, 175-180.
195. A. J. Fatiadi, in *Triple-Bonded Functional Groups (1983)*, John Wiley & Sons, Ltd., 2010, pp. 1057-1303.
196. P. Pollak, G. Romeder, F. Hagedorn and H.-P. Gelbke, in *Ullmann's Encyclopedia of Industrial Chemistry*, Wiley-VCH Verlag GmbH & Co. KGaA, 2000.
197. F. F. Fleming, L. Yao, P. C. Ravikumar, L. Funk and B. C. Shook, *Journal of Medicinal Chemistry*, 2010, **53**, 7902-7917.
198. J. S. Miller and J. L. Manson, *Accounts of Chemical Research*, 2001, **34**, 563-570.
199. T. Sandmeyer, *Berichte der Deutschen Chemischen Gesellschaft*, 1885, **18**, 1492-1496.

200. S. Zhou, K. Junge, D. Addis, S. Das and M. Beller, *Organic Letters*, 2009, **11**, 2461-2464.
201. K. Yamaguchi, H. Fujiwara, Y. Ogasawara, M. Kotani and N. Mizuno, *Angewandte Chemie International Edition*, 2007, **46**, 3922-3925.
202. T. Oishi, K. Yamaguchi and N. Mizuno, *Angewandte Chemie International Edition*, 2009, **48**, 6286-6288.
203. K. Yamaguchi and N. Mizuno, *Angewandte Chemie*, 2003, **115**, 1518-1521.
204. K. Yamaguchi and N. Mizuno, *Chemistry – A European Journal*, 2003, **9**, 4353-4361.
205. M. Kotani, T. Koike, K. Yamaguchi and N. Mizuno, *Green Chemistry*, 2006, **8**, 735-741.
206. F. Li, J. Chen, Q. Zhang and Y. Wang, *Green Chemistry*, 2008, **10**, 553-562.
207. K.-N. T. Tseng, A. M. Rizzi and N. K. Szymczak, *Journal of the American Chemical Society*, 2013, **135**, 16352-16355.
208. K. Yamaguchi and N. Mizuno, *Angewandte Chemie International Edition*, 2002, **41**, 4538-4542.
209. E. C. Corker, U. V. Mentzel, J. Mielby, A. Riisager and R. Fehrmann, *Green Chemistry*, 2013, **15**, 928-933.
210. J. M. Fletcher, W. E. Gardner, B. F. Greenfield, M. J. Holdoway and M. H. Rand, *Journal of the Chemical Society A: Inorganic, Physical, Theoretical*, 1968, 653-657.
211. M. T. Uddin, Y. Nicolas, C. Olivier, T. Toupance, M. M. Müller, H.-J. Kleebe, K. Rachut, J. Ziegler, A. Klein and W. Jaegermann, *The Journal of Physical Chemistry C*, 2013, **117**, 22098-22110.
212. S. Bang, S. Lee, T. Park, Y. Ko, S. Shin, S.-Y. Yim, H. Seo and H. Jeon, *Journal of Materials Chemistry*, 2012, **22**, 14141-14148.
213. T. Kawai and T. Sakata, *Chemical Physics Letters*, 1980, **72**, 87-89.
214. G. Blondeel, A. Harriman, G. Porter, D. Urwin and J. Kiwi, *The Journal of Physical Chemistry*, 1983, **87**, 2629-2636.
215. A. A. Ismail, L. Robben and D. W. Bahnemann, *ChemPhysChem*, 2011, **12**, 982-991.
216. X. Lang, H. Ji, C. Chen, W. Ma and J. Zhao, *Angewandte Chemie International Edition*, 2011, **50**, 3934-3937.

217. N. Li, X. Lang, W. Ma, H. Ji, C. Chen and J. Zhao, *Chemical Communications*, 2013, **49**, 5034-5036.
218. Z. Zheng, C. Chen, A. Bo, F. S. Zavahir, E. R. Waclawik, J. Zhao, D. Yang and H. Zhu, *ChemCatChem*, 2014, **6**, 1210-1214.
219. D. Sun, K. Ono, T. Okajima, K. Tanizawa, M. Uchida, Y. Yamamoto, F. S. Mathews and V. L. Davidson, *Biochemistry*, 2003, **42**, 10896-10903.
220. P. L. Rinaldi, M. S. R. Naidu and W. E. Conaway, *Journal of Organic Chemistry*, 1982, **47**, 3987-3991.
221. T. Suoranta, M. Niemelä and P. Perämäki, *Talanta*, 2014, **119**, 425-429.
222. K. S. Kim and N. Winograd, *Journal of Catalysis*, 1974, **35**, 66-72.
223. L. P. Hammett, *Journal of the American Chemical Society*, 1937, **59**, 96-103.
224. M. B. Smith and J. March, *March's Advanced Organic Chemistry: Reactions, Mechanisms, and Structure, 5th Edition*, John Wiley & Sons, Ltd., 2000.
225. J. Hine, *Journal of the American Chemical Society*, 1960, **82**, 4877-4880.
226. C. Capello, U. Fischer and K. Hungerbuhler, *Green Chemistry*, 2007, **9**, 927-934.
227. C. Chen, W. Ma and J. Zhao, *Chemical Society Reviews*, 2010, **39**, 4206-4219.
228. Y. Li and F. Wasgestian, *Journal of Photochemistry and Photobiology A: Chemistry*, 1998, **112**, 255-259.
229. H. Kominami, A. Furusho, S.-y. Murakami, H. Inoue, Y. Kera and B. Ohtani, *Catalysis Letters*, 2001, **76**, 31-34.
230. Y. Zhang, N. Zhang, Z.-R. Tang and Y.-J. Xu, *Chemical Science*, 2013, **4**, 1820-1824.
231. J. Wang, X. Yang, J. Chen, J. Xian, S. Meng, Y. Zheng, Y. Shao and D. Li, *Journal of the American Ceramic Society*, 2014, **97**, 267-274.
232. C. Minero, G. Mariella, V. Maurino, D. Vione and E. Pelizzetti, *Langmuir*, 2000, **16**, 8964-8972.
233. K. Lv and Y. Xu, *The Journal of Physical Chemistry B*, 2006, **110**, 6204-6212.
234. C. Lee and D. L. Sedlak, *Journal of Molecular Catalysis A: Chemical*, 2009, **311**, 1-6.
235. H. Xie, P. E. Ray and B. L. Short, *Stroke*, 2005, **36**, 1047-1052.
236. W. Wang, L. Zhang, T. An, G. Li, H.-Y. Yip and P.-K. Wong, *Applied Catalysis B: Environmental*, 2011, **108–109**, 108-116.
237. C. S. Foote, *Org. Chem. (N. Y.)*, 1979, **40**, 139-171.

238. M. Y. Li, C. S. Cline, E. B. Koker, H. H. Carmichael, C. F. Chignell and P. Bilski, *Photochemistry and Photobiology*, 2001, **74**, 760-764.
239. D. Zhang, R. Qiu, L. Song, B. Eric, Y. Mo and X. Huang, *Journal of Hazardous materials*, 2009, **163**, 843-847.
240. Y. Nosaka, T. Daimon, A. Y. Nosaka and Y. Murakami, *Physical Chemistry Chemical Physics*, 2004, **6**, 2917-2918.
241. H. Saito and Y. Nosaka, *Chemistry Letters*, 2012, **41**, 1591-1593.
242. X. Hu, H. Ji and L. Wu, *RSC Advances*, 2012, **2**, 12378-12383.
243. M. Buchalska, P. Labuz, L. Bujak, G. Szewczyk, T. Sarna, S. Mackowski and W. Macyk, *Dalton Transactions*, 2013, **42**, 9468-9475.